

Vlp : an integral approach to the simulation of injection moulding : prediction of product properties

Citation for published version (APA):

Caspers, L. W. (1995). *Vlp : an integral approach to the simulation of injection moulding : prediction of product properties*. [Phd Thesis 1 (Research TU/e / Graduation TU/e), Mechanical Engineering]. Technische Universiteit Eindhoven. <https://doi.org/10.6100/IR443685>

DOI:

[10.6100/IR443685](https://doi.org/10.6100/IR443685)

Document status and date:

Published: 01/01/1995

Document Version:

Publisher's PDF, also known as Version of Record (includes final page, issue and volume numbers)

Please check the document version of this publication:

- A submitted manuscript is the version of the article upon submission and before peer-review. There can be important differences between the submitted version and the official published version of record. People interested in the research are advised to contact the author for the final version of the publication, or visit the DOI to the publisher's website.
- The final author version and the galley proof are versions of the publication after peer review.
- The final published version features the final layout of the paper including the volume, issue and page numbers.

[Link to publication](#)

General rights

Copyright and moral rights for the publications made accessible in the public portal are retained by the authors and/or other copyright owners and it is a condition of accessing publications that users recognise and abide by the legal requirements associated with these rights.

- Users may download and print one copy of any publication from the public portal for the purpose of private study or research.
- You may not further distribute the material or use it for any profit-making activity or commercial gain
- You may freely distribute the URL identifying the publication in the public portal.

If the publication is distributed under the terms of Article 25fa of the Dutch Copyright Act, indicated by the "Taverne" license above, please follow below link for the End User Agreement:

www.tue.nl/taverne

Take down policy

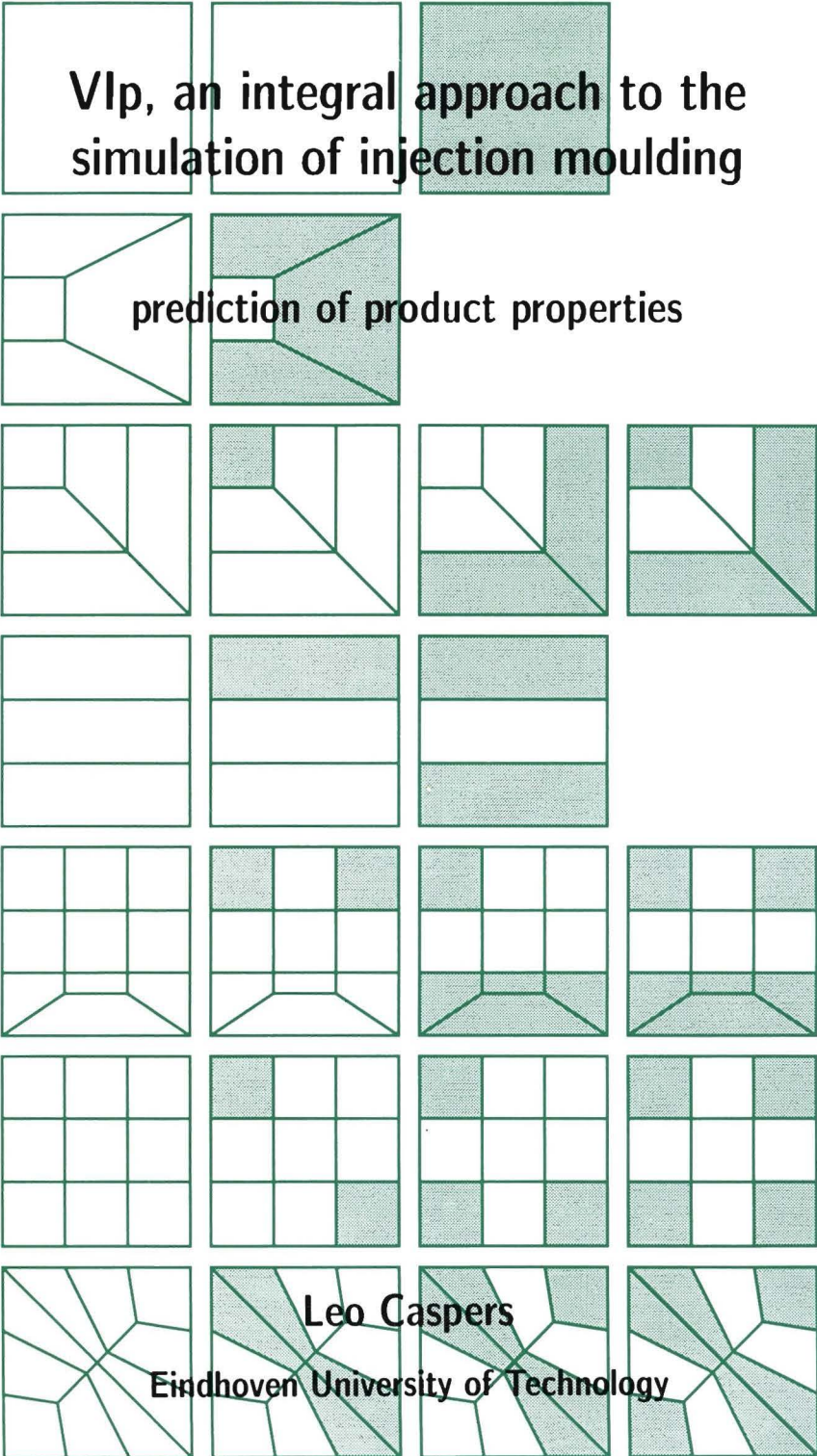
If you believe that this document breaches copyright please contact us at:

openaccess@tue.nl

providing details and we will investigate your claim.

Vlp, an integral approach to the simulation of injection moulding

prediction of product properties



This research was supported financially by the Dutch Ministry of Economic Affairs, grant number IOP-PCBP 2.5.

CIP-GEGEVENS KONINKLIJKE BIBLIOTHEEK, DEN HAAG

Caspers, Leo Wilhelmus

Vip, an integral approach to the simulation of injection moulding : prediction of product properties / Leo Wilhelmus Caspers. - Eindhoven : Technische Universiteit Eindhoven

Thesis Technische Universiteit Eindhoven. - With ref. - With summary in Dutch.

ISBN 90-386-0356-8

Subject headings: injection moulding ; numerical simulation / product properties.

Typeset by the author with the \LaTeX Documentation System

Printed by Febodruk, Enschede The Netherlands

© 1995 by Leo W. Caspers

Cover:

Left hand side column of squares represents Vip's division of quadrilaterals into subelements, while for each case all possible filling states per subelement is indicated on the right.

VIp, an integral approach to the simulation of injection moulding

prediction of product properties

Proefschrift

ter verkrijging van de graad van doctor
aan de Technische Universiteit Eindhoven
op gezag van de Rector Magnificus, prof.dr. J.H. van Lint,
voor een commissie aangewezen door het College van Dekanen
in het openbaar te verdedigen
op dinsdag 29 augustus 1995 om 16.00 uur

door

Leo Wilhelmus Caspers

geboren te Waalwijk

Dit proefschrift is goedgekeurd door de promotoren:

prof.dr.ir. H.E.H. Meijer
prof.dr.ir. F.P.T. Baaijens

en de copromotor:

dr.ir. F.N. van de Vosse

Voor Maria en mijn ouders

Contents

Summary	ix
Notation	xi
1 Introduction	1
1.1 Injection moulding	1
1.2 State of the art	5
1.3 Scope of the study	9
2 Governing equations	11
2.1 Balance equations	11
2.2 Constitutive equations	12
2.2.1 Specific volume	12
2.2.2 Cauchy stress tensor	14
2.2.3 Heat conduction and internal energy	21
2.3 Thin film approximation	21
2.4 Resulting set of equations	24
2.5 Discussion	31
3 Numerical Methods	33
3.1 Operator splitting	33
3.2 Temporal discretisation	34
3.3 Iteration methods	40
3.4 Spatial discretisation and FE formulation	40
3.5 Discussion	46
4 Material Characterisation	47
4.1 Rheology	47
4.2 Specific volume	52

4.3	Thermal capacity and heat conduction	57
4.4	Discussion	58
5	Characteristic results	59
5.1	Density distribution	59
5.2	Thermally induced residual stress	69
5.3	Flow-induced residual stress	76
5.4	Elastic recovery	79
5.5	Discussion	81
6	Concluding discussion	83
A	Accuracy of pressure element	87
A.1	Description of a test case	87
A.2	Results	88
A.3	Discussion	89
B	Remeshing technique	91
C	Simplified thermal stress computation	97
D	Thermomechanical Analyser	101
E	Governing equations for the runner system	103
	Samenvatting	115
	Acknowledgements	117
	Curriculum Vitae	119

Summary

Injection moulding is a widely spread production process for large series of geometrically complex thin-walled products. As modifications of the mould are expensive and time consuming, mould designers need to know in advance whether the moulding process will run correctly for a certain design. A production process running without problems, however, does not automatically ensure a sufficient product quality. Given the high demands that must be met nowadays, it is important to estimate the properties of the product and its dimensional accuracy and stability in advance. This requires an integral approach to the simulation of injection moulding. With the aid of a computer program that is based on this approach, mould shape and processing conditions can be optimised with respect to product quality, reducing the time spent on both mould design and iterative modification and on product testing.

In this thesis an integral analysis of the moulding process and the resulting product properties will be presented. Properties like the distribution of molecular orientation, density, material distribution in MCIM (multi-component injection moulding), degree of conversion in (R)RIM, SRIM and RTM (reinforced and structural reactive injection moulding and resin transfer moulding) and also the fibre orientation in reinforced systems are the result of the entire thermomechanical history for every material particle. Therefore, it is essential to incorporate a sufficiently accurate numerical method to approximate material derivatives. Particle tracking can be used to evaluate the accuracy of the method employed.

This study focusses on the computation of shrinkage, warpage and elastic recovery of amorphous thermoplastics. The *density* is described by a history dependent model, called the KAHR model. Although in general the computed pressure distribution during the post-filling and cooling stages highly depends on the computed density, the computation of the density distribution can be decoupled from the pressure calculation. *Residual stresses*

originate from two main effects. The *flow induced stresses* are built up during the filling and post filling stage of the process, and correspond with the orientation of the macromolecules. This orientation is (partly) frozen-in and gives rise to anisotropy of the thermal, mechanical and optical behaviour, and causes a diminished long term dimensional stability because of elastic recovery. Since the orientation hardly influences the flow, a decoupled approach can be employed for the computation of this stress. In this study a compressible Leonov model is used. The *thermally and pressure induced stresses* (or thermal stresses for short) are built up mainly during the post-filling and cooling stages, and are caused by inhomogeneous cooling and a varying pressure in time, resulting in a differential shrinkage across the thickness of the product. This stress distribution is computed using a multi-mode Maxwell model, which is a linearisation of more advanced viscoelastic models like the Leonov model mentioned. The thermal stress is generally an order of magnitude higher than the flow induced stress, and is the main cause of warpage of the product. A two-shot moulding process is modelled to illustrate this effect. It can be concluded that warpage of the product, mainly caused by asymmetrical cooling of the second shot, can be prevented in this special case by using different holding pressures for the two distinct shots of the process.

The numerical analyses are validated both experimentally and by using analytical solutions. Density and dimensional stability measurements reported in literature are all performed on simple rectangular strips, so a two dimensional model is sufficient for this part of the validation. For the two-shot moulding experiments, however, a more complex geometry is chosen, requiring a $2\frac{1}{2}$ D approach for the analyses. This approach is employed for the development of the simulation code VIp (which stands for *Polymer Processing & Product Properties Prediction Program*) at CPC (Centre for Polymers and Composites). Based on a parent program, that, finally, resulted in injection moulding simulation software like "POMO" and "Inject-3", VIp has become a validated, flexible and accurate simulation code of practical use for high-end applications.

Notation

Operators and functions

$\vec{\nabla}$	$1/m$	gradient operator
$\vec{\nabla}^*$	$1/m$	gradient operator with respect to the midplane
$\vec{\nabla}_0$	$1/m$	gradient operator with respect to reference state
\dot{a}	$1/s$	material derivative
\mathbf{A}^c	-	conjugation
\mathbf{A}^d	-	deviatoric part
\mathbf{A}^{-d}	-	deviatoric part of inverse
\mathbf{A}^{-1}	-	inverse
$I_3^{\mathbf{A}}$	-	third invariant
$\vec{a} \cdot \vec{b}$	-	dot product
$tr(\mathbf{A})$	-	trace
$\exp(a)$	-	e^a
\mathcal{L}	-	convection diffusion operator

Subscripts

a	element nodal point number
c	convected quantity
i	time step number

j	mode number
n	dimension number
C	Cross model parameter
L	Leonov model parameter
M	Maxwell model parameter
K	Voigt model parameter
δ	KAHR model parameter
∞	equilibrium behaviour

List of symbols

\hat{a}	Pa	used in incremental formulation of thermal stress component in stiffness matrix
a^\bullet	Pa	used in incremental formulation of thermal stress component in stiffness matrix
a_p	-	pressure dependent shift factor of relaxation times of δ (KAHR model)
a_T	-	temperature dependent shift factor of relaxation times
a_0	m^3/kg	first temperature fit parameter (Tait model)
a_{0m}	m^3/kg	first temperature fit parameter melt state (Tait model)
a_{0s}	m^3/kg	first temperature fit parameter solid state (Tait model)
a_1	$m^3/(kg K)$	second temperature fit parameter (Tait model)
a_{1m}	$m^3/(kg K)$	second temperature fit parameter melt state (Tait model)
a_{1s}	$m^3/(kg K)$	second temperature fit parameter solid state (Tait model)
b	$1/Pa$	fit parameter in expression for a_p (KAHR model)
\hat{b}	Pa	used in incremental formulation of thermal stress component in stiffness matrix
b^\bullet	Pa	used in incremental formulation of thermal stress component in stiffness matrix
c_p	$J/(kg K)$	heat capacity at constant pressure

c_1	-	first constant in WLF shift factor
c_2	K	second constant in WLF shift factor
c_3	$1/K$	first constant in Arrhenius shift factor
e	J/kg	specific internal energy
h	m	local thickness
i	-	time step number (subscript)
j	-	mode number
k	-	Poisson ratio
l	m	length
m	-	number of modes
p	Pa	pressure in polymer melt
p_{atm}	Pa	atmospheric pressure
p_e	Pa	pressure prescribed at gate
p^h	Pa	opposite of hydrostatic stress
q	m^2/s	volume flux per unit of length (line gates)
r	m	local coordinate in radial direction in runner
r'	m	variable of integration for integrals across radius
r_h	$J/(kg s)$	specific heat source
s	m	local coordinate along centre line of runner
s_0	K/Pa	fitted constant value of $\frac{\partial T_g}{\partial p}$ (Tait model)
t	s	time
t'	s	variable of integration in time integrals
t''	s	variable of integration in time integrals
Δt	s	time step
u	-	unknown in example convection diffusion equation
v^r	m/s	velocity in radial direction in runner
v^s	m/s	velocity parallel to centre line of runner
v_3^e	m/s	velocity in local thickness direction
x	-	fit parameter in expression for a_δ (KAHR model)
x_3^e	m	local coordinate in thickness direction

w_j	-	weight factor for mode j
z_a	m	thickness coordinate in fibre direction (shell element)
z_{T_g}	m	thickness coordinate at glass transition
B_m	Pa	pressure parameter for melt state (Tait model)
B_s	Pa	pressure parameter for solid state (Tait model)
B_0	Pa	first fit pressure parameter (Tait model)
B_{0m}	Pa	first fit parameter in expression for B_m
B_{0s}	Pa	first fit parameter in expression for B_s
B_1	$1/K$	second pressure parameter (Tait model)
B_{1m}	$1/K$	second fit parameter in expression for B_m
B_{1s}	$1/K$	second fit parameter in expression for B_s
C	m/N	compliance of mould
C_a	-	material independent constant (Tait model)
C_0	m^2/N	linear stress optical coefficient
D	-	diffusion coefficient in general convection diffusion equation
F	-	right hand side in general convection diffusion equation
F_n	$m^{n+1}/Pa s$	terms in expression for fluidity S
F_r	-	term in expression for \dot{B}_{kl}
G	N/m^2	constant shear modulus
G'	N/m^2	storage shear modulus
G''	N/m^2	loss shear modulus
G^\bullet	N/m^2	deviatoric strain coefficient in deviatoric stress expression
H_a	$J/(smK)$	heat transfer coefficient from product surface to ambient air

H_m^+	$J/(smK)$	heat transfer coefficient from "top" surface of product to mould
H_m^-	$J/(smK)$	heat transfer coefficient from "bottom" surface of product to mould
H_R	$J/(smK)$	heat transfer coefficient from product to mould for runner
J'	m^2/N	storage compliance (Voigt model)
J''	m^2/N	loss compliance (Voigt model)
J_g	m^2/N	instantaneous compliance (Voigt model)
J_j	m^2/N	creep compliance for mode j (Voigt model)
K	N/m^2	constant bulk modulus
K^\bullet	Pa	volumetric strain coefficient in hydrostatic pressure expression
N_a	-	interpolation function for nodal point a , shell elements
Q	m^3/s	total volume flux (runners)
R	m	runner diameter
S	$m^3/(Pa s)$	fluidity, defined for cavity
S_c	$m^4/(Pa s)$	fluidity, defined for runner
T	K	temperature
T_R	K	mould wall temperature for runner
T_r	K	reference temperature
T_a	K	ambient air temperature
T_e	K	injection temperature
T_g	K	glass transition temperature
T_{g0}	K	fit parameter representing the glass transition temperature at zero pressure (Tait model)
T_m^+	K	mould temperature at "top" surface of product
T_m^-	K	mould temperature at "bottom" surface of product

T_w^+	K	mould wall temperature at “top” surface of product
T_w^-	K	mould wall temperature at “bottom” surface of product
α	$1/K$	thermal expansion coefficient
α_m	$1/K$	thermal expansion coefficient polymer melt
α_s	$1/K$	thermal expansion coefficient solid polymer
α^+	m	position of first solidification front in thickness direction
α^-	m	see α^+ , but now for the second solidification front
α^s	m	see α^+ , but now for the solidification front in the runner
$\Delta\alpha$	$1/K$	difference in thermal expansion coefficient between melt and solid state
β	-	parameter defining the width of the spectrum of volume relaxation times (KAHR model)
β^*	Pa/K	temperature coefficient in hydrostatic pressure expression
$\dot{\gamma}$	$1/s$	shear rate
γ^*	Pa	coefficient for δ in hydrostatic pressure expression
$\dot{\gamma}_r$	$1/s$	shear rate in runner
$\dot{\gamma}_1$	$1/s$	first component of shear rate with respect to base O_ϵ
$\dot{\gamma}_2$	$1/s$	second component of shear rate with respect to base O_ϵ
δ	-	normalised deviation of ν from equilibrium
ϵ^h	-	volumetric linear strain
ζ_{Kj}	s	reduced creep compliance for deviatoric strain, mode j (Voigt model)
ζ_{Mj}	s	reduced relaxation modulus for deviatoric stress, mode j (Maxwell model)

ζ'_{Mj_i}	s	reduction factor for $\sigma_{j_i}^d$ at $t = t_i$
ζ_δ	-	response function of the bulk relaxation spectrum below T_g (KAHR model)
ζ_n	-	isoparametric coordinates
η	$Pa\ s$	dynamic shear viscosity
η_r	$Pa\ s$	viscosity of viscous part (Leonov model)
η_{r0}	$Pa\ s$	reference viscosity for viscous part (Leonov model)
η_C	$Pa\ s$	shear rate independent viscosity (7-constant Cross model)
η_0	$Pa\ s$	reference viscosity
η_K	$Pa\ s$	shear viscosity (Voigt model)
θ	$1/K$	fit parameter in expression for a_{T_g} (KAHR model)
κ	$1/Pa$	isothermal compressibility coefficient
κ'	$1/Pa$	pseudo-compressibility
κ_1	$1/Pa^2$	coefficient in equation for $\Delta\kappa$
$\Delta\kappa$	$1/Pa$	difference in isothermal compressibility coefficient between melt and solid state
$\Delta\kappa_0$	$1/Pa$	pressure independent part of $\Delta\kappa$
λ	$J/(Kms)$	heat conduction coefficient in thickness direction
ν	m^3/kg	specific volume
ρ	kg/m^3	density
ρ_s	kg/m^3	density at product surface
ρ^*	kg/m^3	reduced density
τ_0	s	reference relaxation time
ϕ_1	-	first rotation of fibre base
ϕ_2	-	second rotation of fibre base
χ	m	variable of integration for integrals along the thickness

Γ_f	-	boundary at the flow front
Γ_e	-	boundary at the gate
Γ_R	-	boundary of the runner in radial direction
Γ_0	-	boundary where polymer is in contact with the mould at the edges of the midplane or "dead end" of runner
Γ_+	-	"top" surface of the product
Γ_-	-	"bottom" surface of the product
\bar{c}^*	<i>Pa</i>	integration constant
\vec{g}_n	-	covariant base vectors
\vec{h}	<i>J/(m² s)</i>	heat flux vector
\vec{f}	<i>N/kg</i>	specific body forces
\vec{n}^*	-	unit outward normal
\vec{u}	<i>m</i>	displacement vector
$\Delta\vec{u}$	<i>m</i>	incremental displacement vector
$\Delta\vec{u}^f$	<i>m</i>	incremental displacement of third fibre base vector
$\Delta\vec{u}^l$	<i>m</i>	incremental displacement in reference surface
\vec{v}	<i>m/s</i>	velocity vector
\vec{v}^*	<i>m/s</i>	velocity parallel to midplane of thin-walled geometry
$\vec{v}^{\bar{*}}$	<i>m/s</i>	velocity parallel to midplane of thin-walled geometry averaged across the thickness
\vec{x}	<i>m</i>	position vector
\vec{x}^f	<i>m</i>	third fibre base unit vector (shell element)
\vec{x}^l	<i>m</i>	position vector nodal point <i>a</i> (shell element)
B	-	Finger tensor
B_e	-	Finger tensor corresponding to F_e
$\bar{\mathbf{B}}_e$	-	Finger tensor corresponding to $\bar{\mathbf{F}}_e$

\mathbf{B}_p	-	Finger tensor corresponding to \mathbf{F}_p
\mathbf{D}	$1/s$	rate of deformation tensor
\mathbf{D}_e	$1/s$	rate of deformation tensor corresponding to \mathbf{L}_e
\mathbf{D}_p	$1/s$	rate of deformation tensor corresponding to \mathbf{L}_p
\mathbf{F}	-	deformation tensor
\mathbf{F}_e	-	elastic part of deformation tensor
$\bar{\mathbf{F}}_e$	-	elastic part of deformation tensor with volumetric effects excluded
\mathbf{F}_p	-	plastic part of deformation tensor
\mathbf{I}	-	second order unity tensor
\mathbf{L}	$1/s$	velocity gradient tensor
\mathbf{L}_e	$1/s$	elastic part of velocity gradient tensor
\mathbf{L}_p	$1/s$	plastic part of velocity gradient tensor
\mathbf{R}^{fg}	-	transformation tensor from fibre base to global base
\mathbf{R}^{fl}	-	transformation tensor from fibre base to lamina base
\mathbf{R}^{gl}	-	transformation tensor from global base to lamina base
\mathbf{W}_e	$1/s$	spin tensor corresponding to \mathbf{L}_e
\mathbf{W}_p	$1/s$	spin tensor corresponding to \mathbf{L}_p
ε	-	Linear strain tensor
ε_c	-	Linear strain tensor caused by creep
λ	$J/(Kms)$	Heat conduction tensor
σ	N/m^2	Cauchy stress tensor
σ_e	N/m^2	elastic part of Cauchy stress tensor (Leonov model)
σ_v	N/m^2	viscous part of Cauchy stress tensor (Leonov model)
σ^\bullet	N/m^2	Cauchy stress tensor without incorporation of the incremental strain of the current time step

\underline{g}	Pa	initial stress
$\Delta \underline{\varepsilon}$	-	incremental linear strain components
$\Delta \hat{\underline{\varepsilon}}$	-	incremental linear strain components with respect to covariant base
$\underline{\sigma}$	Pa	Cauchy stress components
\underline{B}	$1/m$	strain displacement matrix
\underline{D}	$1/s$	rate of deformation matrix
\underline{L}	$1/s$	velocity gradient matrix
\underline{M}	Pa	stiffness matrix
\underline{R}^{cl}	-	transformation matrix from covariant base to lamina base
$\underline{R}^{\phi f}$	-	transformation matrix from incremental fibre rotations to incremental fibre displacements

Chapter 1

Introduction

The injection moulding process will be shortly described to illustrate the complex thermomechanical history that material particles experience during moulding. The scientific and industrial relevance of the numerical simulation of injection moulding as well as the concept of high precision in relation to injection moulded parts are indicated. The state of the art is described with respect to the numerical simulation of the process. Finally, the objectives and methodologies employed in this study are presented.

1.1 Injection moulding

The process

Injection moulding is one of the most commonly used processes for the production of large series of polymer products. The main reason is that this moulding process hardly dictates any geometrical limitations for product design, giving rise to a substantial integration: parts that have to be assembled when more conventional production techniques are applied, can be unified into one single product using injection moulding.

The main parts of an injection moulding machine are shown schematically in figure 1.1. Here the process will be described for injection moulding of thermoplastic amorphous materials. For semi-crystalline materials and thermosets the process is similar. Powder (or granules) of the moulding material is fed via a hopper (1) into an extruder (2), that consists of a screw, rotating inside a heated (4) barrel, where the material melts and is transported towards the mould (3). During the transport, mixing takes place to homogenise the materials temperature. The melt is stored in front of the

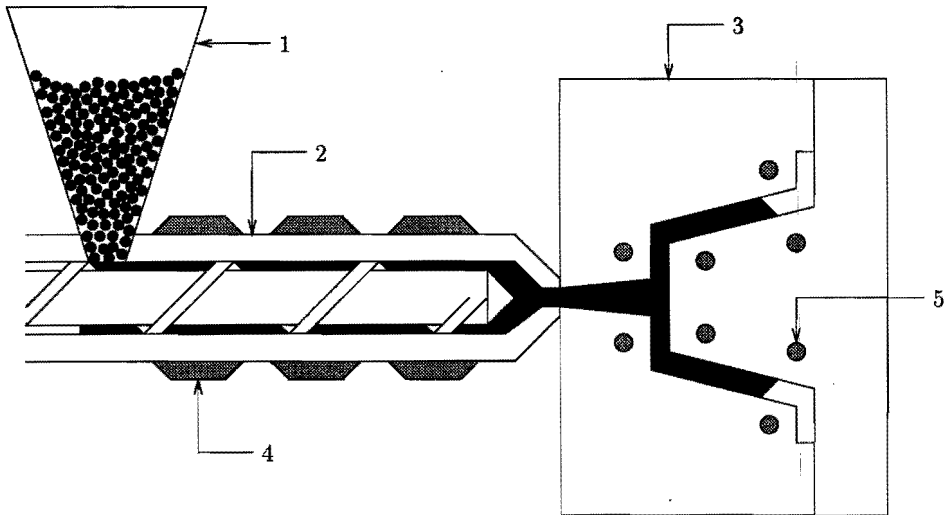


Figure 1.1: Schematic layout of an injection moulding machine

screw, that is meanwhile moving backwards against the so-called back pressure, exerted via a hydraulic cylinder at the end of the screw. When enough material is molten, the screw is moved forward by the same hydraulic cylinder. Since generally backwards flow into the screw channel is prevented by a non-return valve (not indicated), the melt is pushed forward and fills the mould at a typical high speed of 0.5 m/s. As the mould is cooled (5), the material solidifies, and its density increases. In order to prevent shrinkage of the product, the material is put under a high pressure (packing and holding stage), until the gate solidifies and no more material can be injected. This point defines the start of the cooling stage. When the product has acquired enough stiffness, the mould is opened and the product is ejected. In the meantime the extruder has plasticised a new batch of material and the cycle can be repeated.

High precision

Typical injection moulded products are parts such as car bumpers and dashboards, housings and elements of electric and electronic devices and all kinds of objects for domestic application. During the last decade, injection moulding is more and more applied to products that require high dimensional and

optical accuracy, for example compact disc player lenses and glass fibre connectors. Precision of an injection moulded product can be defined as the dimensional accuracy and stability in time. It depends on the distribution of a number of typical properties throughout the product, most of which are a result of the complex thermomechanical history of the material. All recent studies are limited to amorphous thermoplastics since effects like the degree of crystallinity, or shrinkage as a result of chemical reaction, still need a lot of research before they can be modelled accurately. For amorphous thermoplastics the following effects are of major influence on precision:

Volume relaxation An amorphous polymer is defined to be in the fluid state, when its typical volume relaxation times are much shorter than the process time. As generally relaxation times increase with decreasing temperature, a temperature region can be defined where relaxation and process times are comparative, followed by a region where this volume relaxation is much slower than the process. The intermediate region is called the glass transition region. In the lower temperature region the polymer is called to be in the glassy state. There is a noticeable decrease of the thermal expansion coefficient $\frac{1}{\nu} \frac{\partial \nu}{\partial T}$ during the transition, although it does not become zero, since only a part of the volume relaxation behaviour is affected (see figure 1.2, curve 1). This part adapts only very slowly to changing conditions, but it still will tend to reach the equilibrium situation (curve 2). This shrinkage effect is called physical ageing (curve 5). Cooling of the polymer at higher rates (a decrease in process time) shifts the transition region to higher temperatures (curve 3). Relaxation times increase with increasing pressure. This implies that the temperature region where glass transition takes place is a function of the local pressure (see curve 4). Finally, the relaxation times are a function of the deviation of the density from its equilibrium value, which makes the behaviour non-linear.

Orientation Due to deformation of the polymer melt during injection and packing, the macromolecules, that initially are in a random coil conformation, tend to stretch and orient. When the flow stops, they try to regain their original conformation. This relaxation is hindered due to the rapid cooling and part of the orientation is frozen-in. As deformation and temperature are functions of space and time, this gives rise to a complex distribution of the so-called flow-induced stress. The tendency of the macromolecules to regain their random coil conformation does not disappear when T_g is passed; only

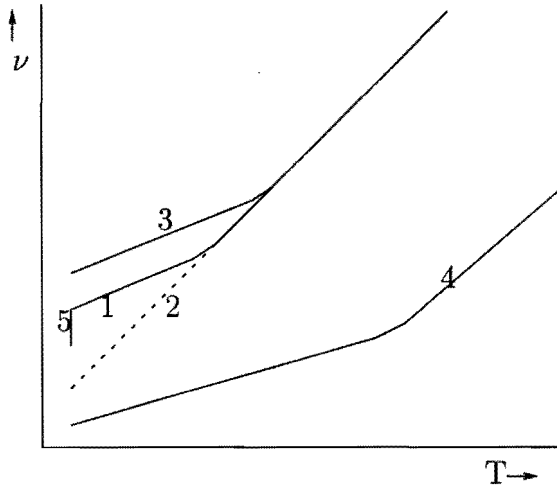


Figure 1.2: Specific volume (ν) for an amorphous polymer as a function of temperature (T); 1: cooling at zero pressure; 2: equilibrium behaviour at zero pressure; 3: cooling at high speed, zero pressure; 4: cooling at high pressure; 5: physical ageing

the rate at which this process continues is lowered several decades. This leads to undesired anisotropic deformation of the product during its lifetime. This elastic recovery, which can be looked upon as creep caused by the frozen-in stress (see Struik, 1990, part 2), should be minimised for a dimensionally stable product.

Temperature- or pressure-induced residual stress When a cross section of a thin walled product is considered, every material particle experienced its own temperature and pressure history. Some particles solidified under higher pressure or at higher cooling rates than others. Consequently the strain during solidification varied across the thickness. Combined with the fact that not all material solidified at the same time, this results into a stress distribution across the thickness. This not only causes shrinkage after demoulding but, in case of unbalanced mould wall temperatures, also leads to warpage of the product. As this temperature or pressure induced residual stress is usually much higher than the flow-induced stress, the latter are of minor influence on warpage after demoulding, but may dominate, as mentioned earlier, the dimensional stability.

Adsorption of fluids Some polymers, like for instance nylon, may adsorb liquids (like water) up to even ten volume percent, causing an expansion of the product. As this effect mainly depends on the type of polymer and liquid, and cannot be altered significantly by the processing conditions, no attempt is made to model this phenomenon here. It is clear that these materials should be disregarded when high precision is required.

Relevance of simulations

In practice much time is spent on the design of the mould, because of its major influence on product quality and because it is usually impossible to compensate for deficiencies made in the mould design by adjusting processing parameters during production. Expensive modifications of the moulds are often necessary. Mould designers make use of injection moulding simulation programs in order to prevent these imperfections. Most programs are capable of predicting weld line locations and location of air traps, giving the opportunity to optimise the locations of gates and air vents. Also the filling pressure and the pressure and temperature distributions inside the mould during packing and cooling, are estimated in order to evaluate the necessary clamping force, machine size and the cycle time. Usually this is where for most mould designers the simulation ends. The influence of the polymer selected and process conditions chosen on the product properties is not predicted by the simulation. Only empirical rules, of which the validity is severely limited due to the pronounced presence of non-linear effects, prevail. They may be sufficient for products with relatively low demands on accuracy. However, when high precision is required and product properties like shrinkage, warpage and dimensional stability become important, the prediction of these quantities as a function of processing conditions and material chosen must form part of the simulations: an integral approach to the simulation of injection moulding.

1.2 State of the art

Process simulation

Since the introduction of the $2\frac{1}{2}$ D approach of Hieber and Shen (1980) to simulate the filling stage of injection moulding for viscous fluids, this model was refined by e.g. Boshouwers and van der Werf (1988) and Sitters (1988) and extended towards the postfilling stage by Chiang *et al.* (1991b). The

thermomechanical behaviour of the mould was first taken into account by Chiang *et al.* (1991a). Since then, the process simulations were extended to similar processes like multi-component injection moulding (see e.g. Turng *et al.* (1993) and Zoetelief (1995)), resin transfer moulding (see e.g. Liang *et al.*, 1993), orientation of fibres in filled materials (see e.g. Cintra Jr. and Tucker III, 1994), gas assisted injection moulding (see e.g. Turng and Wang, 1991), processing of semi-crystalline materials (see e.g. Saiu *et al.*, 1992), and reactive injection moulding (see e.g. Hayes, 1991). Papathanasiou and Kamal (1993) introduced a viscoelastic model to compute the pressure inside the cavity during filling and Nguyen and Kamal (1993) gave an extension to include the packing stage. Their analyses, however, are still limited to the $2\frac{1}{2}$ D approximation, neglecting the local phenomena such as junctions and corners, as studied by e.g. Akkerman (1993). All these results eventually could be combined employing a hybrid $2\frac{1}{2}$ D - 3D technique. The ever increasing computing power of today's computers might even allow a full 3D approach in the near future.

Physical ageing

In order to describe physical ageing of polymers in terms of volume relaxation, the pvT model used must include an equilibrium value of the specific volume as a function of pressure and temperature, as well as a description or the kinetics of the specific volume tending from its momentary value towards its equilibrium value. For both aspects: equilibrium values and kinetics, structural as well as phenomenological models have been proposed.

A well-known structural model for the equilibrium behaviour of polymers is developed by Simha and Somcynsky (1969) (SS theory), representing a large family of lattice models (see e.g. Nies and Stroeks (1990)). Macromolecules are modelled on a lattice, each segment occupying a site. This introduces a structure parameter, being the fraction of unoccupied sites or free volume. Several assumptions are made on the interaction between the segments. The assumptions eventually lead to the formulation of a partition function in terms of molecular and thermodynamical quantities, that approximates the total number of states that the system can be in. From this, an expression for the Helmholtz free energy can be derived, which is minimised with respect to the structure parameter, as the fluid state is at equilibrium.

A successful structural model for the kinetics of physical ageing that is associated with the SS theory was developed by Robertson *et al.* (1985).

From the average free volume and its fluctuation, a discrete distribution of the free volume is derived for the equilibrium state, defining a discrete number of states for the local free volume. By introducing a pressure, temperature and/or structure dependent expression for the transition rate from one state to another, a time dependent $p\nu T$ behaviour can be described. A similar theory was developed by Vleeshouwers (1993), based on the model of Nies and Stroeks (1990).

Two phenomenological models that are often used for description of the $p\nu T$ behaviour of polymeric fluids are represented by the Tait equation, in which a linear temperature dependence and an exponential pressure dependence of the density is given (see Zoller (1982) and equation (2.6)) and the model of Spencer and Gilmore (1951), which resembles the behaviour of an ideal gas.

A class of phenomenological models for the ageing of polymer glasses was proposed by Kovacs *et al.* (1979). The normalised deviation of the specific volume from equilibrium is written as a time integral of the temperature history, and later (see Ramos *et al.*, 1988) also of the pressure history. The volume relaxation is described by means of a relaxation spectrum, which is chosen pressure, temperature and structure dependent (see also equations (2.10) and (2.11)).

The main advantage of the use of structural models is that the parameters can be given a physical meaning and may be used for the description of other properties of the material such as the modulus, and allow for an extrapolation beyond the limit of experimentally accessible value. Besides, they may give an insight into the mechanisms governing specific volume (relaxation). The expressions found are, especially for the relaxation times, often similar to those of phenomenological models and, moreover, they are fitted on the same experimental data. Therefore, the phenomenological models could beneficially be used, especially because they often lead to a better fit and require less computing time. Care must be taken in their use, however, since extrapolation might be inconsistent with physical laws.

Residual stresses

Lee *et al.* (1965) developed a viscoelastic model for the calculation of (thermally induced) residual stresses in tempered flat glass. It was validated experimentally by Narayanaswamy and Gardon (1969) and, in a subsequent paper, extended to include structural relaxation (see Gardon and Narayanaswamy, 1970). A significant extension since then is the introduc-

tion of the often dominating influence of the pressure during solidification on the stress distribution (see Titomanlio *et al.* (1987), Brucato *et al.* (1989)). They employed a viscous-elastic material model. Baaijens (1991) employed the model of Lee *et al.* (1965) with inclusion of the pressure effects, presenting a 2 dimensional analysis. Douven (1991) and also Santhanam (1992) included this approach into their $2\frac{1}{2}$ models enabling the analysis of more complex geometries. The computed stresses are systematically overpredicted (see also Zoetelief *et al.* (1995)).

Isayev and Hieber (1980) used the Leonov model for computing flow induced residual stresses, caused by the deformation during filling only, employing a $1\frac{1}{2}$ D approach. Baaijens and Douven (1990) formulated a compressible version of the Leonov model, enabling the prediction of the stresses, induced during the post-filling stage. This proved to be an essential extension of the model. Flaman (1990) applied this model for the prediction of residual birefringence and compared the computed results with measurements. Douven (1991) extended the model for the application to $2\frac{1}{2}$ D geometries. Wimberger-Friedl (1991) made it plausible that cooling stresses during vitrification may induce a biaxial orientation, which in some cases dominates the orientation caused by (uniaxial shear) flow. Recent studies show that the high level of orientation in the surface of the product may be induced by these cooling stresses, instead of the extensional flow in the flow front. The application of insulating and active heating layers in the mould wall was investigated theoretically and experimentally by Jansen (1993).

Elastic recovery

The only reference we could find on the quantitative prediction of elastic recovery in injection moulded parts is represented by the work of Struik (1990). A number of model experiments are described, that isolate the effect of orientation on the dimensional stability of the samples below the glass transition temperature. A simple model, that compared well with the experiments, is presented.

Shrinkage and warpage

The computation of shrinkage and warpage is usually based on the computed thermally and pressure induced stress distribution (see Douven (1991), Santhanam (1992) and Chiang *et al.* (1993)). Structural modelling is used for the computation of the warped geometry. Aspects like the flow-

induced stress contribution, physical ageing and elastic recovery are omitted in the analyses. Only Walsh (1993), who computes the strain contributed by shrinkage, degree of crystallisation, mold restrictions and orientation (in stead of stresses), actually included all factors by employing linear regression analysis on the results of a number of moulding experiments. The strains thus computed form the input for a structural analysis.

1.3 Scope of the study

The main objective of this study is the development and implementation of a validated computational method for the simulation of the injection moulding process, including the possibility to predict the long term mechanical behaviour of the moulded product as a function of polymer properties and processing conditions. The method developed must be suitable for the geometric complexity that is characteristic for injection moulded parts, but can be restricted to thin walled geometries. Validation of the method by comparison with analytical solutions and experimental data is of great importance.

To achieve these objectives, first a mathematical model is derived that describes the injection moulding process as well as the relevant mechanical properties of the product based on both balance and constitutive equations (Chapter 2). The resulting partial differential equations cannot be solved analytically, as they are non-linear, coupled and defined on a geometrically complex domain. A finite element model to obtain approximate solutions of these differential equations is derived in Chapter 3. Stability and convergence of the numerical methods applied are verified by comparing the numerical results to analytical solutions. Most parameters for the rheological and thermal behaviour of the moulding material are available from polymer manufacturers and from the open literature. The parameters for the time dependence of the density were determined by measurements with a thermo-mechanical analyser (TMA). In Chapter 4 these experiments are described and all material parameters, necessary in advanced computer models like VIp, are summarised. The materials that are characterised are commercially available grades of PS and PMMA. To illustrate the predicting capabilities of the code developed, in Chapter 5 several cases are studied, each focussing on one aspect of high precision and comparing numerical with experimental results. The final chapter summarises the conclusions and gives some recommendations for future research.

Chapter 2

Governing equations

In this chapter, the equations are derived that form the basis of the model of the injection moulding process and the properties of the resulting product. First the balance equations and constitutive equations are summarised. The thin film approximation is introduced in order to simplify the equations. Subsequently a full set of equations is derived for the pressure, shear rate, velocity and temperature. The equations that describe product properties like residual stresses and density distributions are given next and, finally, the equations for shrinkage (including physical ageing) and warpage (including elastic recovery), resulting from stresses and density distributions, are given.

2.1 Balance equations

Conservation of mass, momentum, moment of momentum and energy can be expressed by the following equations (local formulation, see e.g. Bird *et al.* (1960)):

$$\dot{\rho} + \rho \vec{\nabla} \cdot \vec{v} = 0 \quad (2.1)$$

$$\vec{\nabla} \cdot \boldsymbol{\sigma}^c + \rho \vec{f} = \rho \dot{\vec{v}} \quad (2.2)$$

$$\boldsymbol{\sigma} = \boldsymbol{\sigma}^c \quad (2.3)$$

$$\rho \dot{e} = \boldsymbol{\sigma} : \mathbf{D} - \vec{\nabla} \cdot \vec{h} + \rho r_h \quad (2.4)$$

where ρ denotes the density, \vec{v} the velocity vector, \mathbf{D} is the rate of deformation tensor, $\boldsymbol{\sigma}$ is the Cauchy stress tensor, \vec{f} is the specific (i.e. per unit mass) body force, e is the specific internal energy, \vec{h} is the heat flux vector and r_h is the specific heat source.

2.2 Constitutive equations

Constitutive equations are required for σ , e and \vec{h} to solve the balance equations. The thermodynamic pressure (representing the resistance against static volume changes) will be chosen as independent variable (see Sitters, 1988, chap. 2), so one more constitutive equation is needed: the one for the specific volume ν (the reciprocal value of the density ρ). It is assumed that the specific body forces \vec{f} and the specific heat source r_h can be neglected. In the next subsections, the constitutive equations are given for each of the quantities ν (2.2.1), σ (2.2.2), e and \vec{h} (2.2.3).

2.2.1 Specific volume

The specific volume of amorphous thermoplastics shows non-linear history dependent behaviour (see Vleeshouwers, 1993). In the fluid state the specific volume basically equals its thermodynamic equilibrium value, that depends on temperature and pressure only. If the temperature or pressure is changed, the specific volume approaches its new equilibrium value at a principally finite rate. This rate depends on temperature, pressure and on the deviation from equilibrium. The latter indicates the existence of a relaxation time and the fluid state is defined here as the state for which this relaxation time is much shorter than the representative process time. In other words, in the fluid state equilibrium is attained instantly on the time scale of the process.

Upon cooling, the relaxation time increases. Within the glass transition range, the relaxation time becomes comparative to the process time and the specific volume lags somewhat behind to changing conditions. As the relaxation time depends on pressure and temperature, the value of pressure and temperature at which the glass transition takes place depends on the process time. For higher cooling rates, for instance, the glass transition temperature increases (compare figure 1.2).

In the glassy state, the relaxation time is high compared to the process time but still has a finite value. This causes the so-called physical ageing of polymer glasses, a slow change of the specific volume towards its equilibrium value. Experiments show that, after more complex temperature or pressure histories, the deviation from equilibrium first may increase, followed by a gradual decrease (see Chapter 4). In order to describe this behaviour properly, a spectrum of relaxation times rather than one representative time proves to be necessary (see Hutchinson and Kovacs, 1976). Besides, it has been shown that the relaxation times depend on the deviation from equilib-

rium itself, thus introducing the non-linear behaviour mentioned (see Kovacs *et al.*, 1979).

The specific volume depends on pressure p , temperature T , and its (history dependent) normalised deviation from equilibrium δ :

$$\nu = \nu(p, T, \delta) \quad (2.5)$$

Many models assume that δ , and thus ν , depends on pressure and temperature only. One example is the so-called Tait model (see Zoller, 1982):

$$\nu = (a_0 + a_1(T - T_{g0}))(1 - C_a \ln(1 + \frac{p}{B})) \quad (2.6)$$

$$B = B_0 \exp(-B_1 T) \quad (2.7)$$

$$T_g = T_{g0} + s_0 p \quad (2.8)$$

Here C_a is a material independent constant of the value 0.0894. The parameters a_0 , a_1 , B_0 and B_1 are constants, that are different for the melt ($T > T_g$, indexed m) and the solid state ($T < T_g$, indexed s). The total set of parameters a_{0m} , a_{1m} , B_{0m} , B_{1m} , a_{0s} , a_{1s} , B_{0s} , B_{1s} , T_{g0} and s_0 are fitted on measurements of ν , varying the pressure and the temperature. The a parameters represent the temperature dependence of ν at zero absolute pressure. The B parameters include the pressure dependence. T_{g0} represents the glass transition temperature at zero pressure, which is assumed to be constant in this model. Equation (2.6) to (2.7) do not include the history dependent effects mentioned. Therefore, only curves 1 and 4 in figure 1.2 are described by the Tait model, while curve 3 is supposed to coincide with curve 1, and curve 5 is degenerated to a point.

An (also phenomenological) model that describes curves 3 and 5 more accurately is the so-called KAHR model (after Kovacs-Aklonis-Hutchinson-Ramos (see Kovacs *et al.* (1979); Greener *et al.* (1991); Tribone and O'Reilly (1989); Ramos *et al.* (1988)). The specific volume is written as the sum of the equilibrium value ν_∞ (i.e. ν for $t \rightarrow \infty$) and a part that describes the deviation from equilibrium:

$$\nu = \nu_\infty(1 + \delta) \quad (2.9)$$

By definition ν_∞ depends on temperature and pressure only. Equations (2.6) and (2.7) for the melt are used to describe the equilibrium behaviour ν_∞ (using the melt constants for above and below T_g). The normalised deviation from equilibrium, δ , is written as:

$$\delta(t) = \int_{-\infty}^t (-\Delta\alpha\dot{T} + \Delta\kappa\dot{p})\zeta_\delta(t, t') dt' \quad (2.10)$$

$$\zeta_\delta(t, t') = \exp \left[- \left(\int_{t'}^t \frac{dt''}{\tau_\delta} \right)^\beta \right] \quad (2.11)$$

with

$$\tau_\delta = \tau_{\delta 0} a_{T_\delta} a_p a_\delta \quad (2.12)$$

$$a_{T_\delta} = \exp(-\theta (T - T_{\delta r})) \quad (2.13)$$

$$a_p = \exp(bp) \quad (2.14)$$

$$a_\delta = \exp \left(\frac{-(1-x)\theta\delta}{\Delta\alpha} \right) \quad (2.15)$$

and $\dot{T} = \frac{DT}{Dt'}$ and $\dot{p} = \frac{Dp}{Dt'}$ the time derivative of temperature and pressure, respectively, and $\Delta\alpha$, $\Delta\kappa$ the difference in thermal expansion and isothermal compressibility between the fluid and the glassy state. Instead of introducing a discrete spectrum of relaxation times, a KWW (Kohlrausch-Williams-Watts, see Kohlrausch (1847); Williams and Watts (1970)) fractional exponential law is used for ζ_δ . The relaxation time τ_δ is written as a reference relaxation time $\tau_{\delta 0}$ (for $T = T_{\delta r}, p = 0, \delta = 0$), while shift factors a are used for pressure, temperature and structure. The extra material parameters are θ , b , x and β ($0 \leq \beta \leq 1$). The value $\beta = 1$ corresponds to a single relaxation time. The closer β is to zero, the wider the relaxation time distribution. The parameter x represents the relative contribution to the shift factor of a change in structure parameter δ with respect to the temperature contribution. The material parameters can be fitted on measurements of ν as a function of time for several thermomechanical histories (see Kovacs *et al.* (1979) and Chapter 4).

2.2.2 Cauchy stress tensor

The Cauchy stress tensor is used for the determination of the flow kinematics, the residual stresses and elastic recovery after ejection. Residual stresses are split into a thermally and pressure induced stress (or thermal stress for short) on the one hand, and a flow-induced stress on the other. In principle the same constitutive relation could be used for all distinct cases. This would, however, be highly impractical and it is unnecessary as well, so for all four aspects (the constitutive equation to be used for the momentum equation, the thermal stresses, the flow-induced stresses and the elastic recovery) a separate constitutive equation is employed that includes all relevant aspects with a minimum of computational effort:

Computation of flow kinematics

The flow during injection moulding is practically always dominated by the kinematic boundary conditions: no slip at the mould walls or solidified layers and a prescribed flow at the gate. The type of constitutive equation for the stress tensor in the momentum equation only marginally influences the flow kinematics of the polymer melt, as long as it accurately describes the shear viscosity. In order to illustrate this statement, Baaijens and Douven (1990) computed the residual stresses in an injection moulded rectangular strip using both a coupled and a decoupled method. The coupled method uses a non-linear viscoelastic constitutive equation (Leonov model) for the stress tensor in the momentum equation to calculate both kinematics and stresses in full interdependence. The decoupled method calculates both quantities independently using for the former a generalised Newtonian model (the steady state Leonov model). The flow kinematics thus computed is subsequently used as input data for the full viscoelastic Leonov model in order to compute the stresses. The difference in residual stresses between the coupled and the decoupled approach turned out to be less than ten percent. In some situations, e.g. at bifurcations, the assumption of the kinematic boundary conditions dominating the flow kinematics will be violated. However, given the local character of the flow near bifurcations, the decoupled approach will still be used because it is much more efficient from a computational point of view.

In the generalised Newtonian model, melt elasticity is neglected, as is the bulk viscosity, and the shear viscosity η only depends on pressure p , temperature T and the deviatoric part of the rate of deformation tensor \mathbf{D}^d :

$$\boldsymbol{\sigma} = -p\mathbf{I} + \boldsymbol{\sigma}^d \quad (2.16)$$

$$\boldsymbol{\sigma}^d = 2\eta\mathbf{D}^d \quad (2.17)$$

$$\eta = \eta(p, T, \mathbf{D}) \quad (2.18)$$

where $\boldsymbol{\sigma}^d$ is the deviatoric part of the Cauchy stress tensor. For practical reasons a further specification of equation (2.18) is postponed to section 2.3.

Computation of the flow-induced residual stress

Flow-induced stresses arise from (mainly shear) deformation of the polymer during the filling and postfilling stages of the injection moulding process. In Flaman (1990); Baaijens (1991); Douven (1991) it is shown that the compressible Leonov model is capable of predicting this type of residual stress

with reasonable accuracy. The basic aspects of the model are summarised here for reference only. For a more elaborate description the reader is referred to the references above and Akkerman (1993).

The deformation $\mathbf{F} = (\bar{\nabla}_0 \bar{x})^c$ is multiplicatively split into an elastic (\mathbf{F}_e) and a plastic (\mathbf{F}_p) part: $\mathbf{F} = \mathbf{F}_e \cdot \mathbf{F}_p$. The volume change corresponding to the plastic part is taken zero, i.e. $I_3^{\mathbf{F}_p} = \det(\mathbf{F}_p) = 1$ and, consequently, $I_3^{\mathbf{F}} = I_3^{\mathbf{F}_e} = \det(\mathbf{F}_e)$. Subsequently, the volumetric contribution to \mathbf{F}_e is separated from the deviatoric part by:

$$\mathbf{F}_e = (I_3^{\mathbf{F}})^{\frac{1}{3}} \bar{\mathbf{F}}_e, \quad (2.19)$$

The associated Finger tensors are:

$$\mathbf{B} = \mathbf{F} \cdot \mathbf{F}^c, \quad \mathbf{B}_e = \mathbf{F}_e \cdot \mathbf{F}_e^c, \quad \bar{\mathbf{B}}_e = \bar{\mathbf{F}}_e \cdot \bar{\mathbf{F}}_e^c. \quad (2.20)$$

The velocity gradient tensor is defined as $\mathbf{L} = (\bar{\nabla} \bar{v})^c \doteq \dot{\mathbf{F}} \cdot \mathbf{F}^{-1}$. The Cauchy stress tensor is considered to be the sum of an elastic and a viscous part: $\boldsymbol{\sigma} = \boldsymbol{\sigma}_e + \boldsymbol{\sigma}_v$. The elastic stress is split into a hydrostatic part and a deviatoric part (equation (2.21)). For the deviatoric viscous part of $\boldsymbol{\sigma}$ equation (2.23) is employed. Adopting multiple modes (m_L), the deviatoric elastic part is given by equation (2.22). For each mode j the Finger tensor $\bar{\mathbf{B}}_{ej}$ is solved from equation (2.24). \mathbf{D}_{pj} is given by equation (2.25).

$$\boldsymbol{\sigma} = -p\mathbf{I} + \boldsymbol{\sigma}_e^d + \boldsymbol{\sigma}_v \quad (2.21)$$

$$\boldsymbol{\sigma}_e^d = \sum_{j=1}^{m_L} \frac{\eta_{Lj}}{\tau_{Lj}} \bar{\mathbf{B}}_{ej}^d \quad (2.22)$$

$$\boldsymbol{\sigma}_v = 2\eta_r \mathbf{D}^d \quad (2.23)$$

$$\dot{\bar{\mathbf{B}}}_{ej} = (\mathbf{L}^d - \mathbf{D}_{pj}) \cdot \bar{\mathbf{B}}_{ej} + \bar{\mathbf{B}}_{ej} \cdot (\mathbf{L}^{dc} - \mathbf{D}_{pj}) \quad (2.24)$$

$$\mathbf{D}_{pj} = \frac{1}{4\tau_{Lj}} (\bar{\mathbf{B}}_{ej}^d - \bar{\mathbf{B}}_{ej}^{-d}) \quad (2.25)$$

Time-temperature superposition is applied, assuming thermorheologically simple behaviour, which leads to the following expressions for the Leonov viscosities η_{Lj} and relaxation times τ_{Lj} (elastic part) and the viscosity η_r (viscous part) respectively:

$$\eta_{Lj}(p, T) = a_{T_L}(p, T) \eta_{Lj0}, \quad \tau_{Lj}(p, T) = a_{T_L}(p, T) \tau_{Lj0}, \quad (2.26)$$

$$\eta_r(p, T) = a_{T_L}(p, T) \eta_{r0} \quad (2.27)$$

where viscosities η_{Lj0} and relaxation times τ_{Lj0} are determined at a reference temperature (T_{Lr}) and pressure. Note that no vertical shift factor is incorporated in η_{Lj} and η_r . For the Leonov shift factor a_{TL} the classical WLF (Williams-Landel-Ferry, see Williams *et al.* (1955)) equation is used:

$$a_{TL} = \exp\left(\frac{-c_{L1}(T - T_{Lr})}{c_{L2} + T - T_{Lr}}\right) \quad (T \geq T_g) \quad (2.28)$$

A pressure dependence of a_{TL} is incorporated by means of the pressure dependent reference temperature $T_{Lr} = T_{Lr}(p = 0) + s_0 p$, using the pressure dependence of T_g (see Hieber, 1987). Material parameters η_{Lj0} , τ_{Lj0} , η_{r0} , c_{L1} and c_{L2} can be determined by oscillatory shear experiments (see e.g. Douven, 1991). Below T_g , the deformation is considered zero and relaxation times are taken infinite. In other words, the stress present when passing the glass transition temperature is frozen in permanently.

Computation of the thermally and pressure induced residual stress

These stresses arise from the inhomogeneous cooling of the product in combination with the pressure that is applied during cooling. Unlike flow-induced stresses, thermal stresses are not caused by large deformations and, consequently, a linear thermoviscoelastic model is used. A formal derivation of this model is given in Douven (1991), appendix D. Here, only a straightforward derivation is given.

The Cauchy stress tensor is split into a hydrostatic pressure and a deviatoric part:

$$\boldsymbol{\sigma} = -p^h \mathbf{I} + \boldsymbol{\sigma}^d \quad (2.29)$$

An expression for the hydrostatic pressure $p^h(T, \nu)$ can be derived from equation (2.9), substituted into the continuity equation (2.1):

$$\begin{aligned} \frac{\dot{\nu}}{\nu} &= \frac{\dot{\nu}_\infty}{\nu_\infty} + \frac{\dot{\delta}}{1 + \delta} \\ &= \alpha_\infty \dot{T} - \kappa_\infty \dot{p} + \frac{\dot{\delta}}{1 + \delta} \end{aligned} \quad (2.30)$$

$$= \text{tr}(\mathbf{D}), \quad (2.31)$$

where α_∞ , κ_∞ are the thermal expansion coefficient and the isothermal compressibility coefficient, respectively, for the equilibrium behaviour, defined as

$$\alpha_\infty = \frac{1}{\nu_\infty} \left(\frac{\partial \nu_\infty}{\partial T} \right)_p, \quad \kappa_\infty = -\frac{1}{\nu_\infty} \left(\frac{\partial \nu_\infty}{\partial p} \right)_T. \quad (2.32)$$

For small deformations, the rate of deformation tensor \mathbf{D} can be approximated by $\dot{\boldsymbol{\varepsilon}}$, with $\boldsymbol{\varepsilon} = 1/2[(\vec{\nabla}\vec{u}) + (\vec{\nabla}\vec{u})^c]$ and \vec{u} the total displacement field. When no relevant temperature and pressure effects exist for $t \leq 0$, the hydrostatic pressure $p^h(t)$ can be written as:

$$p^h(t) = \int_0^t \left(\frac{\alpha_\infty}{\kappa_\infty} \dot{T} + \frac{\dot{\delta}}{\kappa_\infty(1+\delta)} - \frac{1}{\kappa_\infty} \text{tr}(\dot{\boldsymbol{\varepsilon}}) \right) dt' \quad (2.33)$$

When there are no deformation effects before $t = 0$ and thermorheologically simple material behaviour is assumed, the deviatoric part of the Cauchy stress tensor is written as:

$$\boldsymbol{\sigma}^d = 2 \sum_{j=1}^{m_M} \int_0^t G_{Mj} \zeta_{Mj}(t, t') \dot{\boldsymbol{\varepsilon}}^d dt' \quad (2.34)$$

where the reduced relaxation modulus ζ_{Mj} is defined as:

$$\zeta_{Mj}(t, t') = \exp \left(- \int_{t'}^t \frac{1}{\tau_{Mj}} dt'' \right) \quad (2.35)$$

Analogous to the non-linear viscoelastic Leonov model, time-temperature superposition is applied to describe the pressure and temperature dependence of the Maxwell viscosities η_{Mj} and relaxation times τ_{Mj} :

$$\eta_{Mj}(p, T) = a_{T_M}(p, T) \eta_{Mj0}, \quad \tau_{Mj}(p, T) = a_{T_M}(p, T) \tau_{Mj0}, \quad (2.36)$$

where η_{Mj0} , τ_{Mj0} are values for the modal shear viscosities and relaxation times at a reference temperature and pressure. Again no vertical shift factor is incorporated in η_{Mj} . For temperatures above T_g , the WLF equation is used to describe the time-temperature shift function a_{T_M} for shear behaviour while below T_g an Arrhenius expression is chosen:

$$a_{T_M} = \exp \left(- \frac{c_{M1}(T - T_{Mr})}{c_{M2} + T - T_{Mr}} \right) \quad (T \geq T_g), \quad (2.37)$$

$$a_{T_M} = \exp(-c_{M3}(T - T_{Mr})) \quad (T < T_g). \quad (2.38)$$

Pressure dependence is incorporated in a_{T_M} like in a_{T_L} as described previously. To incorporate the effect of physical ageing on the shear modulus (see e.g. Struik (1978)), a δ -dependence in the shift factor could be introduced, like e.g. in equation (2.15). However, no attention is paid to this effect in this study. As shown by Douven (1991) this Maxwell model can be seen as

a linearised Leonov model. As the Leonov parameters are determined by linear viscoelastic measurements, the values of the parameters of the linear Maxwell model, indexed M , are equal to the corresponding parameters of the non-linear Leonov model, indexed L . Parameter c_{M3} , which is missing in the temperature shift function in the Leonov model, is determined by additional linear viscoelastic measurements below T_g (see Douven (1991), Zoetelief *et al.*).

A viscous-elastic model (see appendix C) for the deviatoric stress can be derived from the present model taking $G_{Mj} = \eta_{Mj}/\tau_{Mj} = G/m_M, \tau_{Mj} \rightarrow \infty$ for $T \leq T_g$ and $G_{Mj} = 0, \tau_{Mj} = 0$ for $T > T_g$ into equations (2.34), (2.35). Here G is a constant shear modulus for the solidified polymer and zero for the polymer melt. The hydrostatic stress can be modelled similarly, taking $\tau_\delta \rightarrow \infty$ for $T \leq T_g$, and $\tau_\delta = 0$ for $T > T_g$ in equation (2.12).

The right hand sides second term of equation (2.33) incorporates viscoelasticity of the bulk modulus, as it forms the history dependent part of the volumetric strain.

Computation of elastic recovery

Struik (1990) has shown that dimensional instability due to internal stresses can be conceived of as creep as a consequence of these stresses. He performed a number of experiments on several amorphous thermoplastics to establish the influence of stress and deformation above T_g on the dimensional stability below T_g . After annealing, rod shaped samples were twisted or uniaxially strained at a temperature above T_g under a constant stress or constant deformation rate. Within 10 minutes the samples were cooled to a temperature below T_g and the stress was removed. Three types of experiments were performed. First, the stress level per sample was kept constant, but varied from sample to sample adjusting the temperature, while the total deformation and deformation time was kept the same. Second, the stress level was kept the same for all samples, but the total deformation varied. Third, the deformation rate was kept constant under an increasing stress. For tensile and shear stresses below 8 MPa it was concluded that the dimensional instability is determined by the stress acting on the material when passing the glass transition temperature. The stress and temperature history before that point in time proved to be irrelevant. When the material is more than 5 to 15 K below the deformation temperature, the strains after unloading are governed by the compliance of the material at that temperature as a function of time, and by the internal stress present when passing the glass

transition. This creep behaviour can be modelled using a linear viscoelastic isotropic model when the occurring stresses are below the linearity limit of the material under consideration and the temperature of the material is below its glass transition temperature.

It could be concluded that the frozen-in stress, caused by deformation during the filling and packing stage, is the origin of elastic recovery after ejection of the product. This recovery can be described by the compliance of the material and the (constant) frozen-in flow-induced stress. Only the reversible part of the deformation above T_g can lead to the creep effect, so only the elastic part of equation (2.21) is considered as an extra load after demoulding.

Rather than a constitutive equation for the stress in terms of deformation, here an equation for the strain is given in terms of stress. The volumetric part of the strain is governed by the KAHR model (equation (2.9)) and the mass balance (equation (2.1)). The deviatoric part of the strain is described by a generalised Voigt model (see Ferry, 1980).

$$\epsilon_c^d = \frac{1}{2} \left[(J_g + t/\eta_K) \sigma^d + \sum_{j=1}^{m_K} \int_{-\infty}^t J_j (1 - \zeta_{Kj}) \dot{\sigma}^d dt' \right] \quad (2.39)$$

with J_j the (shear) creep compliance of mode j , J_g the instantaneous compliance and η_K the viscosity incorporating viscous flow. The expression for ζ_{Kj} is similar to ζ_{Mj} , given by equation (2.35):

$$\zeta_{Kj}(t, t') = \exp \left(- \int_{t'}^t \frac{1}{\tau_{Kj}} dt'' \right) \quad (2.40)$$

Again thermorheologically simple material behaviour is assumed, leading to the following expression for viscosity, relaxation time and shear compliance:

$$\eta_{Kj}(p, T) = a_{T_K}(p, T) \eta_{Kj0}, \quad \tau_{Kj}(p, T) = a_{T_K}(p, T) \tau_{Kj0}, \quad (2.41)$$

$$J_j = \frac{\tau_{Kj}}{\eta_{Kj}} \quad (2.42)$$

As equation (2.39) is only valid below T_g , a_{T_K} is only specified for this temperature range:

$$a_{T_K} = e^{-c_{K3}(T-T_{Kc})} \quad (T < T_g). \quad (2.43)$$

Although usually creep experiments are performed to find the relevant material parameters, here the same viscoelastic measurements are employed, that are used for determining the parameters of the Maxwell model (equation (2.34)). The procedure is elucidated in Chapter 4.

2.2.3 Heat conduction and internal energy

The constitutive equations used for the thermal properties are:

$$\vec{h} = -\lambda \cdot \vec{\nabla}T \quad (2.44)$$

$$\lambda = \lambda(p, T)$$

$$\dot{e} = c_p \dot{T} + \frac{p}{\rho^2} \dot{\rho} + \frac{T}{\rho^2} \left(\frac{\partial \rho}{\partial T} \right)_p \dot{p} \quad (2.45)$$

$$c_p = c_p(p, T)$$

where c_p is the thermal capacity at constant thermodynamic pressure and λ is the thermal conductivity tensor. Equation 2.44 is known as Fourier's law. Equation (2.45) is derived in e.g. Sitters (1988). Chiang *et al.* (1991b) proposed the following equation for c_p :

$$c_p(T) = c_{p1} + c_{p2}(T - c_{p5}) + c_{p3} \tanh(c_{p4}(T - c_{p5})) \quad (2.46)$$

2.3 Thin film approximation

In this study only thin-walled products are considered, fed by a runner system. In this section only the cavity is considered. Runners and runner-like product parts are treated in appendix E. The set of equations given in the previous sections can be written with respect to a local base, shown in figure 2.1. The typical flow kinematics justify the following assumptions, which will be used to simplify the set of equations:

1. The inertial and body forces are negligible compared to the viscous forces.
2. The product can be described by a combination of thin flat geometries.
3. The specific heat source is negligible.

Based on these basic assumptions, the following remarks can be made:

1. The pressure is constant across the wall thickness.

2. The velocity in thickness direction is negligible compared to the velocity parallel to the midplane.
3. The velocity gradient parallel to the midplane is negligible compared to the velocity gradient in the perpendicular direction.
4. For computation of the stress tensor in the balance equation, elongational flow is negligible compared to shear flow.
5. Thermal conduction parallel to the midplane is negligible compared to the conduction in thickness direction.
6. The extra pressure drop due to sudden changes in thickness or at junctions and corners is negligible.

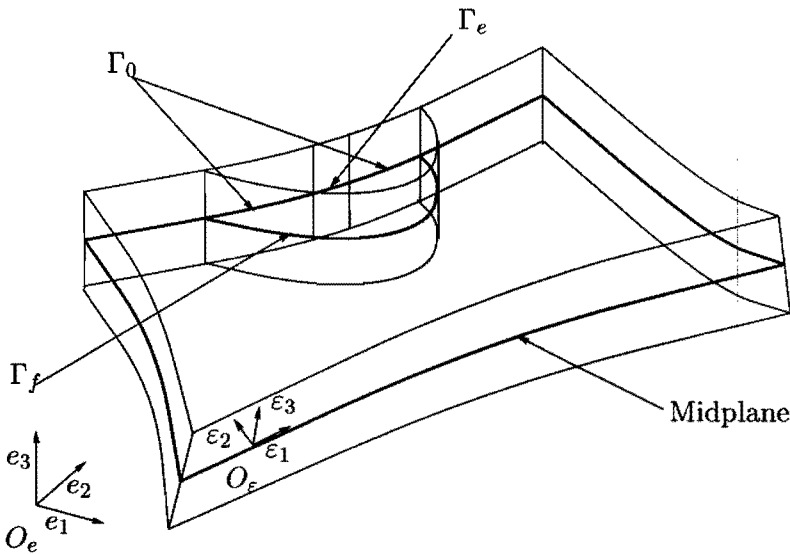


Figure 2.1: Definition of local coordinates, domains and boundaries for cavities

It is possible to use the shear rate $\dot{\gamma}$ in stead of D^d in the constitutive relations, with

$$\dot{\gamma} = \left| \frac{\partial \bar{v}^*}{\partial x_3^\varepsilon} \right|, \quad (2.47)$$

where \vec{v}^* indicates the velocity parallel to the midplane (see figure 2.1) and x_3^ε is the local thickness coordinate. The steady state Leonov model is employed to specify equation (2.18) (see Douven, 1991):

$$\eta = \eta_{r0} a_{TL} + \sum_{j=1}^{m_L} \left(\frac{2\eta_{Lj} a_{TL}}{\sqrt{1 + 4(\dot{\gamma}\tau_{Lj} a_{TL})^2}} \right) \quad (2.48)$$

$$a_{TL} = \exp \left(\frac{-c_{L1}(T - T_{Lr})}{c_{L2} + T - T_{Lr}} \right) \quad (2.49)$$

$$T_g = T_{g0} + s_0 p \quad (2.50)$$

with η_{r0} the viscosity at T_{g0} for the viscous part of the deformation, η_{Lj} the viscosity for mode j and τ_{Lj} the corresponding relaxation time. An alternative model for the shear viscosity is the 7-constant Cross model.

$$\eta(p, T, \dot{\gamma}) = \frac{\eta_C(p, T)}{1 + (\eta_C(p, T)\dot{\gamma}/\tau_{C0})^{(1-n)}} \quad (2.51)$$

$$\eta_C = \eta_{C0} \exp \left(\frac{-c_{C1}(T - T_{Cr} - s_0 p)}{c_{C2} + T - T_{Cr}} \right)$$

Using the three assumptions and the constitutive equations (2.16), (2.17), (2.44) and (2.45), the balance equations can be rewritten as (see e.g. Sitters (1988); Boshouwers and van der Werf (1988); Douven (1991)):

$$\vec{\nabla}^* \cdot \vec{v}^* + \frac{\partial v_3^\varepsilon}{\partial x_3^\varepsilon} = -\frac{\dot{\rho}}{\rho}, \quad (2.52)$$

$$\vec{\nabla}^* p = \frac{\partial}{\partial x_3^\varepsilon} \left(\eta \frac{\partial \vec{v}^*}{\partial x_3^\varepsilon} \right), \quad \frac{\partial p}{\partial x_3^\varepsilon} = 0, \quad (2.53)$$

$$\rho c_p \dot{T} = \frac{\partial}{\partial x_3^\varepsilon} \left(\lambda \frac{\partial T}{\partial x_3^\varepsilon} \right) + \eta \dot{\gamma}^2 - \frac{T}{\rho} \left(\frac{\partial \rho}{\partial T} \right)_p \dot{p} \quad (2.54)$$

Especially the second assumption is not valid in the flow front region. Therefore, special attention could be paid to the flow kinematics in this region as it is not dominated by shear but contains a major elongational component, affecting the internal stress state. Material derivatives are influenced as well, as particles from the core region end up at the mould wall. This is depicted in figure 2.2a, where the mould walls have the relative velocity opposite to the average front velocity, and solidified layers are omitted.

The model applied for the flow front is depicted in figure 2.2b. All elongational flow is neglected, which may lead to serious errors in the prediction

of the flow-induced stress at the very surface layer of products¹ (see Jansen, 1993). The residence time in the front region is assumed to be zero for all particles. As a consequence the flow-front is considered to be isothermal. Although the residence time in the flow front does influence the exact location where particles end up in the product, the gradient in flow direction of the relevant quantities is relatively small, so that incorporation of the residence time, although quite well possible (see Zoetelief, 1995) does not have the highest priority. Given the position of entrance into the front region, the position where the particle exits is based on the local velocity profile (indicated on the left in figure 2.2b) and the mass balance. The material that comes into contact with the cold mould cools from the temperature of the core at a high rate. Incorporation of this effect is important for an accurate prediction of the density distribution.

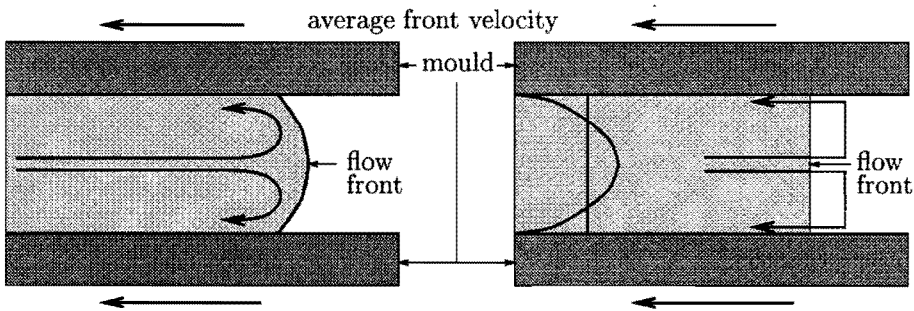


Figure 2.2: Left (a): Schematic illustration of the flow front kinematics. Right (b): Illustration of the front model applied

2.4 Resulting set of equations

Given the assumptions of the thin film approximation, the set of balance and constitutive equations can be simplified. This results in a full set of equations for quantities related to the process, like pressure, temperature and velocity, equations for the structure parameters, like density and residual stresses and the final product properties, like warpage and elastic recovery.

¹Wimberger-Friedl (1995) showed that the high level of stress may also be caused by the “squeeze flow” or unidirectional shrinkage in thickness direction, that occurs during solidification of the surface layers.

Pressure

Integration of the equations (2.53)₁ along the x_3^ε coordinate yields:

$$\frac{\partial \vec{v}^*}{\partial x_3^\varepsilon} = \frac{1}{\eta} \left(x_3^\varepsilon \vec{\nabla}^* p + \vec{c}^* \right) \quad (2.55)$$

where \vec{c}^* is an integration constant. Integration of equations (2.55) along x_3^ε leads to:

$$\vec{v}^*(x_3^\varepsilon) = \int_{\alpha^-}^{x_3^\varepsilon} \frac{\partial \vec{v}^*}{\partial \chi} d\chi = \quad (2.56)$$

$$\vec{\nabla}^* p \int_{\alpha^-}^{x_3^\varepsilon} \frac{\chi}{\eta} d\chi + \vec{c}^* \int_{\alpha^-}^{x_3^\varepsilon} \frac{1}{\eta} d\chi \quad (\alpha^- \leq x_3^\varepsilon \leq \alpha^+) \quad (2.57)$$

where α^- , α^+ are the positions of the solidification fronts. The constant \vec{c}^* can be determined as follows, using:

$$F_n = \int_{\alpha^-}^{\alpha^+} \frac{\chi^n}{\eta} d\chi \quad (n = 0, 1, 2) \quad (2.58)$$

and the assumption that $\vec{v}^*(\alpha^+) = 0$, \vec{c}^* can be written as:

$$\vec{c}^* = -\frac{F_1}{F_0} \vec{\nabla}^* p \quad (2.59)$$

and consequently

$$\vec{v}^*(x_3^\varepsilon) = \int_{\alpha^-}^{x_3^\varepsilon} \frac{1}{\eta} \left(\chi - \frac{F_1}{F_0} \right) d\chi \vec{\nabla}^* p \quad (2.60)$$

Integration of equation (2.60) over h leads to:

$$\int_{-\frac{h}{2}}^{\frac{h}{2}} \vec{v}^* d\chi = \int_{\alpha^-}^{\alpha^+} \vec{v}^* d\chi = -S \vec{\nabla}^* p, \quad S = F_2 - \frac{F_1^2}{F_0} \quad (2.61)$$

Similarly, integration of the continuity equations 2.52 over the total thickness yields:

$$\int_{-\frac{h}{2}}^{\frac{h}{2}} \vec{\nabla}^* \cdot \vec{v}^* d\chi + \int_{-\frac{h}{2}}^{\frac{h}{2}} \frac{\partial v_3^\varepsilon}{\partial \chi} d\chi = - \int_{-\frac{h}{2}}^{\frac{h}{2}} \frac{\dot{\rho}}{\rho} d\chi \quad (2.62)$$

The second term of equation (2.62) equals the relative velocity of the two mould walls in x_3^ε direction $\frac{\partial h}{\partial t}$, due to mould elasticity and is written as:

$$\frac{\partial h}{\partial t} = \frac{\partial h}{\partial p} \frac{\partial p}{\partial t} = C \frac{\partial p}{\partial t} \quad (2.63)$$

with C the compliance of the mould. Substitution of (2.61)₁ into (2.62) yields:

$$\vec{\nabla}^* \cdot (S \vec{\nabla}^* p) = \int_{-\frac{h}{2}}^{\frac{h}{2}} \frac{\dot{\rho}}{\rho} d\chi + C \frac{\partial p}{\partial t} \quad (2.64)$$

Finally, equations (2.30) and (2.64) give:

$$-\vec{\nabla}^* \cdot (S \vec{\nabla}^* p) + \int_{-\frac{h}{2}}^{\frac{h}{2}} \kappa_\infty \dot{p} d\chi + C \frac{\partial p}{\partial t} = \int_{-\frac{h}{2}}^{\frac{h}{2}} \left(\alpha_\infty \dot{T} + \frac{\dot{\delta}}{1 + \delta} \right) d\chi \quad (2.65)$$

Of course boundary conditions are required to solve these equations. For the injection area of the cavity (Γ_e , figure 2.1), either a volume flux, or a pressure can be prescribed. The volume flux is usually prescribed during filling, resulting in an inhomogeneous Neumann boundary condition for the pressure equation, based on equation (2.61).

$$q = S \vec{\nabla}^* p \cdot \vec{n}^* \quad (\Gamma_e) \quad (2.66)$$

Here $q(\vec{x}^*, t)$ denotes a prescribed volume flux per unit of length, \vec{n} is the unit outward normal of Ω_c , with Ω_c the filled area of the midplane. When, during filling, the maximum machine pressure is reached, this pressure must be used as a boundary condition, which results into a Dirichlet boundary condition:

$$p = p_e \quad (\Gamma_e) \quad (2.67)$$

During packing and holding the pressure is prescribed at Γ_e . During cooling the boundary condition at Γ_e equals the one for Γ_0 (see below). At the flow front Γ_f , i.e. the interface between polymer and air inside the cavity, the pressure equals the ambient pressure p_{atm} :

$$p = p_{atm} \quad (\Gamma_f) \quad (2.68)$$

On Γ_0 the volume flux through the boundaries is zero. Using equation (2.61), this results into a homogeneous Neumann boundary condition:

$$\vec{\nabla}^* p \cdot \vec{n}^* = 0 \quad (\Gamma_0) \quad (2.69)$$

Solution of equations (2.65) gives the pressure field inside the mould. The velocity field can be computed using equations (2.52) and (2.60). To compute the coefficients, the temperature field must be known. This can be computed solving the temperature equation, formulated below.

Temperature

For the cavity, the temperature equation reads (see equation (2.54)):

$$-\frac{\partial}{\partial x_3^\varepsilon} \left(\lambda \frac{\partial T}{\partial x_3^\varepsilon} \right) + \rho c_p \dot{T} + \frac{T}{\rho} \left(\frac{\partial \rho}{\partial T} \right)_p \dot{p} = \eta \dot{\gamma}^2 \quad (2.70)$$

Boundary conditions and initial values are required to solve this convection-diffusion equation. During filling, the polymer is in contact with the air at the flow front (Γ_f). Here a zero heat flux is prescribed:

$$\vec{\nabla}^* T \cdot \vec{n}^* = 0. \quad (2.71)$$

This boundary condition is, although far from realistic, also used for Γ_0 due to lack of actual data here. During filling, packing, holding and cooling, the polymer is in contact with the mould at the top (Γ_+) and bottom (Γ_-) plane. Here either the (mould) temperature is prescribed (Dirichlet boundary condition) or the heat flux into the mould (Biot boundary condition):

$$T = T_w^+ \quad \text{or} \quad \lambda \frac{\partial T}{\partial x_3^\varepsilon} = H_m^+(T - T_m^+) \quad (\Gamma^+) \quad (2.72)$$

$$T = T_w^- \quad \text{or} \quad \lambda \frac{\partial T}{\partial x_3^\varepsilon} = H_m^-(T - T_m^-) \quad (\Gamma^-) \quad (2.73)$$

Here T_w^+ , T_w^- are mould wall temperatures, T_m^+ , T_m^- are the temperatures of the medium in the cooling channels and H_m^+ , H_m^- are the effective heat transfer coefficients from polymer to cooling medium. These parameters change when the product is ejected from the mould and cooled by the air:

$$T = T_a \quad \text{or} \quad \lambda \frac{\partial T}{\partial x_3^\varepsilon} = H_a(T - T_a) \quad (\Gamma^+, \Gamma^-) \quad (2.74)$$

Here T_a is the ambient temperature and H_a is the heat transfer coefficient from polymer to air. At the injection area (Γ_e) the temperature is set to the injection (or entrance) temperature T_e :

$$T = T_e \quad (\Gamma_e) \quad (2.75)$$

Density

Given the solutions of equations (2.65) and (2.70), equation (2.10) can be solved. Since the coefficients in the pressure and temperature equations depend on density, these equations are coupled. Initially all material is above the glass transition temperature, so the initial value for δ is zero. Solution of equation (2.10) yields the density distribution across the entire product as a function of time.

Thermally and pressure induced stress

The thermal stresses can be calculated using equations (2.33) and (2.34), given the pressure of the fluid and the entire temperature history. A visco-elastic approximation can be applied instead using equation (C.1). After ejection, equation (2.2) is solved, assuming $\vec{f} = \vec{v} = \vec{0}$ and substituting for the stress tensor either equations (2.33) and (2.34) or equation (C.1). Sufficient kinematic constraints must be prescribed to prevent rigid body motion and rotation. The boundary load is assumed zero. In Chapter 3 it will be shown that, from the computed displacement field, the strains and stresses can be computed.

Orientation or flow-induced stress

The flow-induced stress is computed using equations (2.21) to (2.25). After substitution of 2.25, equation (2.24) can be written as:

$$\dot{\bar{\mathbf{B}}}_{ej} = \mathbf{L}^d \cdot \bar{\mathbf{B}}_{ej} + \bar{\mathbf{B}}_{ej} \cdot \mathbf{L}^{dc} - \frac{1}{2\tau_{Lj}} \left[\bar{\mathbf{B}}_{ej} \cdot \bar{\mathbf{B}}_{ej} - \mathbf{I} - \frac{1}{3} (tr(\bar{\mathbf{B}}_{ej}) - tr(\bar{\mathbf{B}}_{ej}^{-1})) \bar{\mathbf{B}}_{ej} \right]. \quad (2.76)$$

As an initial value, the solution for isothermal stationary flow is taken (see e.g. Akkerman, 1993). Elongational flow effects are neglected, so the influence of the fountain flow on orientation is not taken into account. Also the influence of cooling stresses before and during glass transition (which can be regarded as a squeeze flow, see equation (C.2)) on the degree of orientation is, although proven important (see Wimberger-Friedl, 1991, 1994), neglected. From the results of Tas (1994) it is known that the Leonov model poorly predicts the elongational viscosity at high shear rates for poly-ethylene. Models that perform better, such as Phan-Thien-Tanner, need separate elongational flow experiments to fit all parameters. However, these are not yet available for the material used in this study.

The shear rate is, with respect to the local base O_ε , written as:

$$\dot{\gamma}_1 = \frac{\partial v_1^\varepsilon}{\partial x_3^\varepsilon}, \quad \dot{\gamma}_2 = \frac{\partial v_2^\varepsilon}{\partial x_3^\varepsilon}. \quad (2.77)$$

From the equations (2.55) and (2.59) shear rates can be computed from the pressure gradient. Matrix \underline{L}^d is written as:

$$\underline{L}^d = \underline{L} = \begin{bmatrix} 0 & 0 & \dot{\gamma}_1 \\ 0 & 0 & \dot{\gamma}_2 \\ 0 & 0 & 0 \end{bmatrix} \quad (2.78)$$

Let $B_{kl}(= B_{lk})$ denote the components of the tensor $\bar{\mathbf{B}}_{e_j}$ with respect to local base O_ε , then equation (2.76) can be written as:

$$\dot{B}_{11} = 2\dot{\gamma}_1 B_{13} - \frac{1}{\tau_{Lj}} \left[\frac{1}{2}(B_{11}^2 + B_{12}^2 + B_{13}^2 - 1) - \frac{1}{6}F_r B_{11} \right] \quad (2.79)$$

$$\dot{B}_{22} = 2\dot{\gamma}_2 B_{23} - \frac{1}{\tau_{Lj}} \left[\frac{1}{2}(B_{12}^2 + B_{22}^2 + B_{23}^2 - 1) - \frac{1}{6}F_r B_{22} \right] \quad (2.80)$$

$$\dot{B}_{33} = -\frac{1}{\tau_{Lj}} \left[\frac{1}{2}(B_{13}^2 + B_{23}^2 + B_{33}^2 - 1) - \frac{1}{6}F_r B_{33} \right] \quad (2.81)$$

$$\begin{aligned} \dot{B}_{12} &= \dot{\gamma}_1 B_{23} + \dot{\gamma}_2 B_{13} \\ &\quad - \frac{1}{\tau_{Lj}} \left[\frac{1}{2}(B_{12}(B_{11} + B_{22}) + B_{13}B_{23}) - \frac{1}{6}F_r B_{12} \right] \end{aligned} \quad (2.82)$$

$$\begin{aligned} \dot{B}_{13} &= \dot{\gamma}_1 B_{33} \\ &\quad - \frac{1}{\tau_{Lj}} \left[\frac{1}{2}(B_{13}(B_{11} + B_{33}) + B_{12}B_{23}) - \frac{1}{6}F_r B_{13} \right] \end{aligned} \quad (2.83)$$

$$\begin{aligned} \dot{B}_{23} &= \dot{\gamma}_2 B_{33} \\ &\quad - \frac{1}{\tau_{Lj}} \left[\frac{1}{2}(B_{23}(B_{22} + B_{33}) + B_{12}B_{13}) - \frac{1}{6}F_r B_{23} \right] \end{aligned} \quad (2.84)$$

with

$$F_r = B_{11} + B_{22} + B_{33} - \quad (2.85)$$

$$(B_{11}B_{22} + B_{11}B_{33} + B_{22}B_{33} - B_{12}^2 - B_{13}^2 - B_{23}^2) \quad (2.86)$$

The stationary solution is taken as an initial condition. After solution of this set of equations, \mathbf{B}_{e_j} is substituted into equation (2.22) and gives the elastic part of the deviatoric stress tensor. In order to determine the viscous part,

an expression for \underline{D}^d , the deviatoric part of the deformation rate tensor with respect to local base O_ε , must be known:

$$\underline{D}^d = \begin{bmatrix} 0 & 0 & \dot{\gamma}_1 \\ 0 & 0 & \dot{\gamma}_2 \\ \dot{\gamma}_1 & \dot{\gamma}_2 & 0 \end{bmatrix} \quad (2.87)$$

Equation (2.21) then finally gives the total stress tensor that is due to flow-induced orientation.

Shrinkage and warpage

A no-slip condition is prescribed in all cases at the mould walls Γ_-, Γ_+ . For geometrically complex products, this constrained quench assumption can be justified. Also for rectangular products this assumption is valid when the fluid core of the product is still under a sufficiently high hydrostatic pressure to ensure enough friction at the walls. Only when the pressure is zero and the product is not completely solidified, and after complete solidification, the no-slip condition may have to be abandoned. Little is known, however, on the friction between product and mould wall. Besides, the typical stress distribution across the thickness, that corresponds to the incorporation of boundary slip, has never been observed experimentally in injection moulded products (see Brucato *et al.*, 1989).

After demoulding, the momentum equation is solved again (see section 2.4) and from the computed displacements and rotations (or warpage), strains and thus shrinkage can be evaluated.

Creep

The stress tensor, as given in equation (2.21), forms the input for equation (2.39) at ejection of the product. It is assumed that, after demoulding, the frozen-in stress remains constant. Thus the latter equation can be written as:

$$\varepsilon_c^d = \frac{1}{2} \sigma^d \left(J_g + t/\eta_K + \sum_{j=1}^{m_K} J_j (1 - \zeta_{Kj}(t, t_e)) \right) \quad (2.88)$$

with t_e the moment of ejection and ζ_{Kj} as given by equation (2.40). From the computed (extra) strains an (extra) displacement field can be evaluated.

2.5 Discussion

Given the equations of balance and the constitutive equations for the Cauchy stress tensor, density, heat flux and internal energy, a set of equations is derived to describe the injection moulding process and the formation of the structure and the mechanical properties of the moulded product.

Three constitutive equations are proposed for the Cauchy stress tensor. Following a decoupled approach, a generalised Newtonian model is used in the momentum equation. A compressible Leonov model is employed for the computation of the flow-induced residual stress. This stress is taken as an external load for the computation of creep after demoulding, modelled by a multi-mode Voigt model. A linearised version of the Leonov model is used for the calculation of thermal residual stress, leading to shrinkage and warpage.

The set of equations is simplified, employing the thin film approximation. This leads to equations for pressure, shear rate, velocities, temperature. Equations for pressure and temperature are coupled via the density and the viscosity. After solution of these equations, pressure, temperature and density are used as input data for the computation of thermally and pressure induced stress, shrinkage and warpage, flow-induced residual stress and elastic recovery.

Chapter 3

Numerical Methods

In this chapter, the numerical methods are described that are applied to solve the equations, derived in Chapter 2. In section 3.1 an operator splitting technique is proposed for the approximation of material derivatives, resulting in an additional pure convection equation. As the transient equations cannot be solved analytically, they are discretised in time (3.2). Several equations are coupled, so an iterative procedure is required for this, which is elucidated in section 3.3. Finally, a description of the spatial discretisation is given, which leads to a finite element formulation of the equations (section 3.4).

3.1 Operator splitting

Since all terms of the temperature equation (2.70), except for the material derivatives, depend on the local thickness coordinate only, an operator splitting technique seems useful for the solution of these equations. For description of this method, a general convection-diffusion equation, defined for a two dimensional space, is treated (see also Press *et al.*, 1988, Chap. 19). Starting from:

$$-\vec{\nabla} \cdot D\vec{\nabla}u + \dot{u} = F \quad (3.1)$$

the convection-diffusion equation can be written as:

$$\frac{\partial u}{\partial t} = \mathcal{L}u \quad (3.2)$$

$$\mathcal{L}u = \mathcal{L}_1u + \mathcal{L}_2u \quad (3.3)$$

$$\mathcal{L}_1u = -\vec{v} \cdot \vec{\nabla}u \quad (3.4)$$

$$\mathcal{L}_2u = \vec{\nabla} \cdot D\vec{\nabla}u + F \quad (3.5)$$

The operator splitting technique applied consists of subsequent solution of:

$$\frac{\partial u}{\partial t} = \mathcal{L}_1 u \quad (3.6)$$

$$\frac{\partial u}{\partial t} = \mathcal{L}_2 u \quad (3.7)$$

The initial value for (3.6) equals that for the original equation (2.70). Only boundary conditions at inflow boundaries are required. The initial value for equation (3.7) is the solution of equation (3.6), which will be referred to as the convected value of u , denoted by u_c .

3.2 Temporal discretisation

The relevant equations are solved for a number of discrete moments in time t_i . The velocity field \vec{v}^* is assumed to be constant during a time step $\Delta t_i = t_i - t_{i-1}$ and is evaluated at t_i . All material derivatives are assumed to be constant as well and are approximated by:

$$\dot{u}_i \approx \frac{u_i - u_c}{\Delta t}. \quad (3.8)$$

Time dependent domain

During filling, the domains Ω_c and Ω_r change in time. Suppose the averaged speed $|\vec{v}^*|$ is known at the flow front Γ_f (see figure 2.1) at t_{i-1} . The location of this front at t_i is estimated by taking the enveloping curve of all “circles” in the midplane with $|\vec{v}^*|$ times $(t_i - t_{i-1})$ as a radius and with their midpoints located on the front at t_{i-1} . For the first time step, the average front velocity can be derived from the boundary conditions (2.66). For every following time step, these equations are evaluated at the front.

Convection equations

Despite of the higher accuracy of a Crank Nicholson method (see Zoetelief, 1995), the convection equation (3.6) is solved using an Euler implicit scheme:

$$\frac{u_i - u_{i-1}}{\Delta t_i} + \vec{v}_i^* \cdot \vec{\nabla}^* u_i = 0 \quad (3.9)$$

It is assumed that pressure and temperature fields are sufficiently “smooth”, so that the effects of numerical dispersion and diffusion are limited. This choice reduces memory requirements and increases the speed of the code.

Pressure and temperature equations

The pressure and temperature equations (2.65), (2.70) are discretised using an Euler implicit scheme. The coefficients are evaluated at the current time step t_i and therefore the equations have to be solved iteratively (see section 3.3).

Application of time discretisation and operator splitting to the pressure equation (2.65) leads to:

$$\begin{aligned}
 -\vec{\nabla}^* \cdot (S\vec{\nabla}^* p_i) + \frac{p_i}{\Delta t} \left[\int_{-\frac{h}{2}}^{\frac{h}{2}} \kappa_\infty d\chi + C \right] = \\
 \frac{1}{\Delta t} \int_{-\frac{h}{2}}^{\frac{h}{2}} \left(\alpha_\infty (T - T_c) + \frac{\delta - \delta_c}{1 + \delta} + p_c \kappa_\infty \right) d\chi + \\
 C \frac{p_{i-1}}{\Delta t} \quad (3.10)
 \end{aligned}$$

with p_c the solution of

$$\frac{\partial p}{\partial t} = -\vec{v}_i^* \cdot \vec{\nabla}^* p \quad (t_{i-1} \leq t \leq t_i) \quad (3.11)$$

(see the next section for the treatment of δ_c). Boundary conditions of equation (3.10) are listed in Chapter 2. For equation (3.11) the boundary condition at the gates is the local pressure at the previous time step. No other boundary conditions are required, not even on the flow front as the pressure is assumed to be constant across the gap width. The initial condition is the pressure distribution at $t = t_{i-1}$.

After time discretisation and incorporation of the operator splitting technique, the resulting equations for the temperature are:

$$-\frac{\partial}{\partial x_3^e} \left(\lambda \frac{\partial T_i}{\partial x_3^e} \right) + \frac{T_i}{\Delta t} \left[\rho c_p + \frac{1}{\rho} \left(\frac{\partial \rho}{\partial T_i} \right)_p (p - p_c) \right] = \eta \dot{\gamma}^2 + \rho c_p \frac{T_c}{\Delta t} \quad (3.12)$$

with T_c the solution of

$$\frac{\partial T}{\partial t} = -\vec{v}_i^* \cdot \vec{\nabla}^* T \quad (t_{i-1} \leq t \leq t_i) \quad (3.13)$$

Boundary conditions of equation (3.12) are listed in Chapter 2. At the inflow boundaries, the boundary condition for equation (3.13) is the injection

temperature. The initial value is T_{i-1} . As indicated in section 2.3, the flow front boundary needs special treatment in order to incorporate the convection from the core to the surface. For convenience treatment will be postponed to section 3.4. The initial condition for equation (3.13) is T_{i-1} , the temperature at the previous time step.

Density equation

Although other solution methods exist (see e.g. Hussain *et al.*, 1990), the fractional exponential formulation of the relaxation time spectrum in the KAHR model (equation (2.11)) is approximated by a discrete spectrum:

$$e^{-(\frac{t}{\tau_{\delta 0}})^\beta} \approx \sum_{j=1}^{m_\delta} w_j e^{-\frac{t}{\tau_{\delta j 0}}}, \quad \sum_{j=1}^{m_\delta} w_j = 1. \quad (3.14)$$

This enables an incremental formulation of $\delta_{j_i} = \delta_j(t_i)$, the contribution to δ for relaxation time j at t_i .

$$\delta_{j_i} = \zeta_{\delta j_i} \delta_{j_c} + \zeta_{\delta j_i} \int_{t_{i-1}}^{t_i} (-\Delta \alpha \dot{T}_i + \Delta \kappa \dot{p}_i) w_j \exp\left(-\int_{t'}^{t_{i-1}} \frac{dt''}{\tau_{\delta j}}\right) dt' \quad (3.15)$$

$$\zeta_{\delta j_i} = \exp\left(-\int_{t_{i-1}}^{t_i} \frac{dt''}{\tau_{\delta j}}\right) \quad (3.16)$$

Application of the trapezium rule for numerical integration and substitution of equation (2.12) leads to:

$$\delta_j(t_i) = \zeta'_{\delta j_i} \delta_{j_c} + \frac{\Delta t_i}{2} (-\Delta \alpha \dot{T}_i + \Delta \kappa \dot{p}_i) w_j (1 + \zeta'_{\delta j_i}) \quad (3.17)$$

$$\zeta'_{\delta j_i} = \exp\left[-\frac{\Delta t_i}{2\tau_{\delta j 0}} \left(\frac{1}{a_{T_i} a_{p_i} a_{\delta_i}} + \frac{1}{a_{T_{i-1}} a_{p_{i-1}} a_{\delta_{i-1}}}\right)\right] \quad (3.18)$$

As $\zeta'_{\delta j_i}$ depends on $\delta(t_i)$ itself, equation (3.17) has to be solved iteratively. A Picard iteration scheme is used. The time derivatives \dot{T} , \dot{p} are approximated by equation (3.8).

The term δ_c could be computed applying equation (3.11), but now for δ in stead of p . However, when $\delta \neq 0$ (so there may be a $\vec{\nabla}^* \delta \neq 0$), the material is more or less solidified, so \vec{v}^* is (almost) zero. Thus the convective term becomes negligible.

Thermal stress equation

For temporal discretisation of equations (2.33) and (2.34) it is assumed that time derivatives are constant during a time step. Like for δ_{j_i} in the previous section, an incremental formulation can be given for the hydrostatic and deviatoric parts of the stress tensor. Discretization of equation (2.33) and application of the trapezium rule for numerical integration results in:

$$p_i = p_{i-1} + \beta^\bullet \Delta T_i + \gamma^\bullet \Delta \delta_i - K^\bullet \text{tr}(\Delta \boldsymbol{\varepsilon}_i) \quad (3.19)$$

$$\beta^\bullet = \frac{1}{2} \left(\frac{\alpha_{\infty i}}{\kappa_{\infty i}} + \frac{\alpha_{\infty i-1}}{\kappa_{\infty i-1}} \right) \quad (3.20)$$

$$\gamma^\bullet = \frac{1}{2} \left(\frac{1}{\kappa_{\infty i}(1 + \delta_i)} + \frac{1}{\kappa_{\infty i-1}(1 + \delta_{i-1})} \right) \quad (3.21)$$

$$K^\bullet = \frac{1}{2} \left(\frac{1}{\kappa_{\infty i}} + \frac{1}{\kappa_{\infty i-1}} \right) \quad (3.22)$$

where ΔT_i , $\Delta \delta_i$, $\Delta \boldsymbol{\varepsilon}_i$ are the change in T , δ , $\boldsymbol{\varepsilon}$ respectively during time step Δt_i for the particle under consideration. Discretization of equation (2.34), again in combination with the application of the trapezium rule, leads to:

$$\sum_{j=1}^{m_M} \boldsymbol{\sigma}_{j_i}^d = \sum_{j=1}^{m_M} \zeta'_{Mj_i} \boldsymbol{\sigma}_{j_{i-1}}^d + 2G^\bullet \Delta \boldsymbol{\varepsilon}_i^d \quad (3.23)$$

$$G^\bullet = \sum_{j=1}^m \frac{G_j}{2} (1 + \zeta'_{Mj_i}) \quad (3.24)$$

$$\zeta'_{Mj_i} = \exp \left[-\frac{\Delta t_i}{2\tau_{Mj_0}} \left(\frac{1}{a_{TM_i}} + \frac{1}{a_{TM_{i-1}}} \right) \right] \quad (3.25)$$

The expression for the total Cauchy stress tensor at t_i can be summarised as:

$$\boldsymbol{\sigma}_i = \boldsymbol{\sigma}^\bullet + K^\bullet \text{tr}(\Delta \boldsymbol{\varepsilon}_i) \mathbf{I} + 2G^\bullet \Delta \boldsymbol{\varepsilon}_i^d \quad (3.26)$$

$$\boldsymbol{\sigma}^\bullet = -(p_{i-1} + \beta^\bullet \Delta T_i + \gamma^\bullet \Delta \delta_i) \mathbf{I} + \sum_{j=1}^m \zeta'_{Mj_i} \boldsymbol{\sigma}_{j_{i-1}}^d \quad (3.27)$$

Equation (3.26) can be written with respect to local base O_ε , thus eliminating the incremental strain component $\Delta \boldsymbol{\varepsilon}_{33}$:

$$\boldsymbol{\sigma}_i = \underline{M} \Delta \boldsymbol{\varepsilon} + \underline{g} \quad (3.28)$$

$$\boldsymbol{\sigma}^T = [\sigma_{11} \ \sigma_{22} \ \sigma_{12} \ \sigma_{23} \ \sigma_{13}], \quad (3.29)$$

$$\Delta \underline{\varepsilon}^T = [\Delta \varepsilon_{11} \quad \Delta \varepsilon_{22} \quad 2\Delta \varepsilon_{12} \quad 2\Delta \varepsilon_{23} \quad 2\Delta \varepsilon_{13}], \quad (3.30)$$

$$\underline{M} = \begin{bmatrix} a^\bullet & b^\bullet & 0 & 0 & 0 \\ b^\bullet & a^\bullet & 0 & 0 & 0 \\ 0 & 0 & G^\bullet & 0 & 0 \\ 0 & 0 & 0 & G^\bullet & 0 \\ 0 & 0 & 0 & 0 & G^\bullet \end{bmatrix}, \quad (3.31)$$

$$\underline{g} = \begin{bmatrix} \sigma_{11}^\bullet + \frac{\hat{b}}{\hat{a}}(\sigma_{33} - \sigma_{33}^\bullet) \\ \sigma_{22}^\bullet + \frac{\hat{b}}{\hat{a}}(\sigma_{33} - \sigma_{33}^\bullet) \\ \sigma_{12}^\bullet \\ \sigma_{23}^\bullet \\ \sigma_{13}^\bullet \end{bmatrix}, \quad (3.32)$$

$$\Delta \varepsilon_{33} = \frac{\sigma_{33} - \sigma_{33}^\bullet}{\hat{a}} - \frac{\hat{b}}{\hat{a}}(\Delta \varepsilon_{11} + \Delta \varepsilon_{22}), \quad (3.33)$$

$$\hat{a} = \frac{3K^\bullet + 4G^\bullet}{3}, \quad (3.34)$$

$$\hat{b} = \frac{3K^\bullet - 2G^\bullet}{3}, \quad (3.35)$$

$$a^\bullet = \hat{a} - \frac{\hat{b}^2}{\hat{a}}, \quad (3.36)$$

$$b^\bullet = \hat{b} - \frac{\hat{b}^2}{\hat{a}}. \quad (3.37)$$

Four cases can be distinguished with respect to the local boundary conditions:

1. **“Constrained quench” with fluid core** - All strain components are zero, except for ε_{33} , which must obey:

$$\int_{-\frac{\hat{h}}{2}}^{\frac{\hat{h}}{2}} \varepsilon_{33} d\chi = 0. \quad (3.38)$$

The corresponding Cauchy stress component equals $-p$, which is governed by equation (2.65).

2. **“Constrained quench” with solid core** - The only difference with case 1 is that instead of $\sigma_{33} = -p$, equation (3.39) is used, which can be derived from equation (3.33) and equation (3.38) and the fact that σ_{33} is constant across the thickness:

$$\sigma_{33} = \frac{\int_{-h/2}^{h/2} \sigma_{33}^* / \hat{a} \, d\chi}{\int_{-h/2}^{h/2} 1 / \hat{a} \, d\chi} \quad (3.39)$$

3. **“Free quench” inside the mould** - All strain components still equal zero, except ϵ_{33} . In this case $\sigma_{33} = -p_{atm}$ (the atmospheric pressure) is used.
4. **“Free quench” outside the mould** - All strain components may be non-zero. They are derived from the change in the displacement field $\Delta \vec{u}_i$ during time step Δt_i , which is approximated by solving equation (2.2), after substitution of equation (3.28), using a finite element method (see section 3.4)

All stress components, other than σ_{33} , are determined using equations (3.28) to (3.37).

Flow induced stress

At each time step, equations (2.79) to (2.84) are solved for all material particles in the fluid state, and the deviatoric part of the stress tensor is updated using equation (2.21). When a particle solidifies during a time step Δt_i , the stress at t_{i-1} is frozen in permanently. Equation (3.8) can be applied to approximate the material derivatives of B_{kl} , but the convective term proved to be negligible. Due to numerical inaccuracies, $\det(B_{kl})$ may deviate from 1 after some time steps. Therefore, B_{33} is recomputed from the other components every time step.

Elastic recovery

Division of the time integral in equation (2.88) into a part before t_{i-1} and a part from t_{i-1} to t_i yields:

$$\epsilon_c^d(t_i) = \sigma^d \left[J_g + t_i / \eta_K + \sum_{j=1}^{m_K} J_j \left(1 - \prod_{k=1}^i \zeta_{Kj}(t_k, t_{k-1}) \right) \right] \quad (3.40)$$

Application of the trapezium rule for numerical integration to the expression for ζ_{Kj} results in:

$$\zeta_{Kj}(t_k, t_{k-1}) = \exp \left(-\frac{\Delta t_k}{\tau_{Kj}} \Big|_{t=t_k} + \frac{\Delta t_k}{\tau_{Kj}} \Big|_{t=t_{k-1}} \right) \quad (3.41)$$

3.3 Iteration methods

Every time step, the pressure and temperature fields are initially estimated from the previous time step. For the first time step, they are based on boundary and initial conditions. During filling the values at new nodes are extrapolated from the nodes at the previous flow front. The pressure gradient and shear rate are not computed from the estimated pressure and temperature fields but are estimated just like these fields: although discontinuities in cavity thickness may introduce some serious errors in these estimations, convergence is generally better applying this method. From these estimations, the coefficients of the pressure and the temperature equations (3.10) to (3.13) can be derived. An approximate solution is computed using finite element methods (see section 3.4), enabling recalculation of the coefficients and solution of the equations (Picard iteration scheme). Convergence is checked, using the deviation between two subsequent iterations, with respect to computed pressure, temperature and velocity. The first iteration, \vec{v}^* is taken the null vector in equations (3.11) and (3.13). This improved the stability of the Picard iteration method. A poor estimate of the velocity field appeared to lead to even worse convected pressure and temperature fields.

As mentioned in section 3.2 a separate Picard iteration scheme is employed for the computation of δ_{j_i} (equation (3.17)).

3.4 Spatial discretisation and FE formulation

The equations for pressure ((3.10), temperature ((3.12), the convection equations ((3.11), (3.13) and the equations for warpage ((2.2), (3.28)) are solved employing finite element methods to compute approximate solutions.

Pressure equation

As the pressure is assumed constant across the thickness of the product, a mesh is defined on the midplanes of the (filled part of the) cavity. Biquadratic nine-noded quadrilateral surface elements are applied to describe

the pressure field for the midplanes. Although quadrilaterals limit the flexibility during meshing, this element type was chosen because of its good convergence when refining the mesh, yielding an accurate approximation of the pressure gradient (see appendix A). The accuracy of this gradient is important, as it determines the accuracy of the velocity field (equation (2.60)) and also of the material derivatives (equation (3.11)). At junctions and sharp corners of the midplanes, the pressure gradient is defined for every plane separately. Thus the velocity is always parallel to the midplane, which is again important for computation of the material derivatives via equation (3.11).

Equation (3.10) is a second order elliptic differential equation for the pressure. The solution is approximated using the Galerkin finite element method, as implemented in the finite element package SEPRAN (see Segal, 1993). The coefficients are determined in the vertices of the elements only, and interpolated to the midpoints. As the region Ω_c for which equations (3.10) is defined, change in time, local remeshing is required every time step. In appendix B this technique is described.

Temperature equation

In every vertex of the quadratic pressure elements a gridline is defined in thickness direction. In the case that the boundary conditions at Γ^+ and Γ^- are equal (symmetrical case), only half the thickness is discretised by the grid line. In this case the gridline is split into two parts: one for the solidified layer, and one for the fluid layer. In the asymmetrical case, a third part is reserved for the second solidified layer. The number of grid points in each part is equal for every grid line and independent of the thickness of the solidified layer. Figure 3.1 illustrates this. When the material is completely solidified, the grid points are spread evenly over the grid line. Linear line elements are used to describe the temperature across the thickness. Equation (3.12) is a second order elliptical differential equation. An approximate solution for this equation is computed using the Galerkin finite element method.

Convection equation

Given the velocity in all grid points, for each grid plane in the fluid layer the convection equation is solved (see figure 3.1). The solution field is approximated by bilinear elements. A SUPG finite element method is employed, using the time dependent upwind parameter according to (Zoetelief, 1995, app. B). After the convection equation is solved, the typical fountain flow

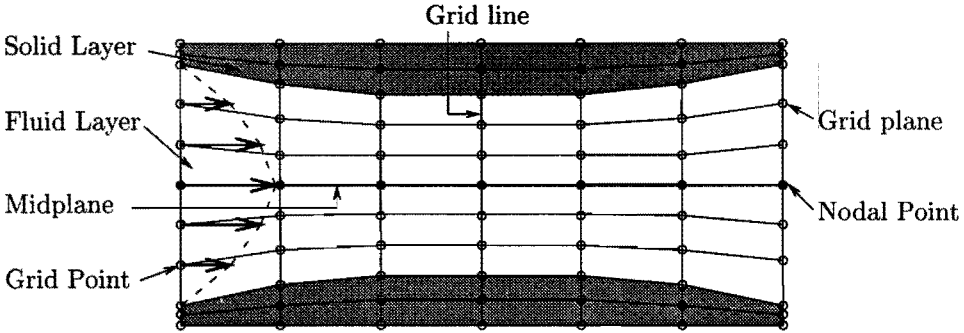


Figure 3.1: Definition of grid lines in thickness direction (asymmetrical case)

at the flow front is incorporated. For all grid lines at the flow front, data at grid points where $\bar{v}^* < \bar{v}^*$ are overwritten by interpolated data of the corresponding positions where $\bar{v}^* > \bar{v}^*$ (see also end of section 2.3 and figure 2.2b).

Shrinkage and warpage

The geometry is discretised by bilinear shell elements, of which the vertices coincide with the (biquadratic) pressure elements (see also Hughes and Liu (1981), Dvorkin and Bathe (1984) and Douven (1991)). Isoparametric coordinates $\zeta_1, \zeta_2, \zeta_3 \in [-1, 1]$ are introduced. Coordinate ζ_3 coincides with the local thickness or fibre direction of the shell (see figure 3.2). The mapping to the physical shell domain is described by:

$$\bar{x} = \sum_{a=1}^4 (N_a \bar{x}_a^l + N_a z_a \bar{x}_a^f) \tag{3.42}$$

where \bar{x} is the position vector of an arbitrary point in the physical shell domain, \bar{x}_a^l is the position vector at the reference plane (i.e. $\zeta_3 = 0$) for element node a and \bar{x}_a^f is the unit vector representing the fibre direction at node a . The interpolation functions N_a and z_a are defined as:

$$N_a = \frac{1}{4} (1 + \zeta_{1a} \zeta_1) (1 + \zeta_{2a} \zeta_2), \tag{3.43}$$

$$z_a = \frac{h_a}{2} \zeta_3, \tag{3.44}$$

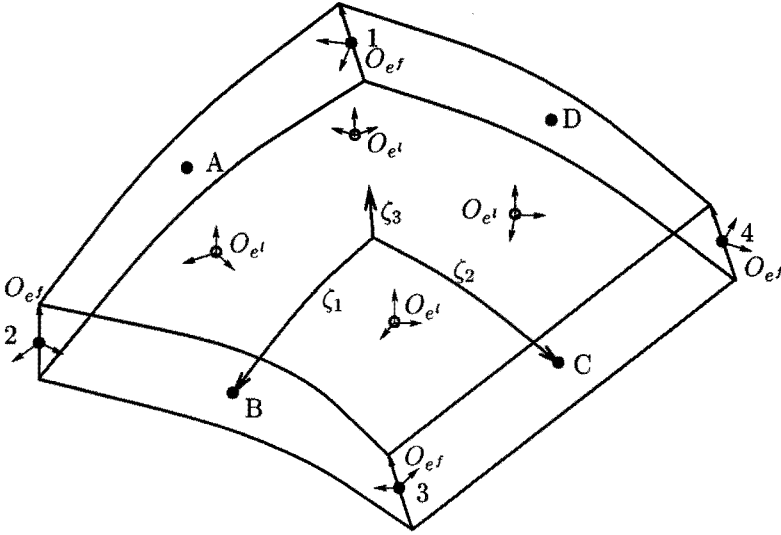


Figure 3.2: Definition of isoparametric coordinates and the numbering of vertices and midside nodes

with h_a the thickness in fibre direction at node a and ζ_{1a}, ζ_{2a} the isoparametric coordinates of node a . The displacement field \vec{u} and also the incremental displacements $\Delta\vec{u}$ are interpolated similar to \vec{x} . The nodal fibres are assumed to be inextensible.

A lamina is a surface for which ζ_3 is constant. Integration over a lamina is done by four point Gaussian quadrature. In every integration point a Cartesian vector base O_{e^l} is defined with \vec{e}_1^l, \vec{e}_2^l tangent to the lamina (see figure 3.2). In every nodal point a local Cartesian vector base O_{e^f} is defined with \vec{e}_3^f in fibre direction (indicated in the same figure), which will be used as a reference frame for rotation increments about \vec{e}_1^f, \vec{e}_2^f ($\Delta\phi_2, \Delta\phi_1$ respectively). These rotation increments are related to the incremental fibre displacement $\Delta\vec{u}^f$ according to the linearised equation:

$$\begin{bmatrix} \Delta\vec{u}^f \cdot \vec{e}_1^f \\ \Delta\vec{u}^f \cdot \vec{e}_2^f \\ \Delta\vec{u}^f \cdot \vec{e}_3^f \end{bmatrix} = \begin{bmatrix} -1 & 0 \\ 0 & -1 \\ 0 & 0 \end{bmatrix} \begin{bmatrix} \Delta\phi_1 \\ \Delta\phi_2 \end{bmatrix} = \mathbf{R}^{\phi f} \Delta\phi, \quad (3.45)$$

(see figure 3.3 for sign conventions). Thus the third rotation is eliminated as a degree of freedom. The (incremental) nodal displacements are defined with

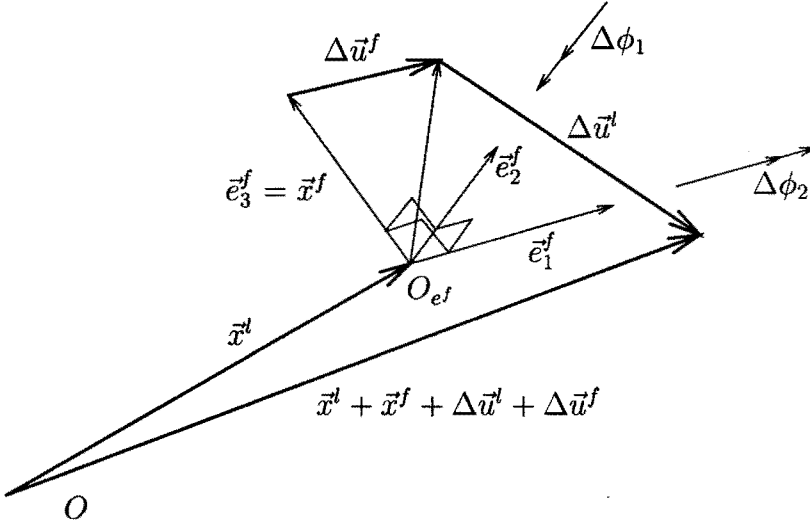


Figure 3.3: Definition of kinematics and sign conventions at a nodal point

respect to the global base O_e . Three rotation tensors $\mathbf{R}^{gl} = \bar{e}_n^l \bar{e}_n$ (global to lamina), $\mathbf{R}^{fg} = \bar{e}_n \bar{e}_n^f$ (fibre to global), $\mathbf{R}^{fl} = \bar{e}_n^l \bar{e}_n^f$ (fibre to lamina) are defined to transform vectors from one base to another.

A strain displacement relation is required to solve the momentum equation in terms of incremental displacements with respect to global base \bar{e}_n :

$$\Delta \varepsilon = \underline{B} \Delta U = \sum_{a=1}^4 B_a \Delta U_a = \sum_{a=1}^4 B_a \left[\Delta u_a^l \quad \Delta u_a^f \right]^T \quad (3.46)$$

The matrix \underline{B} is derived as follows. The incremental strain components with respect to the covariant reference frame O_g , with $\bar{g}_n = \frac{\partial \bar{x}}{\partial \zeta_n}$, are approximated by the linearised form:

$$\Delta \hat{\varepsilon}_{mn} = \frac{1}{2} \left(\frac{\partial \Delta \bar{u}}{\partial \zeta_m} \cdot \bar{g}_n + \frac{\partial \Delta \bar{u}}{\partial \zeta_n} \cdot \bar{g}_m \right) \quad (m, n = 1, 2, 3) \quad (3.47)$$

Using equation (3.42) for $\Delta \bar{u}$, this can be written as:

$$\Delta \hat{\varepsilon}_{mn} = \frac{1}{2} \sum_{a=1}^4 (N_{a,m} \Delta \bar{u}_a^l \cdot \bar{g}_n + z_a N_{a,m} \Delta \bar{u}_a^f \cdot \bar{g}_n + N_{a,n} \Delta \bar{u}_a^l \cdot \bar{g}_m + z_a N_{a,n} \Delta \bar{u}_a^f \cdot \bar{g}_m) \quad (3.48)$$

$$= \sum_{a=1}^4 \hat{b}_a^{mnT} \Delta U_a \quad (3.49)$$

$(m, n = 1, 2, 3)$

where $(\cdot)_{,n} = \frac{\partial}{\partial \zeta_n}$. To prevent locking of the element in the case of thin shells, Dvorkin and Bathe (1984) proposed the following interpolation of the transverse incremental strains $\Delta \hat{\varepsilon}_{13}$, $\Delta \hat{\varepsilon}_{23}$:

$$\Delta \hat{\varepsilon}_{13} = \frac{1}{2}(1 - \zeta_2)\Delta \hat{\varepsilon}_{13}^A + \frac{1}{2}(1 + \zeta_2)\Delta \hat{\varepsilon}_{13}^C \quad (3.50)$$

$$\Delta \hat{\varepsilon}_{23} = \frac{1}{2}(1 - \zeta_1)\Delta \hat{\varepsilon}_{23}^D + \frac{1}{2}(1 + \zeta_1)\Delta \hat{\varepsilon}_{23}^B \quad (3.51)$$

where e.g. $\Delta \hat{\varepsilon}_{13}^A$ is evaluated according to equation (3.48) in point A (see figure 3.2). A transformation matrix $R_{mn}^{cl} = \vec{e}_m^l \cdot \vec{g}_n$ is used to transform the strains $\Delta \hat{\varepsilon}_{mn}$ from the covariant base O_g to the lamina base O_{e^l} :

$$\hat{b}_a^{mnT} = R_{km}^{cl} \hat{b}_a^{klT} R_{ln}^{cl} \quad (3.52)$$

This results in the following expression for B :

$$B = \begin{bmatrix} b_1 & 0 & 0 & b_4 & 0 & 0 \\ 0 & b_2 & 0 & 0 & b_5 & 0 \\ b_2 & b_1 & 0 & b_5 & b_4 & 0 \\ b_1^{23} & b_2^{23} & b_3^{23} & b_4^{23} & b_5^{23} & b_6^{23} \\ b_1^{13} & b_2^{13} & b_3^{13} & b_4^{13} & b_5^{13} & b_6^{13} \end{bmatrix} \quad (3.53)$$

with

$$b_i = \begin{cases} N_{a,n} & n = 1, 2, 3, \\ (N_a z_a)_{,(n-3)} & n = 4, 5, 6. \end{cases} \quad (3.54)$$

Following Hughes and Liu (1981), the shear correction factor $\kappa_{sh}^{1/2}$, with $\kappa_{sh} = 5/6$, is used for b_1^{13} to b_6^{13} and b_1^{23} to b_6^{23} .

The partial element matrices k_{ab}^e , the left hand side columns Δd_a^e and the right hand sides Δr_a^e ($a, b = 1, 2, 3, 4$, no summation) can now be written as:

$$k_{ab}^e = \int_{-1}^1 \int_{-1}^1 Q_a^T \int_{-1}^1 B_a^T M B_b J d\zeta_3 Q_b d\zeta_1 d\zeta_2 \quad (3.55)$$

$$\Delta d_a^e = [\Delta \vec{u}_a^t \cdot \vec{e}_1 \quad \Delta \vec{u}_a^t \cdot \vec{e}_1 \quad \Delta \vec{u}_a^t \cdot \vec{e}_1 \quad \Delta \phi_{1a} \quad \Delta \phi_{2a}]^T \quad (3.56)$$

$$\Delta r_a^e = - \int_{-1}^1 \int_{-1}^1 Q_a^T \int_{-1}^1 B_a^T g J d\zeta_3 d\zeta_1 d\zeta_2 \quad (3.57)$$

with

$$J = \det \left(\frac{\partial \underline{x}}{\partial \underline{\zeta}} \right), \quad \underline{x} = [\underline{x} \cdot \vec{e}_1 \quad \underline{x} \cdot \vec{e}_2 \quad \underline{x} \cdot \vec{e}_3]^T \quad (3.58)$$

$$\underline{Q}_a = \begin{bmatrix} R^{gl} & 0_{32} \\ 0_{33} & R^{fl} R^{\phi f} \end{bmatrix}. \quad (3.59)$$

In the case of stiffeners or ribs being present in the geometry, the sixth degree of freedom is not eliminated in the nodes located at the junctions. For these nodes $\Delta \underline{d}_a^e$, \underline{Q}_a become:

$$\Delta \underline{d}_a^e = [\Delta \vec{u}_a^l \cdot \vec{e}_1 \quad \Delta \vec{u}_a^l \cdot \vec{e}_2 \quad \Delta \vec{u}_a^l \cdot \vec{e}_3 \quad \Delta \vec{u}_a^f \cdot \vec{e}_1 \quad \Delta \vec{u}_a^f \cdot \vec{e}_2 \quad \Delta \vec{u}_a^f \cdot \vec{e}_3]^T, \quad (3.60)$$

$$\underline{Q}_a = \begin{bmatrix} R^{gl} & 0_{33} \\ 0_{33} & R^{gl} \end{bmatrix}. \quad (3.61)$$

This choice is made on a node-by-node basis.

Elastic recovery

The model chosen for elastic recovery is such that cases where cooling is asymmetrical, or cases with kinematic boundary conditions restricting the recovery processes cannot be studied. A different approach would be the addition of the computed flow-induced residual stress tensor to the initial stress tensor $\sigma_{j_{i-1}}^d$ in equation (3.27) every time step. However, the geometry and conditions of the cases studied in this work are such, that equation (3.40) of the original approach can be solved on a node-by-node basis, saving considerable computing time.

3.5 Discussion

For the resulting set of equations of Chapter 2, numerical solution procedures were developed and tested for convergence and stability. The numerical methods were, if not already available, implemented in the SEPRAN finite element package (see Segal, 1993) by Caspers *et al.* (1994b).

Chapter 4

Material Characterisation

Two materials are used in this study. One is a polymethylmethacrylate (PMMA), Plexiglas 7H from Röhm, and the other is a polystyrene (PS), Styron 678E from Dow Chemical. Their rheological and thermal properties are discussed in this chapter.

4.1 Rheology

PMMA 7H In order to compute the flow kinematics during filling, the shear viscosity must be known as a function of shear rate, temperature and pressure. Experimental data were obtained from Schennink (1991), who performed small-amplitude oscillatory shear experiments (Rheometrics Dynamic Spectrometer RDS-II) for several temperatures and frequencies. An oscillatory shear strain was imposed on the sample, while measuring the resulting torque and the phase difference between the strain and the torque. The result is plotted in figure 4.1, where ω denotes the angular frequency and η^* the dynamic viscosity. Applying the Cox-Merz rule, ω can be read as the shear rate $\dot{\gamma}$ and η^* as the steady state shear viscosity η .

A fit using the 7-constant Cross model (equation (2.52)) is shown in figure 4.1 as well, of which the parameters are listed in table 4.1. The fit deviates from the experimental values for low temperatures and high frequencies, as the model does not incorporate the second plateau found experimentally. The pressure dependence of the viscosity, not available from the experimental data, is taken equal to the T_g pressure dependence (see s_0 in table 4.1).

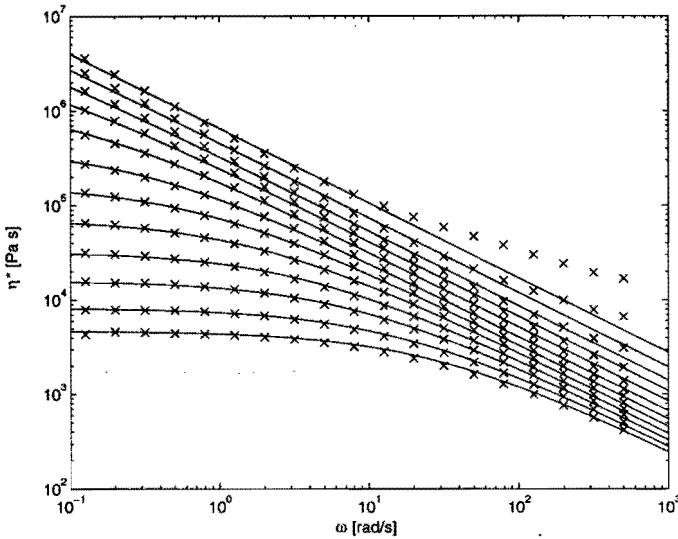


Figure 4.1: Experimental (x) and fitted (lines) viscosity of PMMA at (from top to bottom) 402.6, 412.8, 422.9, 433.2, 442.5, 452.8, 463.7, 473.7, 483.5, 493.6, 503.6, 513.8 and 523.0 K (Schennink (1991))

PMMA 7H		
η_{C0}	$10^3 Pa s$	75.0
T_{Cr}	K	483
n	-	0.21
τ_{C0}	$10^4 s$	12
c_{C1}	-	17.6
c_{C2}	K	215
s_0	$10^{-7} K/Pa$	3.0

Table 4.1: Parameters of 7-constant Cross model, eq. (2.52)

PS 678E The rheological behaviour for the computation of the flow kinematics is described by the steady state Leonov model (see equation (2.48)), and the compressible Leonov model (equations (2.21) to (2.25)) is used for the computation of flow induced stresses, applying the decoupled approach. The parameters as determined by Douven (1991) are listed in table 4.2. The corresponding fit on the oscillatory shear experiments, shifted to the reference temperature $T_{Lr} = 462K$, is shown in the lower plots of figure 4.2.

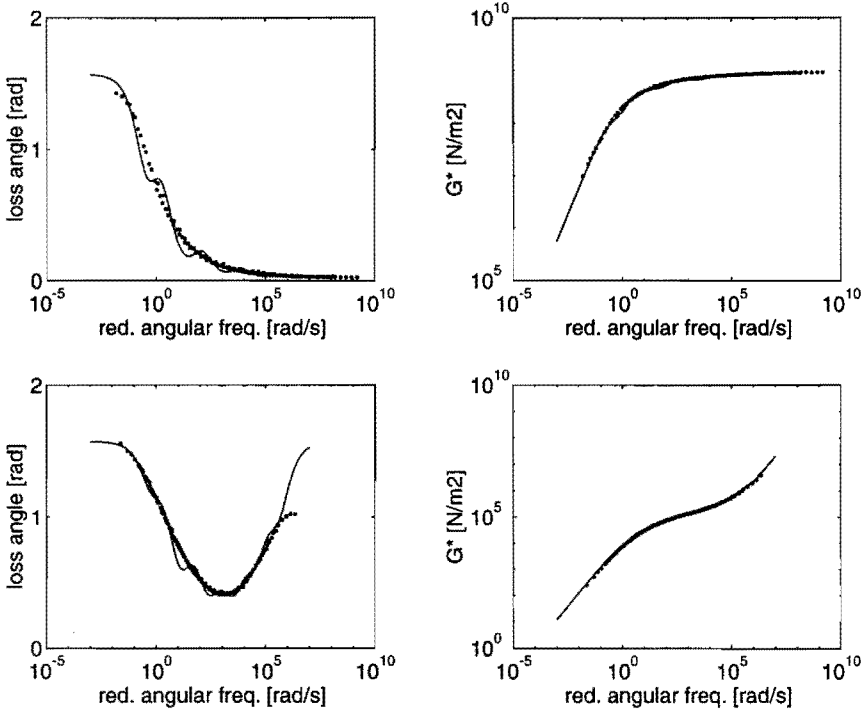


Figure 4.2: Experimental (dots) and fitted (lines) loss angle and dynamic modulus for PS 678E; top: Maxwell model, $T_{Mr} = 363K$; bottom: Leonov model, $T_{Lr} = 462K$ (Douven (1991))

The parameters for the multi-mode Maxwell model, describing the viscoelastic behaviour for the thermal stress analysis (see equation (2.34)), are also taken from Douven and are listed in table 4.3. The corresponding fit on the master curve of the oscillatory torsion experiments (reference temperature $T_{Mr} = 363K$) is shown in the upper plots of figure 4.2. The parameters for the Voigt model (equation (2.39)), listed in table 4.4, are derived from the same experiments that resulted into the Maxwell parameters. From the measured dynamic modulus and loss angle the shear storage modulus G' and the loss modulus G'' are computed. From these quantities the storage compliance J' and loss compliance J'' can be derived (see Ferry, 1980). The value of the instantaneous compliance J_g is chosen 10^{-9} . Although the material is not crosslinked, the shear viscosity η_K is taken infinite in order to make the behaviour at low frequencies somewhat more realistic. Note that the viscous

PS 678E			$\eta_{r0} = 2.05 \text{ Pa s}$	
j	τ_{Lj0}	s	η_{Lj0}	Pa s
1	2.250		$6.011 \cdot 10^3$	
2	$1.965 \cdot 10^{-1}$		$5.639 \cdot 10^3$	
3	$1.175 \cdot 10^{-2}$		$7.402 \cdot 10^2$	
4	$7.872 \cdot 10^{-4}$		$6.499 \cdot 10^1$	
5	$5.472 \cdot 10^{-5}$		8.616	
6	$4.140 \cdot 10^{-6}$		2.335	

Table 4.2: Linear viscoelastic parameters used in the Leonov model, eqs. (2.21) to (2.25)

PS 678E				
j	τ_{Mj0}	s	G_{Mj}	Pa
1	$4.769 \cdot 10^{-8}$		$6.919 \cdot 10^7$	
2	$2.498 \cdot 10^{-6}$		$5.958 \cdot 10^7$	
3	$1.178 \cdot 10^{-4}$		$1.203 \cdot 10^8$	
4	$6.660 \cdot 10^{-3}$		$2.220 \cdot 10^8$	
5	$3.000 \cdot 10^{-1}$		$3.433 \cdot 10^8$	
6	4.996		$9.136 \cdot 10^7$	

Table 4.3: Linear viscoelastic parameters used in the Maxwell model, eq. (2.34)

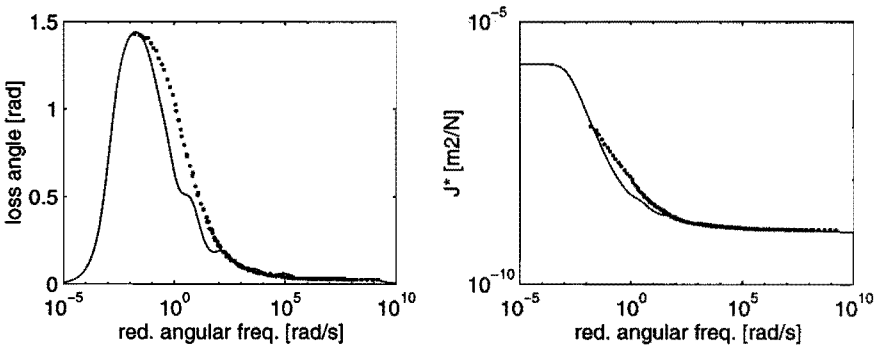


Figure 4.3: Experimental (dots) and fitted (lines) loss angle and dynamic compliance for PS 678E; $T_{Kr} = 363K$

PS 678E		
$J_g = 10^{-9} Pa^{-1}$		$\eta_K = \infty Pa s$
j	$\tau_{Kj0} s$	$J_j Pa^{-1}$
1	$1.351 \cdot 10^{-9}$	$5.429 \cdot 10^{-11}$
2	$2.519 \cdot 10^{-8}$	$6.008 \cdot 10^{-11}$
3	$4.976 \cdot 10^{-7}$	$7.337 \cdot 10^{-11}$
4	$1.174 \cdot 10^{-5}$	$1.281 \cdot 10^{-10}$
5	$2.694 \cdot 10^{-4}$	$1.951 \cdot 10^{-10}$
6	$6.928 \cdot 10^{-3}$	$5.355 \cdot 10^{-10}$
7	$2.645 \cdot 10^{-1}$	$2.049 \cdot 10^{-9}$
8	$3.858 \cdot 10^0$	$2.728 \cdot 10^{-9}$
9	$8.338 \cdot 10^2$	$1.576 \cdot 10^{-6}$

Table 4.4: Linear viscoelastic parameters used in the Voigt model, eq. (2.39)

PS 678E								
Leonov			Maxwell			Voigt		
c_{L1}	-	10.45	c_{M1}	-	30.60			
c_{L2}	K	150.36	c_{M2}	K	51.36			
			c_{M3}	K^{-1}	0.6242	c_{K3}	K^{-1}	0.6242
T_{Lr}	K	462	T_{Mr}	K	363	T_{Kr}	K	363

Table 4.5: Parameters for the time-temperature shift functions

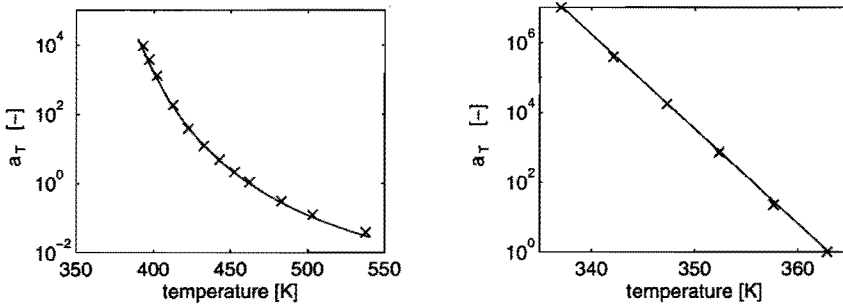


Figure 4.4: Experimental (x) and fitted (lines) horizontal shift factor for PS 678E; left: fluid behaviour, $T_r = 462K$; right: solid behaviour, $T_r = 363K$ (from Douven (1991))

behaviour is described by the high compliance and relatively long relaxation time of the ninth mode. Figure 4.3 shows the corresponding fit at $T_{Kr} = 363K$. The shift factors for the three models are listed in table 4.5. The WLF fit (equations (2.28) and (2.37)) for the fluid behaviour and the Arrhenius fit (equation (2.38)) for the solid behaviour are shown in figure 4.4.

4.2 Specific volume

The parameters of the Tait model (equation (2.6)) can be determined by a least-squares fit on pvT data, i.e. measurements of specific volume for several pressures and temperatures. The rates at which pressure and temperature are varied during these measurements is chosen low to ensure that an equilibrium state is reached. The parameters of the KAHR model (2.9) are fitted on the results of a number of measurements of the length or volume of a sample during and after certain well defined pressure and temperature histories.

PMMA 7H Tait model parameters - The pvT behaviour was measured by Nies (1991) with an apparatus similar to the one described by Zoller *et al.* (1976). Density changes were measured as a result of changes in temperature and pressure. The sample is cooled at a low rate and under a low pressure to the minimum temperature. Then the pressure is applied in several steps, while the volume change is measured for each step. Subsequently the pressure is removed, the temperature is increased to the next level and a new pressure cycle is started. Results of these measurements are shown in figure 4.5, together with the fitted pvT behaviour according to the Tait model (2.6), of which the parameters are shown in table 4.6. The deviating data points in the high temperature range were left out from the fitting procedure. Not only was the apparatus not calibrated for high temperatures, but also material degradation is likely to occur there.

KAHR model parameters - Parameters $\Delta\alpha$ and $\Delta\kappa$ (equation (2.10)), of which the latter is chosen pressure dependent according to

$$\Delta\kappa = \Delta\kappa_0 - \kappa_1 p. \quad (4.1)$$

can be determined from the pvT measurements shown in the previous paragraph (see table 4.7). They are not determined from the raw data, but derived from the Tait fit. A thermomechanical analyser (TMA, see appendix D)

PMMA 7H		pvT		TMA	
		melt	glass	melt	glass
a_0	$10^{-4} m^3/kg$	8.643	8.643	8.824	8.824
a_1	$10^{-7} m^3/(kgK)$	5.85	1.53	5.85	2.89
B_0	$10^8 Pa$	2.6	3.0	2.6	4.3
B_1	$10^{-3} \text{ }^\circ C^{-1}$	3.9	-1.3	3.9	5.5
T_{g0}	K	355		384	
s_0	$10^{-7} K/Pa$	3.0		3.0	

Table 4.6: Tait model parameters, eq. (2.6), from pvT experiments and from TMA experiments via the KAHR model (see text)

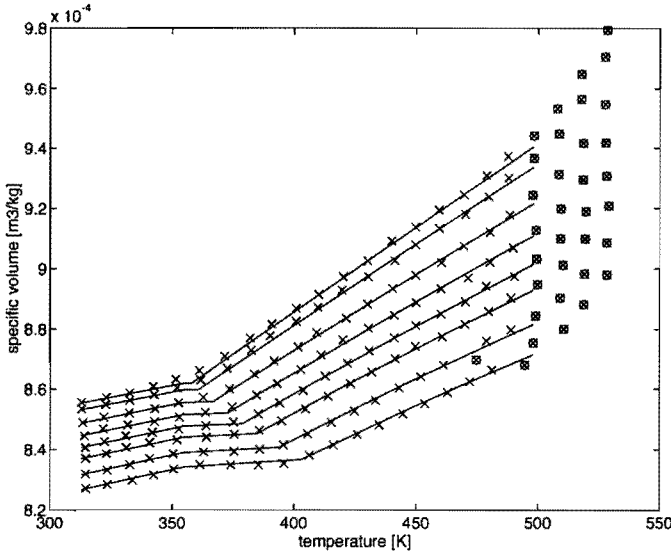


Figure 4.5: Experimental (x) and fitted (lines) pvT behaviour of PMMA. The experiments with an extra circle are left out from the fit.

was used to verify the value of $\Delta\alpha$. The temperature was prescribed to cycle twice between 418 K and 318 K at a rate of 1/60 K/s. The result of this experiment is plotted in figure 4.6. Within the glass transition range some hysteresis may be expected, due to ageing effects. The hysteresis shown in figure 4.6 is, however, due to the fact that during cooling the sample temperature is slightly above the temperature measured by the thermocouple. During heating the opposite is true, which results in a horizontal shift of 2.5

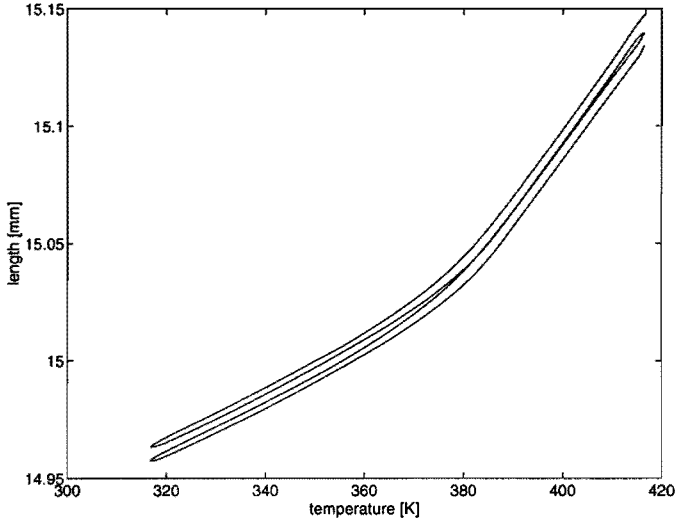


Figure 4.6: Length of PMMA sample as a function of temperature.

K between the cooling and heating curves. There is also a vertical shift of the curves between the first and the second heating and cooling cycle, which is due to creep (0.0064 mm). It was found that creep is significant only above 400 K . The expansion coefficients are hardly different during cooling and heating for both cycles. From figure 4.6 the expansion coefficients are found as listed in table 4.7. There is a significant deviation between the

PMMA 7H		pvT	TMA
α_m	10^{-4} K^{-1}	6.8	5.9
α_s	10^{-4} K^{-1}	1.8	2.1
$\Delta\alpha$	10^{-4} K^{-1}	5.0	3.8
$\Delta\kappa_0$	10^{-10} Pa^{-1}	2.0	
κ_1	10^{-19} Pa^{-2}	4.5	

Table 4.7: Thermal expansion coefficients and isothermal compressibility coefficients of PMMA 7H from both pvT and TMA experiments

coefficients obtained from the pvT and the TMA measurements. One reason is that maximum temperature during the TMA experiments was 418 K to prevent creep effects, while 489 K was reached during the pvT measurements. If only data up to 418 K are incorporated in the fitting procedure

of the Tait equation on the pvT data, $\alpha_m = 6.37 \cdot 10^{-4} K^{-1}$ is found, a value which is much closer to the value obtained from the TMA measurements. This is caused by a slight increase of $\frac{\partial v}{\partial T}$ with temperature above T_g . The difference in α_s may be due to viscoelasticity of the bulk modulus and the relatively poor fit of the Tait equation. The results from the TMA compare best with literature data for different PMMA's (see Greiner and Schwarzl (1984): $\alpha_m = 5.76 \cdot 10^{-4} K^{-1}$, $\alpha_s = 2.4 \cdot 10^{-4} K^{-1}$, $\Delta\alpha = 3.32 \cdot 10^{-4} K^{-1}$; McKinney and Simha (1977): $2.35 \cdot 10^{-4} K^{-1} \leq \Delta\alpha \leq 3.1 \cdot 10^{-4} K^{-1}$; VDMA (1979): $\alpha_m = 5.86 \cdot 10^{-4} K^{-1}$, $\alpha_s = 1.78 \cdot 10^{-4} K^{-1}$, $\Delta\alpha = 3.08 \cdot 10^{-4} K^{-1}$). The glass transition temperature is also different for the pvT (355 K) and the TMA data (375 K). This is most likely caused by the poor fit for the solid behaviour of the Tait equation.

Two types of experiments were performed to fit the KAHR parameters $\tau_{\delta 0}$, β , θ and x in equation (2.13) and (2.15). A contraction experiment starts at a temperature above T_g . Subsequently the sample is cooled down (at $1/60 K/s$) to a temperature below T_g . Then the temperature is kept constant and the sample length is measured as a function of time. A memory experiment starts with a contraction experiment, followed by an increase in temperature (at $1/60 K/s$) to a temperature still below T_g . Again the sample length is measured as a function of time. Note that the expansion experiment, as proposed by Greener *et al.* (1991), is omitted here. Given the accuracy of the TMA, the experiments would take too long, as the starting temperature must be chosen significantly below T_g and the sample length must be at its equilibrium value. Besides, expansion during injection moulding is unlikely to take place. The parameter b in equation (2.14) is computed from the pressure dependence of T_g , taken from the Tait fit. Figure 4.7 shows a typical result of a contraction experiment. The sample length is converted into the KAHR parameter δ by fitting the straight part of the curve above T_g . This straight line is shifted horizontally to cross the curve at its starting point to correct for the temperature induced hysteresis effect mentioned earlier. The line represents the length l_∞ as a function of temperature, and is used in the following (approximate) equation for δ , which can be derived from equation (2.9):

$$\delta = \frac{3(l - l_\infty)}{l_\infty} \quad (4.2)$$

This is done for every experiment separately. The results are used to fit the KAHR parameters $\tau_{\delta 0}$, β , θ and x in equation (2.13), (2.15), employing a

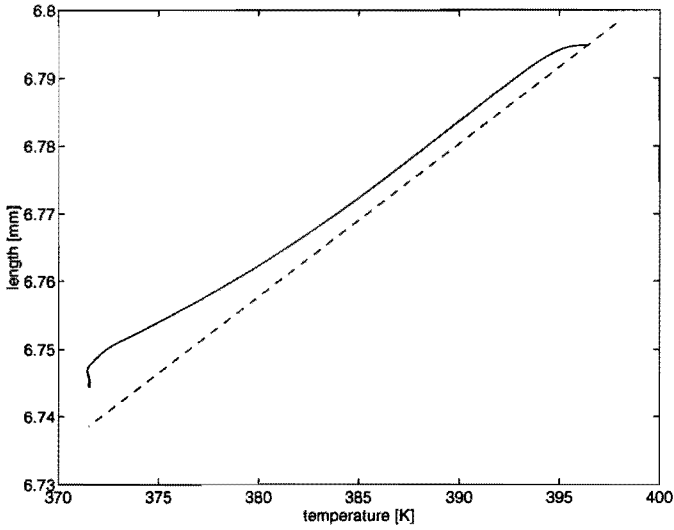


Figure 4.7: Typical result from contraction experiment (full line) and the corresponding equilibrium length (dashed line)

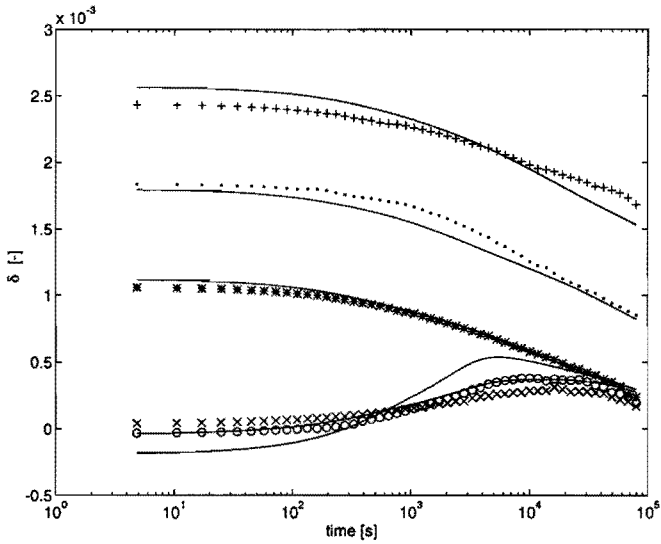


Figure 4.8: Experimental results (symbols) and fit (full lines) for the contraction and memory experiments

Levenberg-Marquardt method (see MATLAB, 1992). Figure 4.8 shows the results for the contraction and memory experiments in terms of δ , together with the fit by the KAHR model. The KAHR parameters found are listed in table 4.8. The fit of the contraction experiments is relatively good. The memory experiments are fitted somewhat worse. This may influence the predictive quality of the model concerning volume relaxation at elevated temperatures after physical ageing at lower temperatures.

Having all parameters of the KAHR model, the double domain Tait model can be fitted on predictions of the first model, using isobars that result from cooling at 25 K/s at several pressure levels. The corresponding parameters are listed in table 4.6 under TMA.

PMMA 7H		
$\tau_{\delta 0}$	10^{-2} s	0.260
β	-	0.272
θ	K^{-1}	0.903
b	10^{-6} Pa^{-1}	0.272
x	-	0.144

Table 4.8: KAHR model parameters, eqs. (2.12) to (2.15)

PS 678E Tait model parameters - The pvt behaviour was measured and fitted by Flaman (1990). The corresponding Tait parameters are summarised in table 4.9. The KAHR parameters were not determined for PS 678E.

4.3 Thermal capacity and heat conduction

PMMA 7H Both the heat capacity and heat conduction data are taken from the literature (VDMA (1979)), although these data were measured for a different type of PMMA. The heat capacity is assumed to be pressure independent and is fitted to equation (2.46). The parameters for PMMA 7H are listed in table 4.10. An average value of 0.19 W/Km is taken for λ .

PS 678E Equation (2.46) is used to describe c_p for PS as well. The parameters, taken from Douven (1991), are listed in table 4.10. The thermal

conductivity λ of PS 678E is taken the constant value of $0.17 \text{ W/m}^2\text{K}$ (see Flaman, 1990).

PS 678E		melt	glass
a_0	$10^{-4} \text{ m}^3/\text{kg}$	9.758	9.758
a_1	$10^{-7} \text{ m}^3/(\text{kgK})$	5.8	2.3
B_0	10^8 Pa	2.4	3.5
B_1	$10^{-3} \text{ }^\circ\text{C}^{-1}$	3.6	3.0
T_{g0}	K	373	
s_0	10^{-7} K/Pa	5.1	

Table 4.9: Tait model parameters, eq. (2.6)

		PMMA 7H	PS 678E
c_{p1}	$J/(\text{kgK})$	1780	1730
c_{p2}	$J/(\text{kgK}^2)$	3.8	2.1
c_{p3}	$J/(\text{kgK})$	170	172
c_{p4}	K^{-1}	0.075	0.155
c_{p5}	K	371	359

Table 4.10: Parameters for c_p , eq. (2.46)

4.4 Discussion

In this chapter, the rheological and thermal properties, required as input for the simulation of injection moulding, can be described by a set of models, of which the parameters were fitted on experimental data. The quality of the fits on rheological data is sufficient, except for the lack of experimental data for the viscosity at higher pressures. The incompatibility of the $p\nu T$ and the TMA experiments shows that the characterisation of the specific volume is not straightforward. Finally, there is no data available on the influence of orientation on the heat conduction coefficient.

Chapter 5

Characteristic results

In this chapter several cases are presented, that are characteristic for the applicability and accuracy of the models developed. Numerical results are compared with experimental results if available. In the first section, 5.1, this comparison is made for the computed density distribution (cases A to E). Also the influence of (accelerated) physical ageing on the density distribution is studied (case F). The results for the residual stress distribution are presented in sections 5.2 (cases G to J, thermal stresses) and 5.3 (case K, flow-induced stresses). The model for thermal stress was already validated by Zoetelief *et al.* (1995) for standard injection moulding of a relatively simple strip. Here, the two-shot moulding process is chosen as an example to illustrate the build-up of thermally induced residual stresses. The flow-induced residual stress is computed for a case studied earlier by Flaman (1990) and Douven (1991). Finally, in section 5.4 the model for elastic recovery is applied for a case (L), which was also studied by Schennink (1993).

5.1 Density distribution

Geometry, processing conditions and material parameters

The density distributions of injection moulded PMMA strips were measured by Wimberger-Friedl and de Bruin (1993) and by Kapteijns (1993) for several sets of processing conditions, using a Schlieren optical technique. In figure 5.1 the product geometry is shown. The thickness of the rectangular part is 2 mm. The thickness of the divergent part varies bilinearly from 1.86 mm at the line of symmetry to 2 mm at the upper and lower edges to obtain a straight flow front at the end of this part. The gate is located at the 10

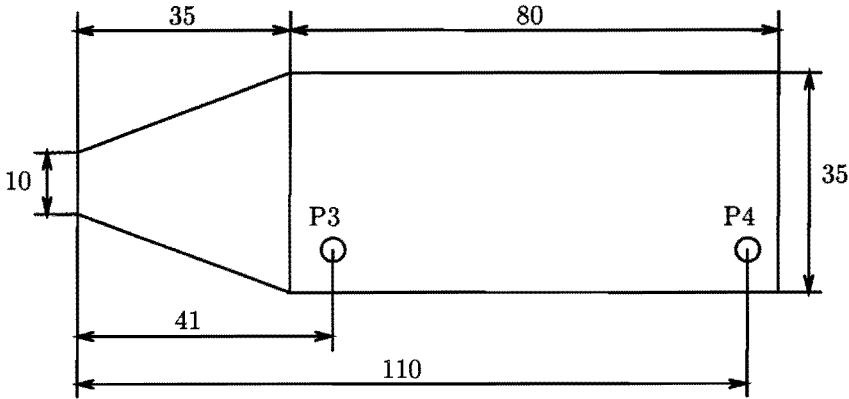


Figure 5.1: Geometry of the test strip, with P3 and P4 the position of two pressure transducers

mm long edge on the left. The symbols P3 and P4 indicate the positions of two pressure transducers. Following Flaman (1990) the compliance of the mould is set to $2.3 \cdot 10^{-13} m/N$.

The cases A to E are taken from Wimberger-Friedl and de Bruin (1993) and case F corresponds to BK12 of Kapteijns (1993). The injection (or entrance) temperature T_e was set to $523 K$ in all cases. Mould temperature T_m and flow rate Q are given in table 5.1. From the experimen-

Case		A	B	B-	B+	D	E	F
T_m	K	303	333	333	333	303	363	333
Q	$10^{-6} m^3/s$	7.63	7.63	7.63	7.63	1.27	7.63	25.43

Table 5.1: Processing conditions for cases A, B, B-, B+, D and E

tal results it was concluded that the material at the surface of the product did not solidify instantly (see Wimberger-Friedl and de Bruin (1993)). Therefore, a Biot boundary condition (see equation (2.72)) is employed for the temperature equation (2.70). The heat transfer coefficient chosen is $H_m^+ = H_m^- = 3 \cdot 10^3 J/(smK)$, so that the position of the peaks in the gap-wise density distributions found numerically coincided more or less with the experimental ones (see e.g. figure 5.4). Unfortunately the pressure measurements, required as a boundary condition during the postfilling stage, were

not available for all cases. However, for the cases A, B and E the hydraulic back pressure was equal during the experiments. Consequently, the necessary, prescribed pressure at the gate p_e is taken from experiment B for the three cases mentioned. No holding pressure is applied for case D. The cases B- and B+ correspond with an descending and ascending holding pressure in time. The prescribed non-zero holding pressure profiles are shown in figure 5.2.

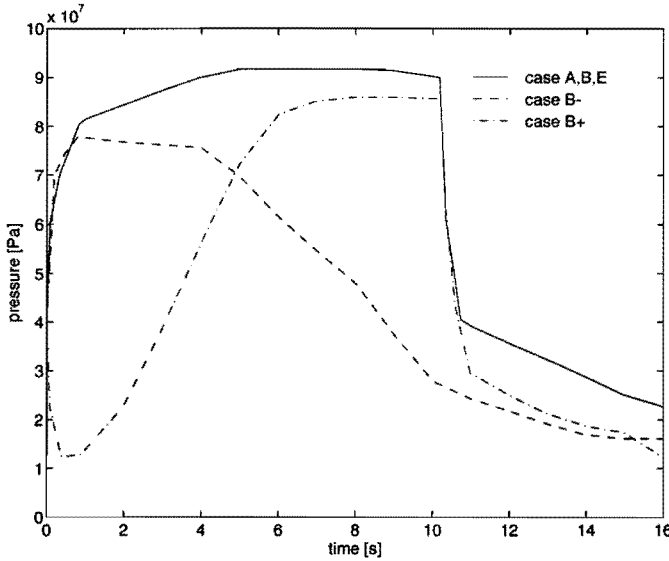


Figure 5.2: Prescribed holding pressures (i.e. after filling) at the gate for cases A, B, E, B- and B+

The 7-constant Cross model (equation (2.52)) is used to describe the shear viscosity η as a function of shear rate, temperature and pressure (table 4.1). The heat capacity c_p is modelled using equation (2.46) and the parameters from table 4.10. The thermal conductivity λ is chosen $0.19 \text{ W}/(\text{m}^2\text{K})$. The specific volume ν is modelled by the KAHR model (equation (2.9)), using the parameters from table 4.6 for the equilibrium behaviour, $\Delta\alpha$ from the TMA experiments and $\Delta\kappa_0$, κ_1 from the pvT experiments (table 4.7). The remaining KAHR parameters are taken from table 4.8. The relaxation spectrum is discretised according to equation (3.14) with the number of discrete relaxation times $m_\delta = 8$. To reduce the computational effort, a decoupled approach can be employed to compute the specific volume ν , by using the Tait equation (2.6) for both the melt and the solid state in the pressure and temperature equations (2.65), (2.70) and

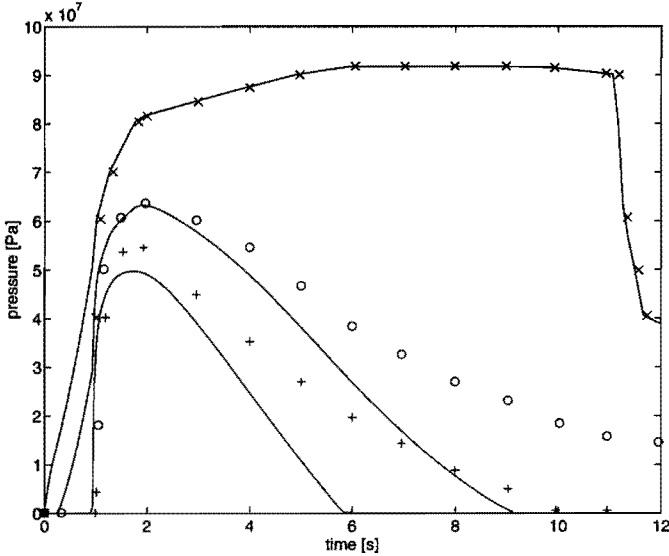


Figure 5.3: Measured (symbols) and computed (lines) pressure history at the gate (x), at P3 (o) and P4 (+) for case B

recompute the specific volume by the KAHR model afterwards. Therefore, the Tait model was fitted on the numerical isobaric cooling experiments at 25 K/s using the KAHR model (see table 4.6 under TMA for the parameters). In general, the computed pressure and temperature during the postfilling stage is highly sensitive to the specific volume behaviour of the material used. In one case, that could be considered as being representative for all other cases studied, the decoupled approach resulted nevertheless in deviations in predicted pressure, temperature and density distributions that were within a few percent only of the results of the fully coupled calculations. Therefore, the decoupled approach is used in all cases presented here.

Results

In figure 5.3 both the experimental and the computed pressure histories at the gate and at positions P3 and P4 are shown for case B. The filling pressure is overestimated by the model (not indicated). Reduction or omission of the pressure dependence of the viscosity (i.e. $0 \leq s_0 < 3.0$ in equation (2.52)) only marginally lowers the viscosity and thus the predicted filling pressure. The pressure during the postfilling stage is clearly underpredicted by the model. The use of the Tait parameters from the $p\nu T$ measurements (see

table 4.6) instead of those from the TMA experiments does not improve the results significantly. Variation of the heat transfer coefficient or of the heat conduction coefficient has hardly any effect on the computed pressure history. The deviation from the experimental curves remains unexplained. Figure 5.4 shows the experimental and the computed distribution across

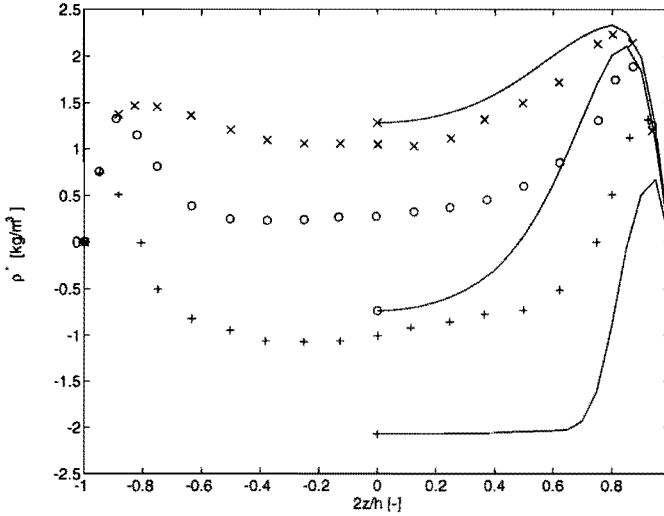


Figure 5.4: Measured (symbols) and computed (lines) reduced density distributions across the (normalised) thickness at 8, 28 and 107 mm from the gate (case B)

the normalised thickness of the reduced density $\rho^* = \rho - \rho_s$ for case B at several positions along the flow path, with ρ_s the density at the surface ($z = h/2$). The density is only computed for half the gap width as the problem is symmetrical. Qualitatively the agreement is satisfactory, quantitatively there are still serious discrepancies, as could be anticipated from the poor prediction of the pressures. The typical density distribution can be explained by the pressure during vitrification. Near the gate the pressure is high during solidification of the entire thickness, except for the thin surface layers that solidify during filling. At the end of the flow path, the solidification starts at the wall when the holding pressure is already partially applied as cooling is delayed by the Biot boundary condition. The maximum pressure is lower than at the gate and drops to zero during the solidification. Although the absolute value of the density (not shown here) is not accurately predicted, the difference between minimum and maximum values corresponds well with the experiments. As mentioned

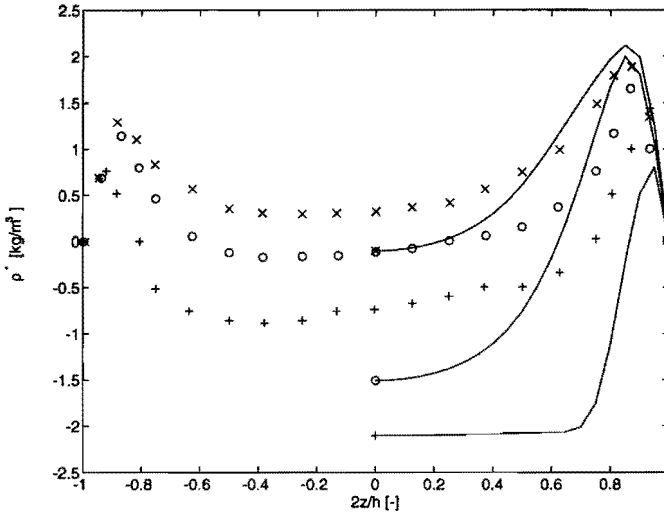


Figure 5.5: Measured (symbols) and computed (lines) reduced density distributions across the (normalised) thickness at 8 (x), 28 (o) and 107 (+) mm from the gate for case B-

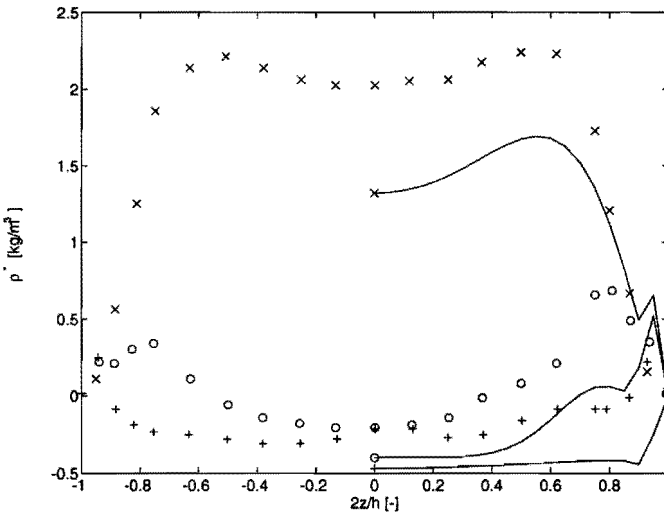


Figure 5.6: As figure 5.5, but now for case B+

above, the difference between numerical and experimental results may be explained by a rather poor prediction of the pressure history and the rough estimate of the heat transfer and heat conduction coefficient, governing the temperature history, which in this case leads to solidification of the core under zero pressure. The absolute value of the density at the surface ($z = h/2$) found numerically is not constant, but varies from 1171.3 kg/m^3 at 8 mm from the gate to 1170.3 kg/m^3 at 107 mm .

Packing pressure The dominating influence of the pressure on the density distribution is illustrated by figures 5.5 and 5.6, showing the experimental and computed reduced density distributions for cases B- (descending holding pressure) and B+ (ascending holding pressure) at 8 , 28 and 107 mm from the gate. The results for case B- show that the density gradient along the flow path is smaller than for the previous case, for the experiments as well as for the simulations. Again a rather poor prediction of the pressure history leads to exaggerated density gradients in gapwise direction. For case B+ the holding pressure obviously did not reach the end of the cavity and was very small at 28 mm from the gate, both for the experiments and the simulations, so the qualitative agreement can be judged to be satisfactory.

Injection speed Wimberger-Friedl and de Bruin (1993) stated that the different surface and core densities at the end of the cavity are caused by the fact that during filling the solidified layer thickness remains (almost) zero, so that the surface solidifies under pressure. Case D, for which a low injection rate and zero holding pressure was prescribed, was chosen to make sure that the surface would solidify under zero pressure. The results are shown in figures 5.7, 5.8. The relatively high computed density gradients in thickness direction are caused by an overestimated filling pressure. The relatively narrow density peak at the gate is in agreement with the experiments. This effect is caused by the removal of the pressure after filling (causing remelting of the solidified layer near the gate) in combination with a slower layer growth due to convective heat transport. The effect found experimentally of a higher density at the surface than in the core near the gate is predicted as well and is caused by a delayed solidification of the surface. The opposite of this effect is found only numerically at 48 and 108 mm from the gate. This is caused by a higher cooling rate at the surface than in the core (compare lines 1 and 3 in figure 1.2).

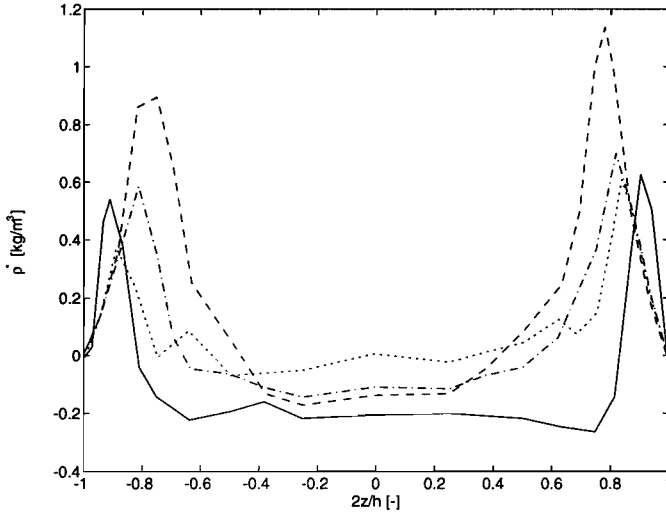


Figure 5.7: Measured reduced density distributions across the (normalised) thickness at 8 (full line), 28 (dotted line), 48 (dashed line) and 108 (dash-dotted line) *mm* from the gate (case D)

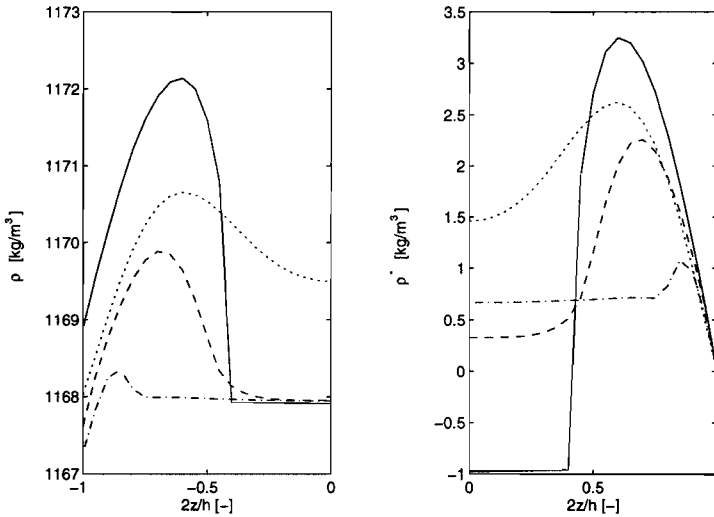


Figure 5.8: Same as 5.7, but now for the absolute (left) and reduced (right) computed density

Mould temperature Cases A, B and E are compared to assess the influence of the mould temperature on the resulting density distribution (figure 5.9). The decreasing *maximum* density with increasing mould temperature found experimentally is hard to explain, since a higher formation pressure and lower cooling rate are in favour of the opposite effect. The simulations predict this decrease in peak height close to the wall with increasing wall temperature correctly. The computed average density (not shown here) increases, however, with increasing mould temperature, which contradicts independent measurements of the gapwise averaged density (see Wimberger-Friedl and de Bruin (1993)).

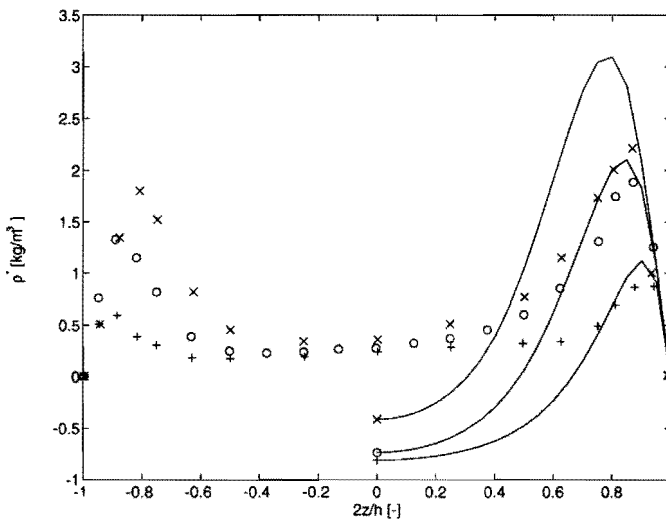


Figure 5.9: Measured (symbols) and computed (lines) reduced density distributions across the (normalised) thickness at 28 mm from the gate for cases A (x), B (o) and E (+)

Ageing Kapteijns (1993) extended the experiments to study the effect of accelerated ageing on the density distribution. The samples were aged for one hour at 333 K and at 363 K (see figure 5.10). The average density decreased during ageing, further away from its equilibrium. This effect is caused by a relaxation of the pressure induced densification, which is faster than the normal volume relaxation towards equilibrium. A U-shaped profile resulted after the ageing at the highest temperature, for which no explanation has been found yet. In figure 5.11 the corresponding computed density distributions are plotted. Besides the fact that the absolute values are dif-

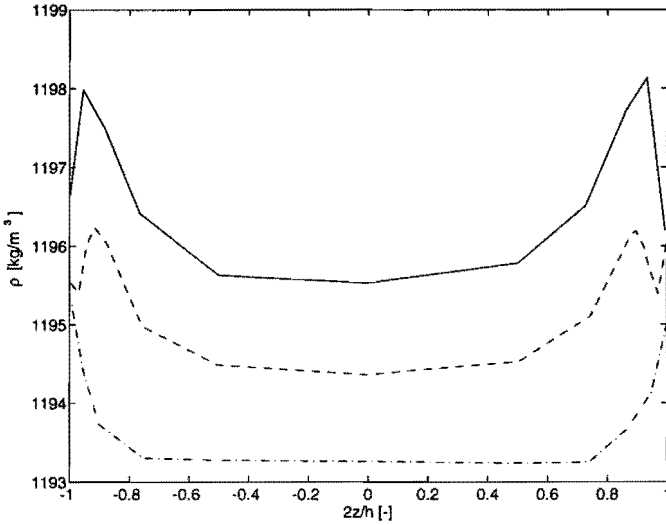


Figure 5.10: Measured density distributions across the (normalised) thickness at 27 mm from the gate (case F): unaged (full line), after 1 hour at 333 K (dashed line) and after 1 hour at 363 K (dash-dotted)

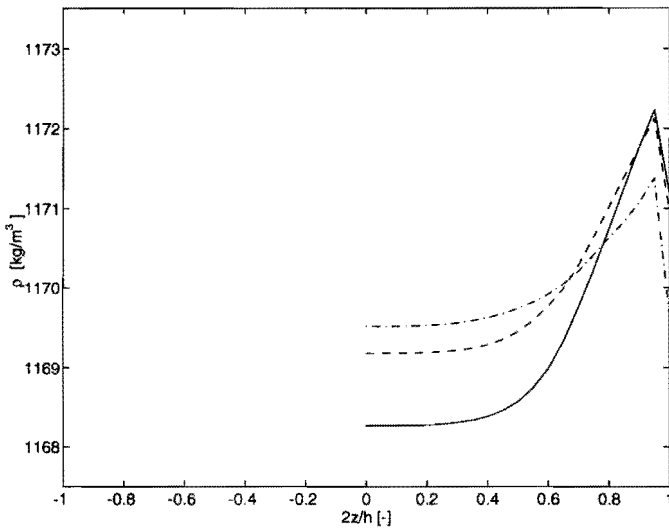


Figure 5.11: Same as figure 5.10, but now the for the computed density

ferent (which could be caused by the different expansion coefficient α_m from the $p\nu T$ and the TMA experiments), the relaxation of the pressure induced densification is apparently not present in the simulations, as the average density increases. This may be caused by the fact that the pressure during cooling is underestimated by the model, so that part of the cross section solidified under zero pressure. As can be seen in figure 5.12, which shows the gap-wise averaged density evolution at the gate at 343 K, the temporary expansion and the following contraction towards the equilibrium density can be predicted qualitatively for higher pressures.

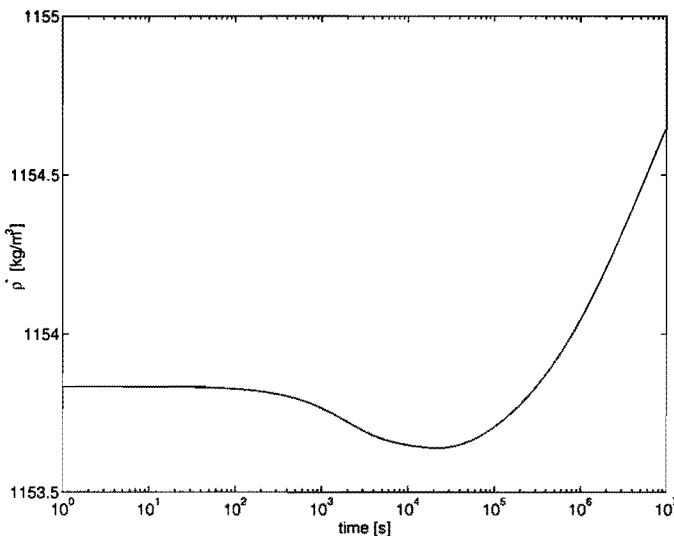


Figure 5.12: Computed averaged density evolution at the gate (case F)

5.2 Thermally induced residual stress

Zoetelief *et al.* (1995) showed that the multi-mode Maxwell model is capable of predicting the thermal residual stresses for injection moulded products, although it tends to overpredict the measured values. Here, a two-shot moulding process is taken as an example, because the asymmetrical cooling of the product often leads to severe warpage. This process starts with a regular injection moulding cycle, in which the first shot is moulded. However, the product is not ejected, but one mould half is removed to make place for a new one, that doubles the thickness of the original cavity. During the replacement of the mould half, one side of the product is cooled by

air. Depending on the kinematic boundary conditions, thermal stresses may equilibrate. The new cavity, of which the walls are formed by the new mould half on one side and the first shot on the other, is filled by the second shot.

Geometry, processing conditions and material parameters

Figure 5.13 shows the product geometry used. The product thickness is 1.5 mm. From previous numerical studies (see Ramaekers (1992) and Caspers

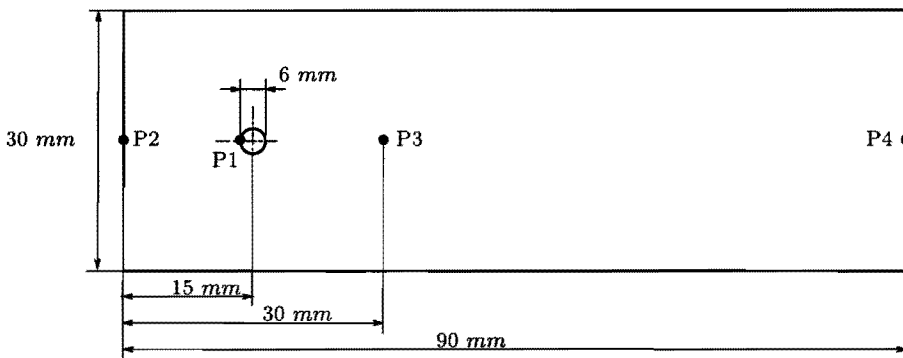


Figure 5.13: Geometry of the test product after the first (left) and after the second shot

et al. (1994a)) it was concluded that of all processing conditions, the level of the holding pressure is of major influence on the distribution of thermally induced residual stress and consequently on the resulting warpage. Main difference with the present study is that, in stead of a line gate, here the cavity is fed by a runner. The runner itself, however, is not modelled here, (although incorporation is quite possible, see appendix E) but is replaced by a “circular line gate” at position P1. Four cases are studied. For the first case (G) the hydraulic back pressure was chosen $5 \cdot 10^7 Pa$ for both the first and second shot. The first shot of case H was the same as that of case G. During the second shot, however, no holding pressure was applied. For case I there was no packing of the first shot, but conditions for the second shot were equal to those of case G. For case J finally, no holding pressure was applied during both shots. The holding pressure is prescribed until the gate solidifies. In figure 5.14 the pressure histories at P1 are shown for cases G to J. The other processing conditions were the same for all cases and are listed

in table 5.2. A heat transfer coefficient of $H_m^+ = H_m^- = 3 \cdot 10^3 J/(smK)$ is assumed. For both the first and the second shot the mould is not opened until the product is completely solidified.

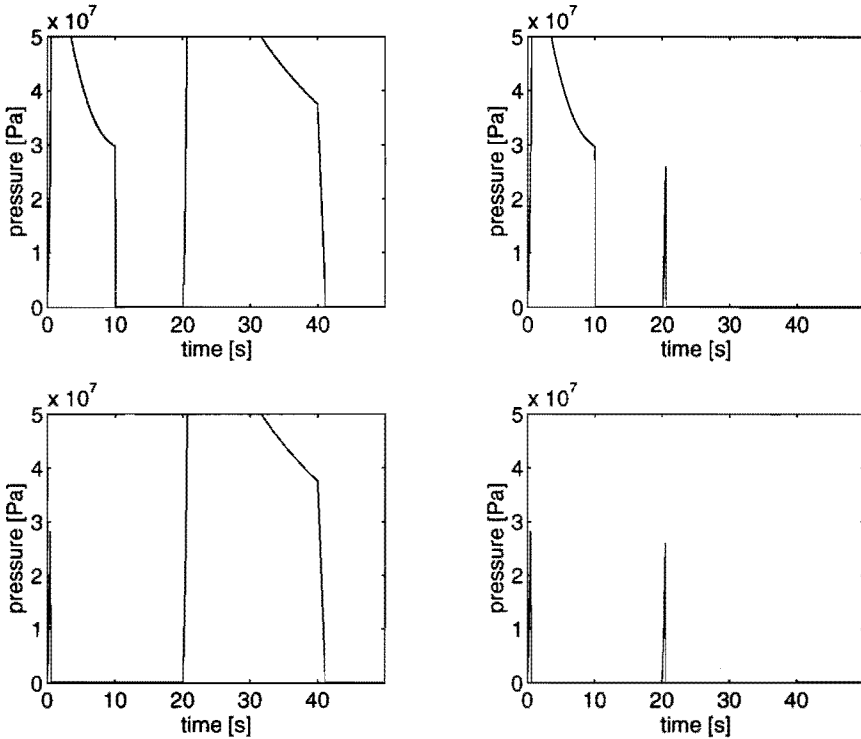


Figure 5.14: Pressure as a function of time at P1 for both sequential injection moulding cycles for case G (top left) case H (top right), case I (bottom left) and case J

T_e	K	T_m	K	Q	$10^{-6} m^3/s$
473		323		8.75	

Table 5.2: Processing conditions for the cases G, H, I and J

The material used is PS 678E. Viscosity data are taken from table 4.2 (steady state Leonov model, equation (2.48)). The specific volume is described by the double domain Tait equation (2.6) of which the parameters are listed in table 4.9. Heat capacity is described by equation (2.46) and the

corresponding parameters can be found in table 4.10. A constant value of $0.17 \text{ W}/(\text{m}^2\text{K})$ is taken for the heat conduction coefficient λ . The Cauchy stress tensor for the computation of thermal stresses is described by the Maxwell model, presented in subsection 2.2.2. The parameters of this model are listed in tables 4.3 and 4.5. Since the pvT behaviour is described by the Tait model, the index ∞ and the second right-hand-side term should be removed from equation (2.33). Thus the effect of the viscoelastic bulk modulus is neglected. From preliminary investigations it was found that incorporation of the KAHR model hardly affects the computed stress distribution in similar cases, although they tend to become flatter.

Results

In figure 5.15 the computed pressure histories at P1, P2, P3 and P4 are shown for case G. The holding pressure is computationally maintained until the gate freezes of. This takes longer for the second shot as it is cooled on one side by the (insulating) first shot. This lower cooling rate results also into a lower filling pressure of the second shot (not indicated).

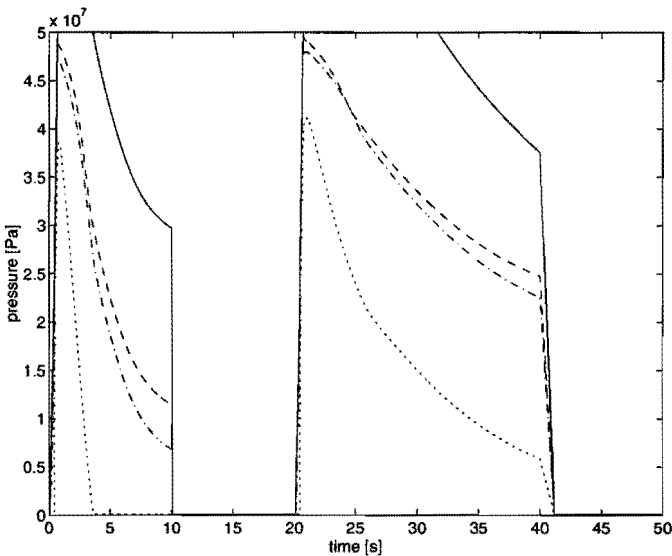


Figure 5.15: Pressure as a function of time at P1 (full line), P2 (dashed line), P3 (dash-dotted) and P4 (dotted) for both sequential injection moulding cycles for case G

Figure 5.16 shows the computed temperature distribution after packing and before and after opening the mould for the first and the second shot. The first shot shows an asymmetrical temperature distribution after removal of one mould half, due to the cooling by the (relatively cold) air. After the second shot has been injected, the first shot is heated to above the glass transition temperature. During cooling, the temperature distribution becomes symmetrical.

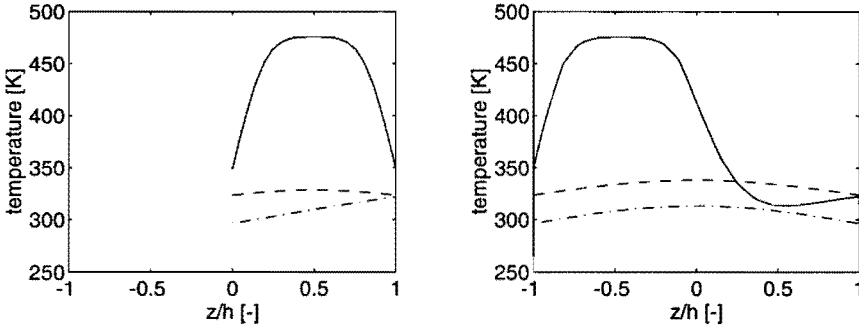


Figure 5.16: Computed temperature distribution at various stages of the two-shot moulding process at P3 (case G). Left: first shot after packing (full line), before ejection (dashed line) and after removal of the mould half to be replaced (dash-dotted). Right: second shot after packing (full line) before ejection (dashed line) and after ejection (dash-dotted)

For the stress computation it is assumed that during the switch of one of the mould halves, stresses cannot equilibrate, although the geometry would allow this. The computed stress distributions at P3 after filling and after packing of the first shot, before and after filling and after packing of the second shot and after ejection of the total product are shown in figure 5.17 for case G. For the upper two plots the multi-mode Maxwell model is used, the lower two plots are according to the viscous-elastic model (see appendix C), using a constant modulus of $906 \cdot 10^6 N/mm^2$ for the solid state. The severe asymmetry of the resulting stress profile is caused by the erasure of part of the thermal stress in the first shot, the higher pressure during solidification of the second shot, and the asymmetric cooling of this shot.

For the computation of the resulting warpage, all displacements and rotations at P2 were prescribed zero. As the rotation around the normal of the midsurface is eliminated (see equation (3.45)), an additional degree of freedom of a neighbouring node was fixed as well. The warpage as a result of the thermal stresses is shown in figure 5.18 for cases G to J. Due to the use

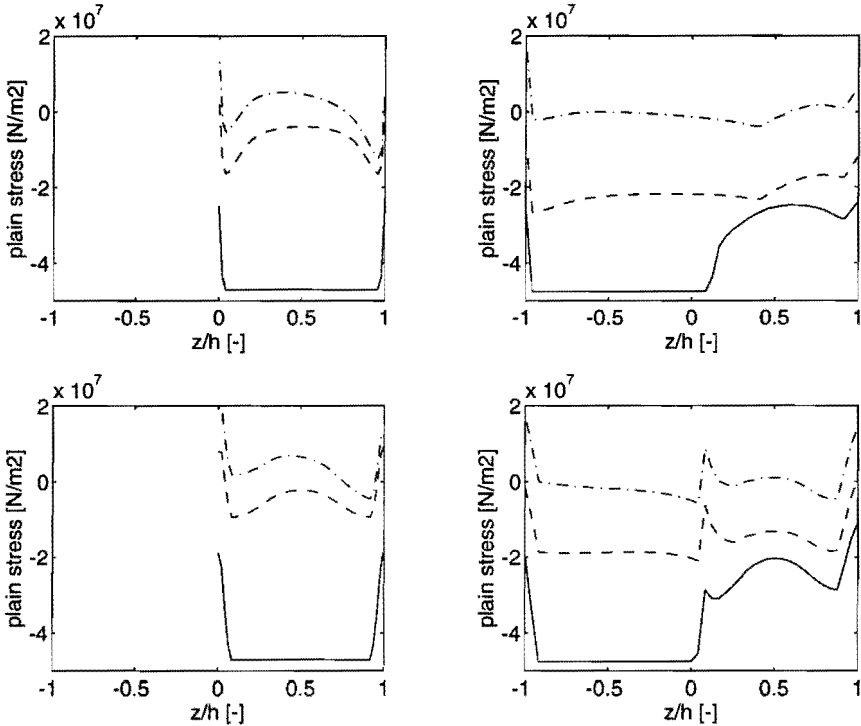


Figure 5.17: Same as figure 5.16 but now for the plain stress. Top: multi-mode Maxwell model; bottom: viscous-elastic model (see appendix C)

of a runner instead of a line gate, the product is warped in both directions. The results for cases H and I show that the curvature of the product can change sign, depending on the level of holding pressures. However, when the holding pressure of both shots is chosen equal, this does not result into a warpage free product, as shown by cases G and J.

Although the stress profiles are rather different when the viscous-elastic approximation is employed, the resulting warpage is hardly different for case G. The computed normal displacement at P4 was 2.49 mm in the viscoelastic case, where for the viscous-elastic case 2.50 mm was found. Also case H is rather insensitive to the model used (-5.11 mm for the viscoelastic model and -5.73 mm for the viscous-elastic approach). However, the viscous-elastic model leads to a doubled displacement at P4 for case I ($4.03, 8.65 \text{ mm}$). Also for case J the difference is significant ($-3.53, 0.13 \text{ mm}$ respectively). The difference is mainly caused by the entirely different stress relaxation behaviour in the first shot when it is heated by the second shot.

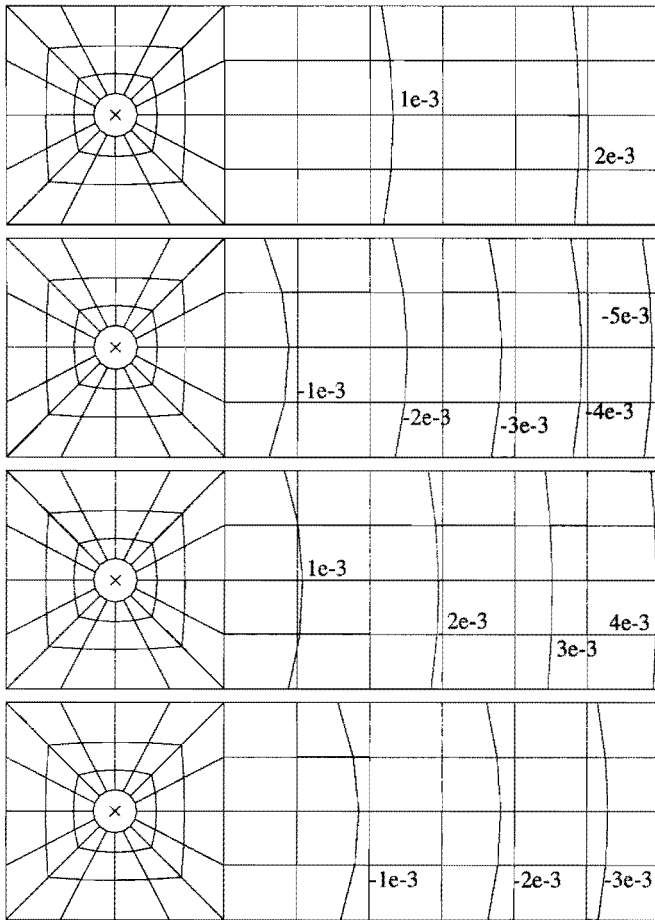


Figure 5.18: Computed normal displacements for (from top to bottom) cases G, H, I and J

To assess the influence of the kinematic boundary conditions while one of the mould halves is being replaced, three additional cases were studied, which are all based on case G, employing the viscous-elastic approach. When, during the switch of the mould half, shrinkage was allowed for in both the length and width directions of the product, (all rotations are still prescribed zero), the resulting normal displacement at P4 became -0.55 mm in stead of 2.50 mm . When shrinkage was only allowed for in the width direction of the product between the first and second shot, this displacement became 2.62 mm , which, unlike the totally constrained and the previous case, was the maximum absolute value. When only shrinkage in the length direction

of the product was allowed for, this led to -1.66 mm displacement, again the absolute maximum value, but in opposite direction.

5.3 Flow-induced residual stress

The experimental results for case K, for which the flow-induced residual stresses are calculated, are taken from Flaman (1990). The product geometry is equal to that of cases A to F. The material used is PS 678E, so the material parameters are equal to those of cases G to J. The parameters for the Leonov model (equations (2.21) to (2.25)) are listed in table 4.2. The processing conditions are listed in table 5.3. The pressure at the gate, which is prescribed during holding, is shown in figure 5.19. Again the heat transfer coefficient is chosen $3 \cdot 10^3 \text{ J}/(\text{smK})$.

T_e	K	T_m	K	Q	$10^{-6} \text{ m}^3/\text{s}$
493		326		7.62	

Table 5.3: Processing conditions for case K

Results

The measured and the computed pressure histories at the gate, at P3 and P4 are shown in figure 5.19. Like for case B, the filling pressure is overestimated and the postfilling pressure is underestimated. The flow-induced stresses cannot be measured directly, but can be assessed by measurement of the birefringence. The stress-optical coefficient of PS (correlating the stress tensor and the refractive index tensor) in the glassy state is about 400 times lower than in the molten state. Therefore, the contribution to birefringence of thermal stresses can be neglected compared to that of flow-induced stresses. From Wimberger-Friedl (1991), Chapter 3, it is known that thermal stresses at and above T_g may induce extra orientation (and birefringence). It is assumed that this extra contribution can be neglected compared to the orientation induced by flow during filling and packing. From the flow-induced residual stress distribution, the birefringence is computed using (see Janeschitz-Kriegl (1983)):

$$\Delta n = C_0 \sqrt{(\sigma_{11} - \sigma_{33})^2 + 4\sigma_{13}^2} \quad (5.1)$$

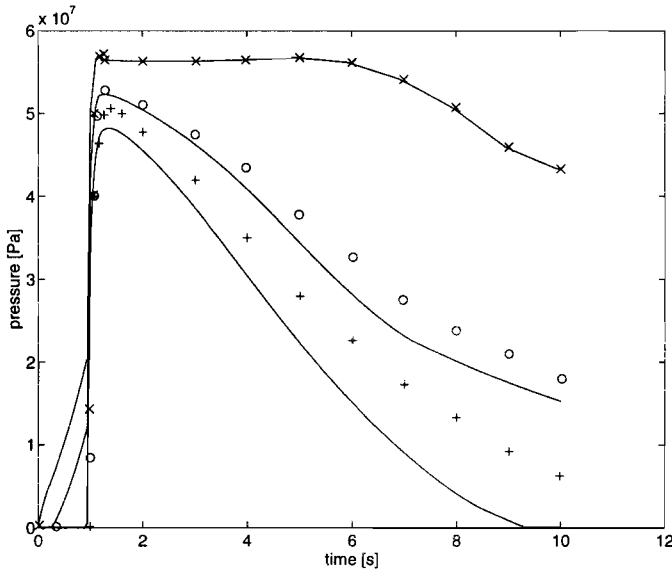


Figure 5.19: Computed (lines) and measured (symbols) pressure histories at the gate (x), at P3 (o) and at P4 (+) (case K)

with C_0 the linear stress optical coefficient, σ_{11} the stress in flow direction and σ_{33} the stress in thickness direction. The stress optical coefficient is taken $-4.8 \cdot 10^{-9} \text{ m}^2/\text{N}$ in accordance with Flaman (1990). The build-up of the birefringence distribution at 25 mm from the gate is shown in figure 5.20, where the distributions after filling, after packing and the residual distribution are plotted. The computed and measured gapwise residual birefringence distribution at 25 , 41 , 60 and 110 mm from the gate is shown in figure 5.21.

The predictions are remarkably accurate (especially compared to similar calculations performed by Flaman (1990) and Douven (1991)), except for the distribution at 25 mm from the gate. This deviation is located only at the peak caused by the flow during holding, so it cannot originate from the three dimensional character of the flow, nor by the omittance of the convective term in equation (2.24). However, the computed birefringence distribution at the same distance from the gate, but more near the edge of the product does correspond to the birefringence distribution, found experimentally. Some asymmetry during the postfilling of the strip might be the cause of the deviation.

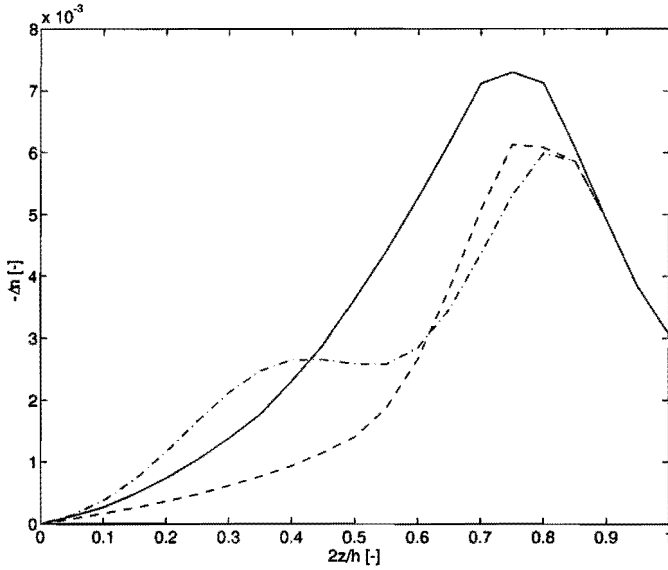


Figure 5.20: Computed birefringence across the thickness at 25 mm from the gate after filling (full line), after packing (dashed) and residual distribution (dash-dotted) (case K)

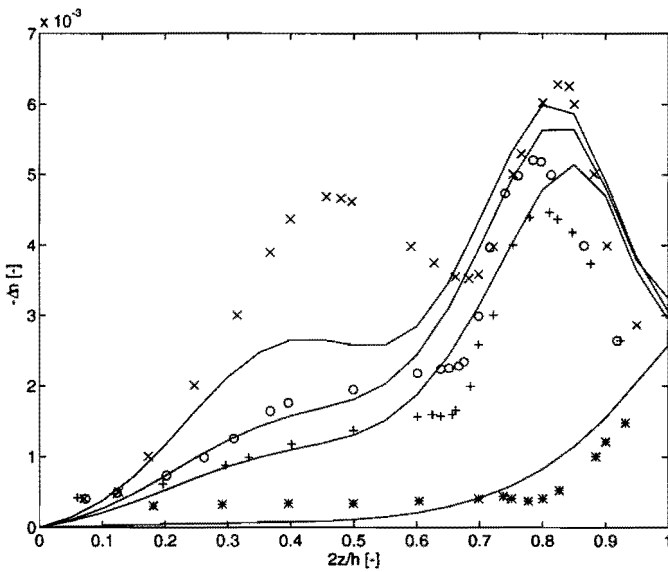


Figure 5.21: Measured and computed (full lines) residual birefringence across the thickness at 25 (x), 41 (o), 60 (+) and 110 (*) mm from the gate (case K)

5.4 Elastic recovery

Volume relaxation and elastic recovery are the most important factors governing the dimensional stability. Case L, known as PS9 in Schennink (1993), from which the experimental data are taken, is used to illustrate this.

Geometry, processing conditions and material parameters

The same geometry of cases A to F is used. The processing conditions are listed in table 5.4. The pressure history, prescribed at the gate during the holding stage, is shown in figure 5.22 (upper full line). The material parameters and models used are the same as those of case G to J. The parameters for the Voigt model are listed in table 4.4 and 4.5.

T_e	K	T_m	K	Q	$10^{-6} m^3/s$
473		328		7.63	

Table 5.4: Processing conditions for case L

Results

Figure 5.22 shows the pressure history at the gate and at P3 and P4. Again the filling pressure is overpredicted while the pressure during cooling is underpredicted. The dimensional change of the length of this part was measured as well as of the width (i.e. not the thickness but the perpendicular direction) at 75 and 110 *mm* from the gate. The storage temperature chosen was 343 *K*. At this storage temperature, the strain due to volume relaxation, computed using the KAHR model, is approximately $1 \cdot 10^{-3}$ on the time scale studied, which is negligible compared to the strain caused by elastic recovery. The measured and computed strain as a function of time is shown in figure 5.23. The computed strain compares well with the experimental values, only the time scale differs one decade. When the storage temperature is chosen 20 *K* lower, the strain due to volume relaxation is still approximately $1 \cdot 10^{-3}$, while the computed strain caused by elastic recovery is two orders smaller than that. This effect was measured as well. This means that the dimensional stability at temperatures close to T_g is governed by elastic recovery, while at lower temperatures the volume relaxation becomes dominant.

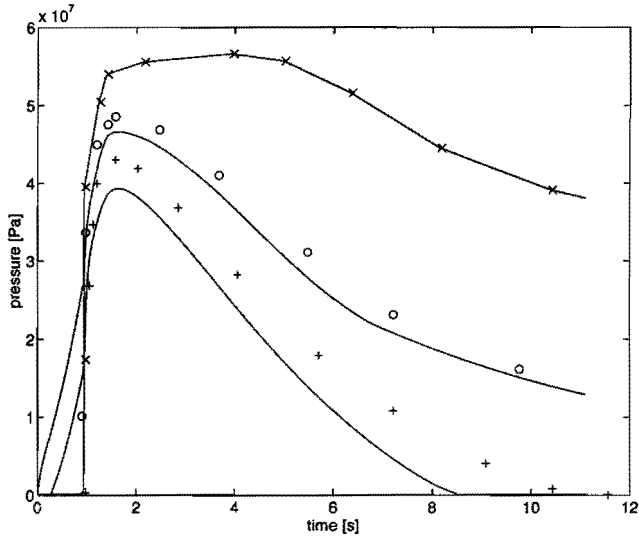


Figure 5.22: Measured and computed (lines) pressure as a function of time at the gate (x), at P3 (o) and P4 (+) (case L)

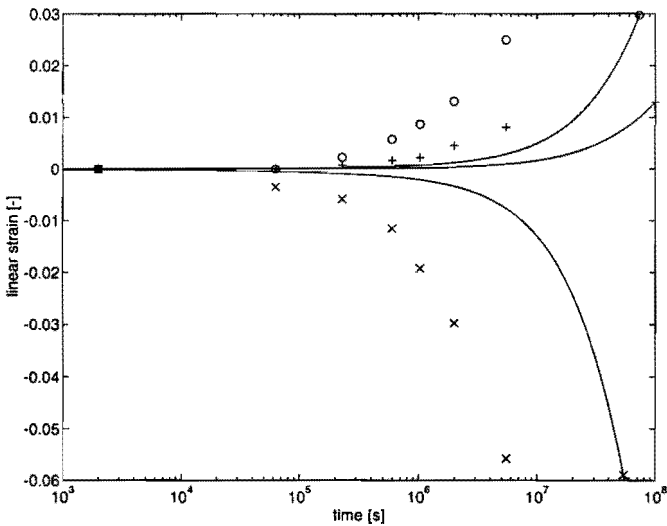


Figure 5.23: Measured (symbols) and computed (lines) strain due to recovery of the length of the rectangular part (x), of the width at 75 (o) and 110 (+) mm from the gate (case L) with a storage temperature of 343 K

5.5 Discussion

The simulation code developed is capable of predicting the pressure history inside the mould. However, all cases show a structural overprediction of the filling pressure and an underprediction of the pressure history during cooling. The former may be improved by measurement of the pressure dependence of the viscosity more accurately. The latter is highly sensitive to the (modelled) $p\nu T$ behaviour, but also the computed temperature history is important. The interpolation at each time step to the modified grid along the thickness of the product (due to a new solidified layer thickness, see figure 3.1), introduces some numerical diffusion, leading to faster cooling. But most important is the lack of accurate data for the heat conduction tensor λ and the heat transfer coefficient H_m . The latter may be obtained by modelling the thermal behaviour of the mould.

It has been shown that usage of the KAHR model can help to interpret the density distributions found experimentally in injection moulded parts and that this model is able to predict these distributions at least qualitatively. The effects of accelerated ageing on the density distribution can be predicted as well, except for the U-shaped density profile found experimentally after extreme ageing. There is no physical explanation for this particular profile yet. Also it was shown that the determination of the parameters of the KAHR model using a thermomechanical analyser, gives relatively good results. Accuracy can be improved by employing dilatometry. It was found that an accurate prediction of pressure and temperature histories is essential for a reliable prediction of the density distribution and volume relaxation.

Unfortunately no experimental results were available to validate the predicted thermal stress distributions, nor the resulting warpage. The warpage of a layered two-shot moulded part can be manipulated by the level of the holding pressure for both shots. The warpage is also governed by the exact kinematic boundary conditions between the first and second shot. It has been shown that the use of a viscous-elastic model in stead of the multi-mode Maxwell model may lead to entirely different stress distributions and warpage.

The compressible Leonov model predicted, using a stress optical law, the birefringence found experimentally in polystyrene injection moulded strips remarkably well. The birefringence as computed by Douven (1991) was a factor three larger for the case studied, while the material parameters used were the same. This discrepancy may be explained by the different numerical methods used. The influence of the cooling stresses on birefringence, but also

on orientation (see Wimberger-Friedl (1991)) is apparently not present in the case studied.

The effects of elastic recovery can be predicted by the Voigt model with its material parameters fitted on linear viscoelastic measurements. However, the time scales of the experimental and the computed results differ one decade. A deviation of 3.5 to 4 K between the temperature during the rheological characterisation and the temperature during recovery could explain this difference. Extra creep experiments may give the explanation.

Chapter 6

Concluding discussion

An integral approach is described for the development of a computational method for the simulation of the injection moulding process, including the prediction of long term mechanical behaviour of the moulded product as a function of processing conditions and polymer properties. Stability and convergence of the numerical methods applied are validated. The methods are implemented into a computer program (VIP) and the results are compared with experimental data. Precision of an injection moulded product, being defined as a desired distribution of a number of properties as a function of time, can be predicted by the program for amorphous thermoplastics, for which density, orientation and thermally induced residual stress distributions determine the dimensional accuracy and stability. The predictions are in satisfactory agreement with experimental results.

The general conclusions drawn from the study can be summarised as:

- Given the $2\frac{1}{2}$ D approximation, the use of higher order elements for the spatial discretisation of the pressure field is essential for an accurate computation of the velocity field as input for the evaluation of material derivatives.
- The history dependent KAHR model applied for the specific volume in combination with the Leonov model for flow-induced residual stress and the Voigt model for elastic recovery enables the prediction of the dimensional stability for amorphous thermoplastics. At temperatures close to the glass transition temperature, the dimensional stability is governed by elastic recovery. At lower temperatures, volume relaxation becomes dominant.

- An important parameter that determines the pressure field during the holding and cooling stages of the injection moulding process besides viscosity is the density as a function of pressure, temperature and time. If the history dependency of the density is neglected, the predicted pressure is hardly different. This enables a decoupled approach for the computation of density distributions.
- All effects found experimentally concerning the density distribution in injection moulded parts, can be predicted qualitatively by the KAHR model used in this study.
- The incorporation of viscoelasticity in the model for the bulk-modulus is of minor influence on the computed residual thermal stress distribution.
- The computed residual thermal stresses and the resulting warpage of layered two-shot moulded parts can be manipulated by the level of the holding pressure for both shots. However, the exact kinematic boundary conditions for the first shot during the replacement of one mould half are also of major influence on the computed stresses and warpage.

Based on these results, the following recommendations and considerations concerning future research in this field can be given:

- The $2\frac{1}{2}$ D approximation excludes the possibility to predict local product properties like sink marks and, more important, severely limit the accuracy of the particle tracking method. To improve this, a full 3D analysis must be considered. Extension of the existing model towards reaction injection moulding requires the incorporation of gravity and inertia forces, as the viscosities are generally much lower for reactive materials. For that reason a full 3D approach may be necessary, in combination with a spectral element method (see e.g. Timmermans (1994)).
- The predictive capability of the model in terms of pressure, temperature and product properties can be improved when the thermal behaviour of the mould is incorporated into the model. However, the improvement may be limited, due to a lack of accurate experimental validation techniques.

- The computed orientation distribution in the moulded product enables the incorporation of anisotropy in material properties like heat conduction and elasticity modulus. A precise experimental validation of this will, however, again be complex.
- The present model can be (and partially is) extended to simulate similar processes like resin transfer moulding, compression moulding and gas-assisted injection moulding.

For resin transfer moulding the fluidity in the pressure equation is replaced by a permeability tensor. Material properties of the resin are averaged by volume with those of the porous medium. Depending on the viscosity of the resin and the permeability of the medium, incorporation of gravity may be important. As the resin is usually a thermoset, also heat of reaction and the influence of degree of reaction on material properties have to be modelled.

For compression moulding a term must be added to the pressure equation to account for the changing gap width. In reality the front propagation is governed by the relative velocity of the mould halves, but a user defined average front propagation, from which the change in gap width and time step are computed, seems preferable for the simulation.

The modelling of gas-assisted injection moulding requires the incorporation of an accurate particle tracking technique (see e.g. Zoetelief (1995)) as well as a model to compute the resulting wall thickness.

- The incorporation of crystallisation kinetics into the existing model would strongly improve its practical relevance. Since *shear-induced crystallisation* has appeared to be an important aspect, however, the major problem will be the formulation of an accurate model and moreover the determination of its parameters.

Appendix A

Accuracy of pressure element

A.1 Description of a test case

The following test case is used to establish to what extent natural boundary conditions are obeyed using subsequently four different element types (see figure A.1).

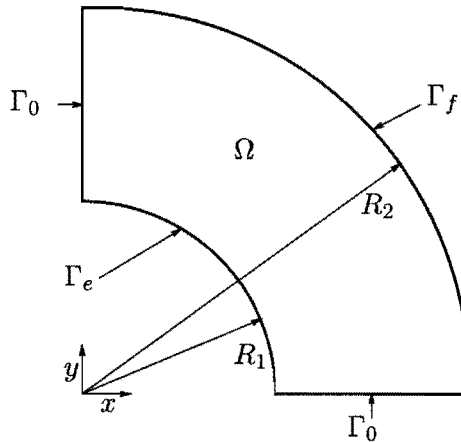


Figure A.1: Domain and boundary definition for the test case

$$\Delta p = 0 \quad (\Omega) \quad (\text{A.1})$$

$$p = 0 \quad (\Gamma_f) \quad (\text{A.2})$$

$$\frac{\partial p}{\partial \vec{n}} \cdot \vec{n} = 0 \quad (\Gamma_0) \quad (\text{A.3})$$

$$\frac{\partial p}{\partial \vec{n}} \cdot \vec{n} = 1 \quad (\Gamma_e) \quad (\text{A.4})$$

with \vec{n} the outward normal vector of the boundary. The radii R_1, R_2 are 1.0, 2.0 respectively. The analytical solution for this problem is:

$$p = \ln(2) - \ln\left(\sqrt{x^2 + y^2}\right) \quad (\text{A.5})$$

$$|\vec{\nabla} p| = -\frac{1}{\sqrt{x^2 + y^2}} \quad (\text{A.6})$$

$$\phi = \arctan\left(\frac{y}{x}\right) \quad (\text{A.7})$$

where $\phi - \pi$ is the angle of $\vec{\nabla} p$ with the x -direction.

A.2 Results

Four element types are used to solve the test case: 3-node triangles (lt), 4-node quadrilaterals (lq), 6-node triangles (qt) and 9-node quadrilaterals (qq). In order to make a good comparison the number of elements is chosen in such a way that the total number of degrees of freedom is equal for the different types of elements. The error made in the quantities defined in equations A.5 to A.7 is calculated by:

$$\varepsilon_u = \sqrt{\frac{\sum_{i=1}^N (u_i - u_{i \text{ exact}})^2}{N}} \quad (\text{A.8})$$

with N the number of nodal points. See table A.1 for the results. Comparing the linear element types, only the length of the gradient is somewhat better for the quadrilateral. The use of the 6-node triangle reduces ε_p to a sixth and ε_ϕ to a fourth. The use of the 9-node quadrilateral reduces ε_p to a fifth, $\varepsilon_{|\vec{\nabla} p|}$ to a third and ε_ϕ to a tenth!

The mesh is refined to check the convergence of the element types (see table A.2). For the linear element types the mesh refinement reduces ε_p to a fourth and $\varepsilon_{|\vec{\nabla} p|}, \varepsilon_\phi$ to a third. For the quadratic element types the mesh refinement reduces ε_p to a twelfth and $\varepsilon_{|\vec{\nabla} p|}, \varepsilon_\phi$ to a fourth.

mesh type	10x10 lt	10x10 lq	5x5 qt	5x5 qq
ε_p	$1.31 \cdot 10^{-3}$	$1.31 \cdot 10^{-3}$	$2.30 \cdot 10^{-4}$	$2.39 \cdot 10^{-4}$
$\varepsilon_{ \vec{\nabla}^*p }$	$1.23 \cdot 10^{-2}$	$1.02 \cdot 10^{-2}$	$1.01 \cdot 10^{-2}$	$3.23 \cdot 10^{-3}$
ε_ϕ	$3.53 \cdot 10^{-2}$	$3.59 \cdot 10^{-2}$	$8.43 \cdot 10^{-3}$	$3.62 \cdot 10^{-3}$

Table A.1: Summary of the results for the four element types, 100 degrees of freedom

mesh type	20x20 lt	20x20 lq	10x10 qt	10x10 qq
ε_p	$3.22 \cdot 10^{-4}$	$3.22 \cdot 10^{-4}$	$1.93 \cdot 10^{-5}$	$2.12 \cdot 10^{-5}$
$\varepsilon_{ \vec{\nabla}^*p }$	$4.39 \cdot 10^{-3}$	$3.57 \cdot 10^{-3}$	$2.29 \cdot 10^{-3}$	$7.62 \cdot 10^{-4}$
ε_ϕ	$1.28 \cdot 10^{-2}$	$1.31 \cdot 10^{-2}$	$1.97 \cdot 10^{-3}$	$4.81 \cdot 10^{-4}$

Table A.2: Summary of the results for the four element types, 400 degrees of freedom

A.3 Discussion

Four different element types are used to solve a second order differential equation. The test case has shown that the solution is the most accurate when quadratic triangles are used. However, the derived quantities $|\vec{\nabla}^*p|$ and ϕ are better when biquadratic elements are used, while the solution is almost just as good. As these quantities are used as input data for particle tracking, the biquadratic element is preferred.

Appendix B

Remeshing technique

This appendix describes the method employed to propagate the flow front during the filling of a cavity, meshed with bilinear elements. Front propagation is based on the method used by Sitters (1988) and is extended here for the use of quadrilateral elements.

The method is based on the assumption that every material point on the flow front can be seen as a source, with a strength that is proportional to the magnitude of the local gap-wise averaged velocity or volume flux per unit of length along the front. When the location of the new front is determined, local remeshing is performed by subdividing partially filled elements in filled and empty ones.

Definitions

Figure B.1 shows the basis mesh, that forms the midplane of the (empty) cavity Ω . The polymer flows into the cavity through the injection regions Γ_e . After some time, one or more regions $\Omega_f \subset \Omega$ will be occupied by the polymer. The flow front(s) Γ_f divide(s) Ω into Ω_f and Ω_e , the empty part(s) of Ω (see figure B.2).

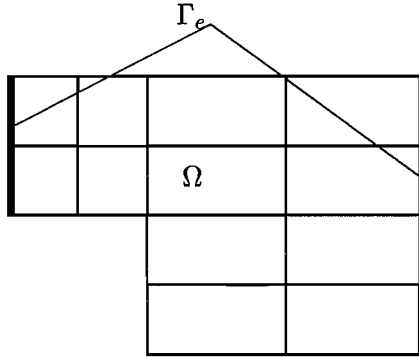


Figure B.1: Basis mesh \mathcal{M}_b with injection boundaries Γ_e

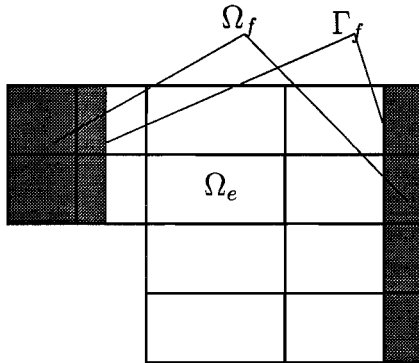


Figure B.2: Partially filled cavity with flow front Γ_f and filled parts Ω_f and empty part Ω_e

In order to compute the pressure and temperature field in Ω_f , the basis mesh must be modified, so that Γ_f coincides with element edges (see figure B.3). The mesh that coincides with the filled part of the cavity Ω_f is

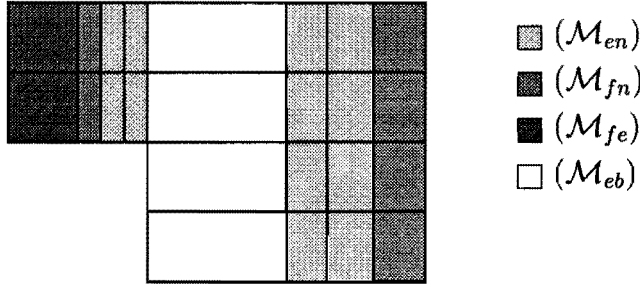


Figure B.3: Subdivided mesh

called \mathcal{M}_f . This mesh can be subdivided into two parts, \mathcal{M}_{fb} and \mathcal{M}_{fn} , where \mathcal{M}_{fb} denotes the set of elements that coincide with elements from \mathcal{M}_b and \mathcal{M}_{fn} is the set of the remaining elements of \mathcal{M}_f . For the empty part of the cavity one can define similar meshes \mathcal{M}_e , \mathcal{M}_{eb} and \mathcal{M}_{en} , the set of empty elements, the empty elements that coincide with elements from \mathcal{M}_b and the remaining empty elements. The complete mesh \mathcal{M}_c is defined as the set of elements in \mathcal{M}_f and in \mathcal{M}_e .

The filling state of an element is defined by the filling state of its edges. As the elements of \mathcal{M}_b may be partially filled, the edges can be partially filled as well. To describe this, on each edge a number of edge points is defined (see figure B.4), that have their own filling state: empty or full, thus defining the filled and empty parts of the edge.

Front propagation

It is supposed that the filling state of all edge points of the complete mesh \mathcal{M}_c is known for the previous time step $t = t_{i-1}$. The source q_{i-1} in an edge point can be interpolated from the source in the nodal points, which is given by equation (2.66), but now defined on Ω_f . An edge point A can be filled by another edge point B during a period Δt_i if their mutual distance Δ^{AB} is less than $(q_{i-1}^B - q_{i-1}^A) \Delta t_i$. In that case, the source at edge point A is increased by $q_{i-1}^B - q_{i-1}^A - \frac{\Delta^{AB}}{\Delta t_i}$. The procedure is done on an element-by-element basis on mesh \mathcal{M}_c and is illustrated by figure B.5. For each element

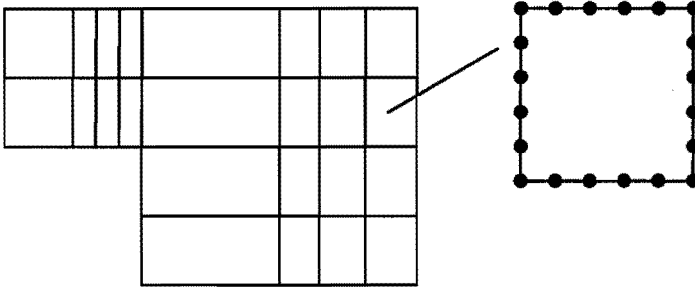


Figure B.4: Definition of edge points

it starts with the determination of edge points of the element that can be filled by the biggest source in the element, then by the biggest but one and so on. For each edge it is recorded whether the filling state of any of its edge points changed. When no edge point changed its filling state the procedure is ended. Since neighbouring elements can alter the filling stage of the edges, this procedure has to be repeated until no edge points are filled anymore. In practice this takes usually not more than three loops over the elements.

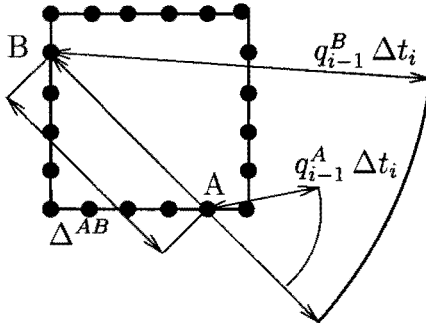


Figure B.5: The filling of edge points

The new filling state of the edge points of the complete mesh \mathcal{M}_c is transferred to those of the basis mesh \mathcal{M}_b by interpolation. This is done only for those edges of \mathcal{M}_c that coincide with edges of \mathcal{M}_b (see figure B.6). The filling state of nodal points is copied from its corresponding edge points, which all have the same filling state. At this stage all information is available

to generate a new complete mesh by copying all elements that are completely filled or empty from \mathcal{M}_b and by subdividing all partially filled elements into subelements to create \mathcal{M}_{fb} , \mathcal{M}_{fn} , \mathcal{M}_{eb} and \mathcal{M}_{en} . This will be the subject of the next section.

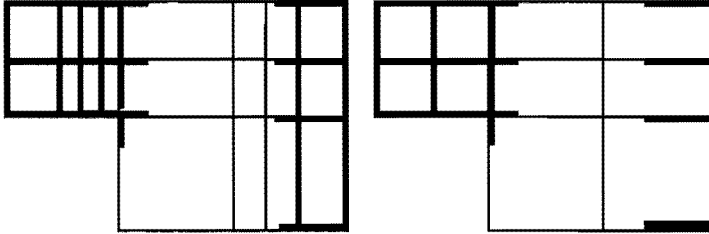


Figure B.6: Interpolation of edge point data from \mathcal{M}_c to \mathcal{M}_b

Local remeshing

The remeshing procedure is performed on an element-by-element basis on the basis mesh \mathcal{M}_b . To ensure that the number of edges along the boundary of the element of the basis mesh remains even after remeshing, a partially filled edge is always split into three parts. This is required for remeshing with quadrilaterals. If the filling state of the edge points along an edge prescribes subdivision into more than three parts, a rearrangement of the filling states is made, removing the smallest isolated group of filled or empty edge points first, until the filling state changes two times along the edge. The case empty-full-empty is excluded, so an edge is empty if its two nodes are empty. The filling state of the edge points at element vertices are never changed, in order to ensure continuity of the filling state. If, on the other hand, the filling state of edge points prescribe a subdivision into only two parts, the empty part is split. All these restrictions limit the number of cases of remeshing per element that may occur to seven (see figure B.7). Finally, figure B.8 shows the new \mathcal{M}_c at $t = t_i$ after remeshing.

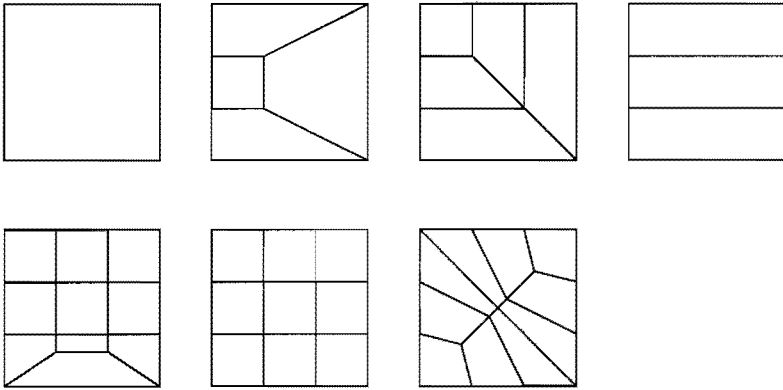


Figure B.7: The seven cases of the remeshing of a quadrilateral

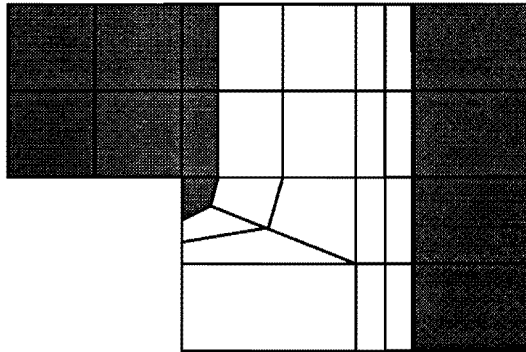


Figure B.8: Remeshed domain Ω : $\mathcal{M}_c(t_i)$

Appendix C

Simplified thermal stress computation

Viscous-elastic model

In this model a zero shear modulus is assumed for the polymer melt and a positive constant G for the glassy state. Given a constant thermal expansion coefficient α and a constant bulk modulus K , the following model can be used to describe this behaviour in the solid phase:

$$\begin{aligned}\boldsymbol{\sigma} &= -p^h \mathbf{I} + \boldsymbol{\sigma}^d \\ p^h &= K \int_0^t (\alpha \dot{T} - \text{tr}(\dot{\boldsymbol{\varepsilon}})) d\tau \\ \boldsymbol{\sigma}^d &= 2G \int_0^t \dot{\boldsymbol{\varepsilon}}^d d\tau\end{aligned}\tag{C.1}$$

with $\boldsymbol{\varepsilon} = 1/2((\vec{\nabla}\vec{u}) + (\vec{\nabla}\vec{u})^c)$, where \vec{u} is the displacement field and $\dot{}$ denotes the time derivative. Equation (C.1) can be derived from equation (2.1), similar to equation (2.33).

Simplified temperature and pressure history

The cooling process is assumed to take place in five steps. During step one, two outer surface layers cool down to mould temperature. Subsequently, the “holding” pressure is applied and a second layer solidifies. The pressure

is then removed and, in the final step, the core layer solidifies. A no-slip boundary condition is assumed.

The surface layer solidifies under zero pressure. As displacements are restricted, a tensile stress will develop (see figure C.1a). An expression for this stress level is derived as follows. The third vector of the local vector base is chosen perpendicular to the midplane of the product. The no-slip boundary condition implies:

$$\varepsilon_{11} = \varepsilon_{22} = 0, \quad \varepsilon_{33}^d = \frac{2}{3}\varepsilon_{33} \quad (\text{C.2})$$

Substitution of equation (C.2) into equation (C.1) and incorporation of the zero normal stress boundary condition for both surfaces of the product lead to:

$$\begin{aligned} \sigma_{33} &= -p^h + \sigma_{33}^d \\ &= -K\alpha\Delta T + K \operatorname{tr}(\varepsilon) + 2G\varepsilon_{33}^d = 0 \end{aligned} \quad (\text{C.3})$$

Thus the non-zero stress components equal:

$$\sigma_{11} = \sigma_{22} = \frac{2GK\alpha\Delta T}{K + 4/3G} \quad (\text{C.4})$$

with ΔT the difference between the constant glass transition temperature and the mould wall temperature. When a pressure p is applied, the overall stress level in the fluid layer is decreased by p . For the solid layer, however, σ_{11}, σ_{22} is decreased only $\frac{k}{1-k}p$, with k the Poisson ratio (see figure C.1b), while $\sigma_{33} = -p$. A second layer solidifies (see figure C.1c), resulting in a local stress level of:

$$\sigma_{11} = \sigma_{22} = -p + \frac{2GK\alpha\Delta T}{K + 4/3G} \quad (\text{C.5})$$

After the pressure is removed (figure C.1d), the core layer will solidify, developing the same tensile stress level as the first layer (figure C.1e). The stress level in the second layer will only increase $p\frac{k}{1-k}$, adding up to:

$$\sigma_{11} = \sigma_{22} = \frac{2GK\alpha\Delta T}{K + 4/3G} - \frac{p(1-2k)}{1-k} \quad (\text{C.6})$$

When the kinematic constraints are removed (see figure C.1f), the thermal effect disappears in the expression of the stress distribution. Supposing $k = 1/3$, the difference between maximum and minimum residual stress equals

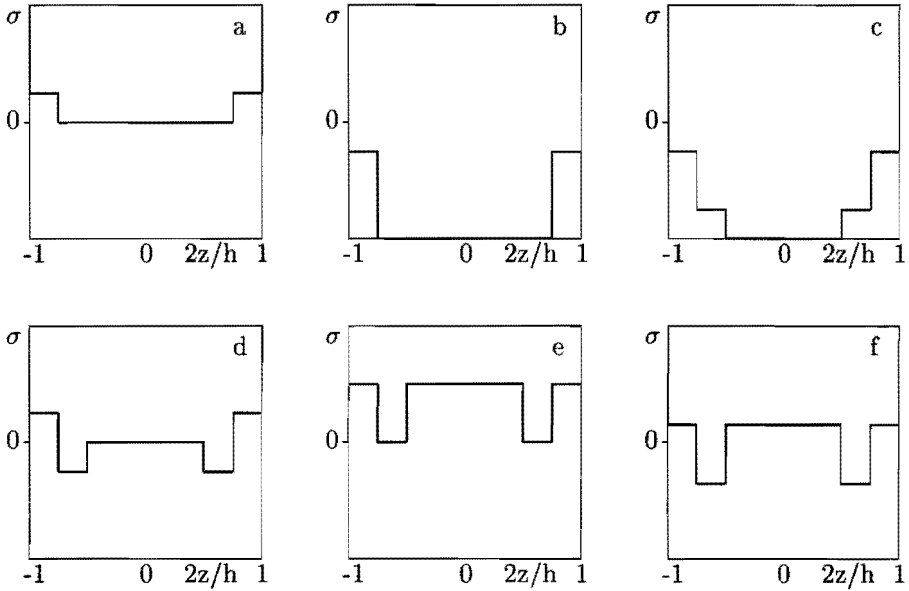


Figure C.1: Development of planar thermal stress across the reduced thickness for a viscous-elastic material (simplified five step constrained quench).

half of the maximum pressure applied. Brucato *et al.* (1989) showed that, using equations (C.1) and given the pressure history during solidification, the residual stress distribution can be written as:

$$\sigma_{11} = \sigma_{22} = -\frac{1-2k}{1-k}(p(z_{T_g}) - \bar{p}) \quad (\text{C.7})$$

with z_{T_g} the position in thickness direction of the solidification front in time, $p(z_{T_g})$ the pressure at that position, and \bar{p} the integral of $p(z_{T_g})$ across the thickness.

Appendix D

Thermomechanical Analyser

The Thermomechanical Analyser (Perkin Elmer TMA 7, see TMA (1993)) measures dimensional changes in one direction of a sample as a function of temperature and time. The apparatus consists of a sample tube and a probe inside this tube, which are both made of quartz. During operation the probe rests on the sample which is placed inside the tube (see figure D). A force of

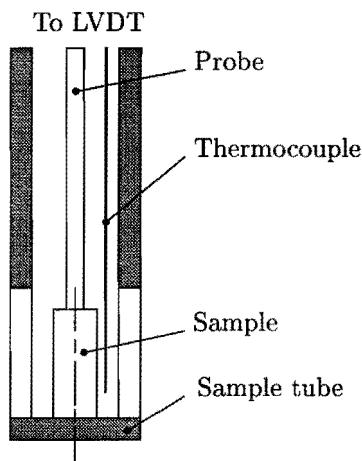


Figure D.1: Schematic layout of the sample tube of the Thermomechanical Analyser (TMA).

1 mN is applied to ensure contact between probe and sample, but preventing creep of the sample at high temperatures as much as possible. Inside the sample tube a chromel alu-mel thermocouple is installed for temperature registration. A furnace is placed around the tube, enabling temperature

control within 4 K (see TMA, 1993). The probe is connected to a LVDT (linear variable differential transformer) for registration of the expansion and contraction of the sample, with a displacement sensitivity of 50 nm . The TMA is connected to a computer (Digital DEC station 325c) to control the temperature and to store the data automatically. Unfortunately the room temperature influences the registered sample length, as it affects the LVDT. The measurements are corrected for this effect by measuring the room temperature separately.

Appendix E

Governing equations for the runner system

This appendix summarises the formulae given in Chapter 2 for the determination of the pressure and temperature distribution, but now for the runner system and runner like product parts, in order to complete the theoretical description of the code developed. The warpage analysis and the computation of flow-induced stress and elastic recovery are not extended for the runners in this study.

It is assumed that the cross section of these parts is circular, or can be modelled as such, taking an equivalent hydraulic radius. In figure E.1 the local base is shown which is used to rewrite the set of balance (2.1) to (2.4) and constitutive equations (2.5), (2.16) to (2.17) and (2.45). The assumptions adopted for the runner system are similar to those for the thin-walled geometries (see section 2.3). The shear rate that will be used in the constitutive relations can be written as:

$$\dot{\gamma}_r = \left| \frac{\partial v^s}{\partial r} \right|, \quad (\text{E.1})$$

with v^s the speed along the centre line of the geometry and r the local radial coordinate. The balance equations are rewritten as:

$$\frac{\partial v^s}{\partial s} + \frac{\partial v^r}{\partial r} = -\frac{\dot{\rho}}{\rho}, \quad (\text{E.2})$$

$$\frac{\partial p}{\partial s} = \frac{1}{r} \frac{\partial}{\partial r} \left(r \eta \frac{\partial v^s}{\partial r} \right), \quad \frac{\partial p}{\partial r} = 0, \quad (\text{E.3})$$

$$\rho c_p \dot{T} = \frac{1}{r} \frac{\partial}{\partial r} \left(r \lambda \frac{\partial T}{\partial r} \right) + \eta \dot{\gamma}_r^2 - \frac{T}{\rho} \left(\frac{\partial \rho}{\partial T} \right)_p \dot{p} \quad (\text{E.4})$$

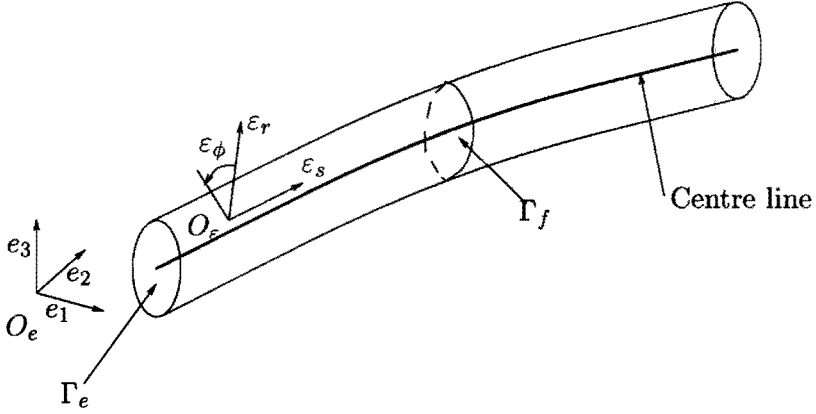


Figure E.1: Definition of local coordinates, domains and boundaries for runners

The flow front region is modelled similar to the model used for the cavity. It is assumed that the radius of the runner system is fixed, so it is not a function of the internal pressure like the thickness of the cavity (equation (2.63)). From equations (E.2) to (E.4) the pressure and temperature equations can be derived for the runner system. The pressure equation reads:

$$-\frac{\partial}{\partial s} \left(S_c \frac{\partial p}{\partial s} \right) + 2\pi \int_0^R \kappa_{\infty} \dot{p} r' dr' = 2\pi \int_0^R \left(\alpha_{\infty} \dot{T} + \frac{\dot{\delta}}{1 + \delta} \right) r' dr' \quad (\text{E.5})$$

Boundary conditions are similar to those for the cavity and are given below (see figure E.1):

$$Q = S_c \frac{\partial p}{\partial s} \quad (\Gamma_e) \quad (\text{E.6})$$

$$p = p_e \quad (\Gamma_e) \quad (\text{E.7})$$

$$p = p_{atm} \quad (\Gamma_f) \quad (\text{E.8})$$

$$\frac{\partial p}{\partial s} = 0 \quad (\Gamma_0) \quad (\text{E.9})$$

Here Γ_0 denotes the point on the centre line of a filled runner at a dead end, Γ_e is a point on the centre line at the entrance of a runner, Γ_f is a point on the centre line where a flow front is located, and Q denotes the total volume

flux. Equations (E.6) and (E.7) give possible boundary conditions at the gate, while equation (E.8) defines the boundary condition at the flow front. Finally, equation (E.9) denotes the boundary condition at the dead ends of runners.

The temperature equation for the runner system can be derived from equation (E.4):

$$-\frac{1}{r} \frac{\partial}{\partial r} \left(r \lambda \frac{\partial T}{\partial r} \right) + \rho c_p \dot{T} + \frac{T}{\rho} \left(\frac{\partial \rho}{\partial T} \right)_p \dot{p} = \eta \dot{\gamma}_r^2 \quad (\text{E.10})$$

and the boundary conditions are:

$$T = T_R \quad \text{or} \quad \lambda \frac{\partial T}{\partial x_3^\xi} = H_R (T - T_m) \quad (\Gamma_R) \quad (\text{E.11})$$

$$T = T_a \quad \text{or} \quad \lambda \frac{\partial T}{\partial x_3^\xi} = H_a (T - T_a) \quad (\Gamma_R) \quad (\text{E.12})$$

$$T = T_e \quad (\Gamma_e) \quad (\text{E.13})$$

where Γ_R is the wall at radius R of the runner, T_R is the temperature of the medium in the cooling channels and H_R is the effective heat transfer coefficient from polymer to cooling medium.

The numerical solution procedure is completely analogue to that for the cavity and is not elaborated here.

References

- Akkerman, R. (1993). *Euler-Lagrange Simulations of Non-isothermal Viscoelastic Flows*. Ph.D. thesis, University of Twente.
- Baaijens, F. P. T. (1991). Calculation of residual stresses in injection moulded products. *Rheol. Acta*, **30**, 284–299.
- Baaijens, F. P. T. and Douven, L. F. A. (1990). Calculation of flow induced residual stresses in injection moulded products. In J. F. Dijksman and F. Nieuwstadt, editors, *Integration of Theory and Applications in Applied Mechanics*, pages 73–90. Kluwer Academic Publishers, Dordrecht.
- Bird, R. B., Stewart, W. E., and Lightfoot, E. N. (1960). *Transport Phenomena*. Wiley, New York.
- Boshouwers, A. H. M. and van der Werf, J. J. (1988). *Inject-3, A Simulation Code for the Filling Stage of the Injection Moulding Process of Thermoplastics*. Ph.D. thesis, Eindhoven University of Technology.
- Brucato, V. M. B., Piccarolo, S., and Titomanlio, G. (1989). Cooling stresses in polystyrene injection moulded samples. *Materials Engineering*, **1**, 597–604.
- Caspers, L. W., Zoetelief, W. F., and Meijer, H. E. H. (1994a). Numerical simulation of the two-shot injection moulding process. *Kunststof en Rubber*, **9**, 32–36. (in Dutch).
- Caspers, L. W., Douven, L. F. A., van de Vosse, F. N., and Zoetelief, W. F. (1994b). VIP manual. Technical report, Eindhoven University of Technology.
- Chiang, H. H., Himasekhar, K., Santhanam, N., and Wang, K. K. (1991a). Integrated simulation of fluid flow and heat transfer in injection moulding

- for the prediction of shrinkage and warpage. *Heat and Mass Transf. Sol. Proc.; ASME, HTD 175/MD 25*, 133–146.
- Chiang, H. H., Hieber, C. A., and Wang, K. K. (1991b). A unified simulation of the filling and postfilling stages in injection molding. part I : Formulation. *Pol. Eng. and Sc.*, **31**, 116–124.
- Chiang, H. H., Himasekhar, K., Santhanam, N., Nagel, B., and Barton, S. (1993). Troubleshooting shrinkage and warpage problems with an integrated cae tool for injection molding. *Injection Molding Outlook Technical Papers, Reg. Techn. Conf. SPE*, pages H1–H11.
- Cintra Jr., J. S. and Tucker III, C. L. (1994). Orthotropic closure approximations for the prediction of flow induced short fiber orientation. In *Proceedings 10th Annual Meeting Pol. Proc. Soc., Akron Ohio USA*, pages 208–209.
- Douven, L. F. A. (1991). *Towards the Computation of Properties of Injection Moulded Products: Flow- and Thermally Induced Stresses in Amorphous Thermoplastics*. Ph.D. thesis, Eindhoven University of Technology.
- Dvorkin, E. N. and Bathe, K. J. (1984). A continuum mechanics based four-node shell element for general non-linear analysis. *Eng. Comput.*, **1**, 77–88.
- Ferry, J. D. (1980). *Viscoelastic Properties of Polymers*. John Wiley and Sons, Inc.
- Flaman, A. A. M. (1990). *Build-up and Relaxation of Molecular Orientation in Injection Moulding*. Ph.D. thesis, Eindhoven University of Technology.
- Gardon, R. and Narayanaswamy, O. S. (1970). Stress and volume relaxation in annealing flat glass. *J. Am. Cer. Soc.*, **53**, 380–385.
- Greener, J., O'Reilly, J. M., and Ng, K. C. (1991). The volumetric response of polymeric glasses to complex thermomechanical histories: a critical evaluation of the KAHR model. *Mat. Res. Soc. Symp. Proc.*, **215**, 99–107.
- Greiner, R. and Schwarzl, F. R. (1984). Thermal contraction and volume relaxation of amorphous polymers. *Rheologica Acta*, **23**, 378–395.

- Hayes, R. E. (1991). Numerical simulation of mold filling in reaction injection molding. *Pol. Eng. Sci.*, **31**, 842–848.
- Hieber, C. A. (1987). Melt-viscosity characterization and its application to injection molding. In A. I. Isayev, editor, *Injection and Compression Molding Fundamentals*, chapter 1. Marcel Dekker, Inc.
- Hieber, C. A. and Shen, S. F. (1980). A finite-element/finite-difference simulation of the injection-molding filling process. *J. Non-Newtonian. Fluid Mech.*, **7**, 1–32.
- Hughes, T. J. R. and Liu, W. K. (1981). Nonlinear finite element analysis of shells: Part 1. three-dimensional shells. *Computer Methods in Applied Mechanics and Engineering*, **26**, 331–362.
- Hussain, M. A., Bendler, J. T., and LeGrand, D. G. (1990). Asymptotic and approximate solution for mechanical relaxation, creep, and recovery in glassy polymers. *Computers in Engineering*, **2**, 73–75.
- Hutchinson, J. and Kovacs, A. J. (1976). *J. Polym. Sci., Polym. Phys. Ed.*, **14**, 1575.
- Isayev, A. I. and Hieber, C. A. (1980). Toward a viscoelastic modelling of the injection molding of polymers. *Rheol. Acta*, **19**, 168–182.
- Janeschitz-Kriegl, H. (1983). *Polymer Melt Rheology and Flow Birefringence*. Springer-Verlag, Berlin.
- Jansen, K. M. B. (1993). *Calculation and Control of Heat Transfer in Injection Moulding*. Ph.D. thesis, Delft University of Technology.
- Kapteijns, A. F. M. (1993). *Aspects of the Compressibility and Ageing of PMMA*. Master's thesis, Eindhoven University of Technology.
- Kohlrausch, R. (1847). *Ann. Phys. (Leipzig)*, **12**, 393.
- Kovacs, A. J., Aklonis, J. J., Hutchinson, J. M., and Ramos, A. R. (1979). Isobaric volume and enthalpy recovery of glasses. ii. a transparent multi-parameter theory. *J. Pol. Sci., Pol. Phys. Ed.*, **17**, 1097–1162.
- Lee, E. H., Rogers, T. G., and Woo, T. C. (1965). Residual stress in a glass plate cooled symmetrically from both surfaces. *J. Am. Cer. Soc.*, **48**, 480–487.

- Liang, E. W., Wang, H. P., and Perry, E. M. (1993). An integrated approach for modeling the injection, compression, and resin transfer molding processes for polymers. *Adv. Pol. Technol.*, **12**, 243–262.
- MATLAB (1992). *MATLAB User's Guide*. The MathWorks, Inc., Natick MA, USA.
- McKinney, J. E. and Simha, R. (1977). Thermodynamics of the densification process for polymer glasses. *J. Res. Nat. Bur. Stand. - A. Phys. Chem.*, **81A**, 283–297.
- Narayanaswamy, O. S. and Gardon, R. (1969). Calculation of residual stresses in glass. *J. Am. Cer. Soc.*, **52**, 554–558.
- Nguyen, K. T. and Kamal, M. R. (1993). Analysis of the packing stage of a viscoelastic melt. *Pol. Eng. Sc.*, **33**, 665–674.
- Nies, E. (1991). Private communication.
- Nies, E. and Stroeks, A. (1990). A modified hole theory of polymeric fluids. 1. equation of state of pure components. *Macromolecules*, **18**, 4088–4092.
- Papathanasiou, T. D. and Kamal, M. R. (1993). Filling of a complex-shaped mold with a viscoelastic polymer. part i: The mathematical model. *Pol. Eng. Sc.*, **33**, 400–409.
- Press, W. H., Flannery, B. P., Teukolsky, A. A., and Vetterling, W. T. (1988). *Numerical Recipes; The Art of Scientific Computing*. Cambridge University Press, New York.
- Ramaekers, R. J. A. E. (1992). *Minimizing the warpage of two-shot injection moulded products of amorphous thermoplastics*. Master's thesis, Eindhoven University of Technology.
- Ramos, A. R., Kovacs, A. J., O'Reilly, J. M., Tribone, J. J., and Greener, J. (1988). Effect of combined pressure and temperature changes on structural recovery of glass-forming materials. 1. extension of the KAHR model. *J. Pol. Sc.: Part B: Pol. Phys.*, **26**, 501–513.
- Robertson, R. E., Simha, R., and Curro, J. (1985). Effects of pressure on volume-recovery experiments. *Macromolecules*, **18**, 2239–2246.
- Saiu, M., Brucato, V., Piccarolo, S., and Titomanlio, G. (1992). Injection molding of ipp. *Intern. Polymer Processing*, **7**, 267–273.

- Santhanam, N. (1992). *Analysis of residual stresses and post-molding deformation in injection-molded components*. Ph.D. thesis, Cornell University.
- Schennink, G. G. J. (1991). Private communication.
- Schennink, G. G. J. (1993). On the dimensional stability of injection moulded, amorphous thermoplastic products. Technical report, Institute for Continuing Education, Eindhoven University of Technology.
- Segal, A. (1993). *SEPRAN, user manual, standard problems and programming guide*. Ingenieursbureau SEPRAN, Leidschendam, The Netherlands.
- Simha, R. and Somcynsky, T. (1969). *Macromolecules*, **2**, 341.
- Sitters, C. W. M. (1988). *Numerical Simulation of Injection Moulding*. Ph.D. thesis, Eindhoven University of Technology.
- Spencer, R. S. and Gilmore, G. D. (1951). *J. Colloid Sci.*, **6**, 118.
- Struik, L. C. E. (1978). *Physical Aging in Amorphous Polymers and other Materials*. Elsevier, Amsterdam.
- Struik, L. C. E. (1990). *Internal stresses, dimensional instabilities and molecular orientations in plastics*. John Wiley and Sons Ltd.
- Tas, P. P. (1994). *Film Blowing: from Polymer to Product*. Ph.D. thesis, Eindhoven University of Technology.
- Timmermans, L. J. P. (1994). *Analysis of spectral element methods with application to incompressible flow*. Ph.D. thesis, Eindhoven University of Technology.
- Titomanlio, G., Brucato, V., and Kamal, M. R. (1987). Mechanism of cooling stress build-up in injection molding of thermoplastic polymers. *Intern. Pol. Proc.*, **1**, 55-59.
- TMA (1993). *Users manual 7 Series/UNIX TMA 7 Thermomechanical Analyzer*. The Perkin Elmer Corporation, USA, manual part no. 0993-8677 rev c edition.
- Tribone, J. J. and O'Reilly, J. M. (1989). Pressure-jump volume-relaxation studies of polystyrene in the glass transition region. *J. Pol. Sc.: Part B: Pol. Phys.*, **27**, 837-857.

- Turng, L. S. and Wang, V. W. (1991). Simulation of co-injection and gas-assisted injection molding. In *In Search of Excellence, ANTEC Conference Proceedings*, volume 37, pages 297–300. SPE.
- Turng, L. S., Wang, V. W., and Wang, K. K. (1993). Numerical simulation of co-injection molding filling process. *J. of Eng. Mat. and Techn.*, **115**, 48–53.
- VDMA, editor (1979). *Kenndaten für die Verarbeitung thermoplastischer Kunststoffe*, volume 1. Thermodynamik. Carl Hanser Verlag, München.
- Vleeshouwers, S. M. (1993). *Modelling and Predicting Properties of Polymers in the amorphous glassy state*. Ph.D. thesis, Eindhoven University of Technology.
- Walsh, S. F. (1993). Shrinkage and warpage predictions for injection molded components. *J. Reinf. Plast. Comp.*, **12**, 769–777.
- Williams, G. and Watts, D. C. (1970). *Trans. Faraday Soc.*, **66**, 80.
- Williams, M. L., Landel, R. F., and Ferry, J. D. (1955). *J. Am. Chem. Soc.*, **77**, 3701.
- Wimberger-Friedl, R. (1991). *Orientation, Stress and Density Distributions in Injection-Moulded Amorphous Polymers Determined by Optical Techniques*. Ph.D. thesis, Eindhoven University of Technology.
- Wimberger-Friedl, R. (1994). Molecular orientation induced by cooling stresses. birefringence in polycarbonate: Iii. constrained quench and injection molding. *J. Pol. Eng. Sci.: Part B: Pol. Phys.*, **32**, 595–605.
- Wimberger-Friedl, R. (1995). Private communication.
- Wimberger-Friedl, R. and de Bruin, J. G. (1993). Gapwise density distributions in injection-molded poly(methylmetacrylate). *Pol. Eng. Sci.*, **33**, 383–392.
- Zoetelief, W. F. (1995). *Multi-Component Injection Moulding*. Ph.D. thesis, Eindhoven University of Technology.
- Zoetelief, W. F., Douven, L. F. A., and Ingen-Housz, A. J. (1995). Residual thermal stresses in injection moulded products. *Pol. Eng. Sci.* accepted.

- Zoller, P. (1982). A study of the pressure-volume-temperature relations of four related amorphous polymers: Polycarbonate, polyarylate, phenoxy, and polysulfone. *Jrnl. of Polymer Sc.*, **20**, 1453-1464.
- Zoller, P., Bolli, P., Pahud, V., and Ackermann, H. (1976). *Rev. Sci. Instrum.*, **47**, 948.

Samenvatting

Spuitsieten is een veel toegepaste techniek voor het vervaardigen van grote series dunwandige kunststof produkten. De matrijs, waarin de vormholte zich bevindt, is vaak complex. Het is duur en tijdrovend fouten in het matrijsontwerp later te herstellen. Vandaar dat tijdens het ontwerp met succes gebruik wordt gemaakt van simulatie-programmatuur teneinde het procesverloop te voorspellen en te optimaliseren. Een perfect procesverloop zegt echter nog niets over de kwaliteit van de vervaardigde produkten. De steeds hoger wordende kwaliteitseisen die aan de veelal technologische produkten worden gesteld, maken het noodzakelijk om voorspelling en optimalisering van produkteigenschappen deel te laten uitmaken van het ontwerpproces. Dit vraagt om een integrale aanpak van de modelvorming van het spuitgietproces.

Dit proefschrift beschrijft de modelvorming van het vormgevingsproces en van de resulterende produkteigenschappen. Veel van deze eigenschappen, zoals de ingevroren oriëntatie, de dichtheid, de materiaalverdeling bij het meer-componenten spuitgieten (M-CIM), de conversiegraad bij de verwerking van reactieve materialen ((R)RIM, SRIM en RTM) maar ook de vezeloriëntatie in glasvezelgevulde materialen, zijn een gevolg van de totale thermomechanische geschiedenis van elk materieel punt. Een voldoende nauwkeurige, numerieke methode voor de benadering van materiële tijdsafgeleiden is dan ook mede bepalend voor de kwaliteit van het model. De berekening van stroombanen kan tevens worden gebruikt voor het toetsen van de nauwkeurigheid van de gebruikte methode.

Krimp- en kromtrekgedrag, fysische veroudering en de zogenoemde “elastic recovery”, of elastische terugvering, zijn de hier voornamelijk bestudeerde produkteigenschappen. Ze zijn afhankelijk van de verdeling van de restspanningen en de dichtheid in het produkt. De *dichtheid* wordt beschreven met behulp een geschiedenis-afhankelijk model, genaamd het KAHR model. Met name het drukverloop tijdens de nadrukfase wordt bepaald door de dichtheid

als functie van temperatuur en druk en tijd. Toch blijkt de berekening van de dichtheid praktisch te kunnen worden ontkoppeld van de drukberekening en kan bovendien de convectieve afgeleide van de dichtheid worden verwaarloosd. Dit leidt tot een enorme winst in rekentijd.

De *restspanningen* kunnen worden onderverdeeld naar hun ontstaansoorzaak. De *stromingsgeïnduceerde spanningen* ontstaan tijdens de vul- en de nadrukfase en correleren met de oriëntatie van de makromolekullen. Deze oriëntatie wordt (gedeeltelijk) ingevroren en veroorzaakt anisotropie in thermische, mechanische en optische eigenschappen. Bovendien leiden deze spanningen tot een verminderde dimensiestabiliteit als gevolg van elastische terugvering. Omdat de oriëntatie de stroming nauwelijks beïnvloedt, kan ook hier een bijzonder effectieve ontkoppelde rekenwijze worden toegepast met verwaarlozing van de convectieve afgeleiden. Een compressibel Leonov model is gebruikt voor de berekening van deze spanningen. De *thermisch en druk geïnduceerde spanningen* (ook wel thermische spanningen genoemd) ontstaan hoofdzakelijk tijdens de navulfase en koelfase en worden veroorzaakt door inhomogeen koelen onder een verlopende druk, met als gevolg inhomogene krimp over de dikte van het produkt. Een multi-mode Maxwell model (een linearisatie van bovengenoemd Leonov model) is gebruikt voor de berekening van thermische spanningen. Deze spanningen zijn vaak een orde groter dan de eerdergenoemde stromingsgeïnduceerde spanningen en bepalen het kromtrekgedrag van het produkt. Een tweeschotsspuitsprocees is als voorbeeld genomen om het ontstaan van thermische spanningen toe te lichten. Uit deze analyse bleek dat het kromtrekken van het produkt als gevolg van asymmetrisch afkoelen van het tweede schot kan worden voorkomen door verschillende nadrukniveaus te kiezen voor de twee achtereenvolgende spuitgietsproeijen.

De numerieke simulaties zijn gevalideerd aan de hand van experimentele resultaten, maar zijn ook getoetst aan analytische oplossingen van vereenvoudigde problemen. De meetresultaten van dichtheidsverdeling en dimensiestabiliteit, afkomstig uit de literatuur, betreffen uitsluitend rechte strepen, waarvoor een twee-dimensionale analyse voldoende zou zijn geweest. De geometrie van het tweeschotsprodukt is iets complexer, waardoor hier minstens een $2\frac{1}{2}$ D benadering vereist is. Deze benadering is geïmplementeerd in het simulatie programma VIp (een afkorting van *Polymer Processing & Product Properties Prediction Program*), dat ontwikkeld is binnen het Centrum voor Polymeren en Composieten van de Technische Universiteit Eindhoven. Het programma is flexibel met betrekking tot produktgeometrie en materiaal modellen, en blijkt praktisch toepasbaar.

Acknowledgements

The author wishes to thank all people who contributed to the research described in this thesis. The work would not have been possible without the substantial contribution of the other members of the “VIp-team” Lucien Douven, Frans van de Vosse and Wim Zoetelief. Furthermore Reinhold Wimberger-Friedl and Hans de Bruin from Philips Research Laboratories allowed me to use the TMA and I appreciate the discussions we had concerning these measurements. I wish to thank Gerald Schennink for letting me use his rheological data on PMMA, and Erik Nies for his experimental $p\nu T$ data, but also for sharing his “ab initio” approach to the modelling of thermodynamic properties of polymers. The numerical implementation of all models used was possible only, thanks to the people from “Ingenieursburo Sepra” Guus Segal and Niek Praagman. The master students Ralph Ramaekers, Otwin Günther, Peter Toonssen and Michiel Spek are gratefully acknowledged for their contribution to the work. Finally, I would like to thank Will Balemans from Philips CFT Technology for his critical evaluation of the code.

Curriculum Vitae

Leo W. Caspers

- Feb. 25th 1967: Born in Waalwijk, The Netherlands
- 1979–1985: Student at the Mgr. Frencken College (Atheneum), Oosterhout, The Netherlands
- 1985–1991: Student at Eindhoven University of Technology, Department of Mechanical Engineering, Eindhoven, The Netherlands
- 1991–1995: Research assistant at Eindhoven University of Technology, Centre for Polymers and Composites, Department of Mechanical Engineering, Eindhoven, The Netherlands

Stellingen

behorende bij het proefschrift

VIp, an integral approach to the simulation of injection moulding prediction of product properties

1. Bij de toepassing van de $2\frac{1}{2}D$ benadering is het gebruik van hogere-orde elementen voor de druk noodzakelijk om hieruit een snelheidsveld te kunnen bepalen dat voldoende nauwkeurig is voor de berekening van stroombanen.
 - Dit proefschrift, appendix A.
2. Bij de berekening van de dichtheidsverdeling met behulp van een geschiedenisafhankelijk model is de in dit proefschrift voorgestelde ontkoppelde rekenwijze, van druk en temperatuur enerzijds en dichtheid anderzijds, toelaatbaar.
 - Dit proefschrift, hoofdstuk 5.
3. Voor de voorspelling van geschiedenisafhankelijke produkteigenschappen bij de simulatie van het spuitgietproces is de berekening van stroombanen essentieel. Bij ontkoppeling van de berekening van procesgrootheden en produkteigenschappen kan echter vaak met het convecteren van alleen druk en temperatuur worden volstaan.
 - Dit proefschrift, hoofdstuk 5.
4. De dimensiestabiliteit van gespuitsgiete, amorfe, kunststof producten wordt bij temperaturen dicht bij de glasovergangstemperatuur bepaald door elastische terugvering. Bij lagere temperaturen neemt de invloed hiervan af en wordt de bijdrage van volumerelaxatie doorslaggevend.
 - G.G.J. Schennink, *On the dimensional stability of injection moulded, amorphous thermoplastic products*, Institute for Continuing Education, Eindhoven University of Technology, 1993
 - Dit proefschrift, hoofdstuk 5.

5. 2,3 Megabyte sourcecode is voor één promovendus niet goed beheersbaar, laat staan voor meerdere(n).
6. Een numerieke simulatie van een experiment moet eveneens reproduceerbaar zijn.
7. Het slaap- en waakpatroon van een cavia is een eigenschap die te benijden valt. Zijn hiermee samenhangende levensverwachting is dat echter niet.
8. Wat in een carpool-car gezegd wordt, is niet bestemd voor daarbuiten.
9. Het feit dat erg lekker en erg gezond eten zo zelden samen gaan lijkt in tegenspraak met de evolutieleer.
10. Amateur-strijkers lijken vals, blazers zijn het.